University of South Florida
Scholar Commons

Graduate Theses and Dissertations | Graduate School

January 2014

Integrated Electrostatically- and Piezoelectrically-Transduced Contour-Mode MEMS Resonator on Silicon-on-Insulator (SOI) Wafer

I-Tsang Wu
University of South Florida, iwu@mail.usf.edu

Follow this and additional works at: http://scholarcommons.usf.edu/etd

Part of the Electrical and Computer Engineering Commons

Scholar Commons Citation
Wu, I-Tsang, "Integrated Electrostatically- and Piezoelectrically-Transduced Contour-Mode MEMS Resonator on Silicon-on-Insulator (SOI) Wafer" (2014). *Graduate Theses and Dissertations.*
http://scholarcommons.usf.edu/etd/5336

This Dissertation is brought to you for free and open access by the Graduate School at Scholar Commons. It has been accepted for inclusion in Graduate Theses and Dissertations by an authorized administrator of Scholar Commons. For more information, please contact scholarcommons@usf.edu.

Integrated Electrostatically- and Piezoelectrically-Transduced Contour-Mode MEMS Resonator on Silicon-on-Insulator (SOI) Wafer

by

I-Tsang Wu

A dissertation submitted in partial fulfillment
of the requirements for the degree of
Doctor of Philosophy
Department of Electrical Engineering
College of Engineering
University of South Florida

Major Professor: Jing Wang, Ph.D.
Thomas M. Weller, Ph.D.
Silvia Thomas, Ph.D.
Ashok Kumar, Ph.D.
Andreas Muller, Ph.D.

Date of Approval:
June 24, 2014

Keywords: Capacitive, ALD, Hybrid, CMP, Tuning

Copyright © 2014, I-Tsang Wu

Dedication

To my parents, my family, my friends, and my teachers.

Acknowledgments

I like to express my gratitude to my mother, Chiung-Yueh Hsu, who has given and supported me my entire life. She has been my inspiration, strength and the role model all my life. I am what I am thanks to her.

I want to state my appreciation to my major professor Dr. Jing Wang, for his academic guidance and support in making me a better scholar and professional in my field. Special thanks are given to my close friends and colleagues Dr. Cesar Morales, Dr. Julio Dewdney, Tianpeng Wu, and Scott Skidmore, who have helped me in many aspects of my work. This work wouldn't have been possible without them. I have enjoyed working with them for the past years, and hopefully our path may cross again in the future. I will like to extend my gratitude to my long-time friend, Kosol Son, who has not only assisted me with academia work, but also helped shaped my career path. I also want to thank Di Lan, Jin Chen, Paula Algarin, Yilu Ning, Juan Castro, and Vinicio Carias for always providing me with helping hand and encouragement during the moments of need.

I would also like to give my most sincere gratefulness to the staff at the NREC and TSS. A special thanks to Rich Everly and Rob Tufts, who continuously provide to facility users with their relentless support and technical knowledge. Last but not least, I want to give a big thank you to Michael Konrad, who has always been there for the students when things are not working properly. I cannot imagine the college without them.

Table of Contents

List of Tables iii

List of Figures iv

Abstract viii

Chapter 1 Introduction 1
- 1.1 Overview 1
- 1.2 Modern Day Transceiver Architecture 2
- 1.3 MEMS Technology Enabled Transceiver Architecture 4
- 1.4 Review of Current State of the Art 5
  - 1.4.1 Electrostatically-Transduced MEMS Resonators 6
  - 1.4.2 Piezoelectrically-Transduced MEMS Resonators 10
- 1.5 Summary of Current State of the Art 14
- 1.6 Dissertation Organization 15
- 1.7 Contributions 15

Chapter 2 Background 17
- 2.1 Piezoelectric Effect 18
- 2.2 Piezoelectric Materials 19
- 2.3 Mathematical Model of the Piezoelectric Effect 20
- 2.4 Operating Principle of MEMS Resonators 20
  - 2.4.1 Piezoelectric MEMS Resonators 21
  - 2.4.2 Capacitive MEMS Resonators 22
  - 2.4.3 Thin-film Piezoelectric-on-Silicon (TPoS) Resonators 23
- 2.5 Contour-Mode Resonators 24
  - 2.5.1 Contour-Mode Circular Disks 24
  - 2.5.2 Contour-Mode Rectangular Plates 27
- 2.6 Mechanical Resonator Modeling 29
- 2.7 Model Parameters for Equivalent Electrical Circuit 30

Chapter 3 Development of Piezoelectrically-Transduced Resonator 32
- 3.1 Selection of Material 33
- 3.2 ZnO Characterization 34
  - 3.2.1 Effects of Oxygen Concentration 34
  - 3.2.2 Effects of Substrate Temperature 36
- 3.3 Fabrication Process for Thin-film Piezoelectric on Silicon 37
- 3.4 Experimental Results 39

3.5 Piezoelectric RF MEMS Filter 44
3.5.1 MEMS Filter Operating Theory 44
3.5.2 Experimental Results 47

Chapter 4 Development of Electrostatically-Transduced Resonator 50
4.1 Atomic Layer Deposition 51
4.2 Chemical Mechanical Polishing 52
4.3 Fabrication of Electrostatically-Transduced Resonator 54
4.4 Experimental Result 56
4.5 Formation of Parallel Plate Capacitor Gap 60

Chapter 5 Micromechanical Resonators Applications Using SOI Wafer 62
5.1 Single-Mask Nano-Gap Electrostatically-Transduced MEMS Resonator 62
5.2 RF MEMS Resonator and Filter Frequency Tuning 65
5.2.1 Experimental Result 68
5.3 Dual-Transduced Hybrid MEMS Resonator 71
5.3.1 Fabrication Process 73
5.3.2 Experimental Result 75
5.4 Parasitic Feedthrough 76
5.4.1 Comparison between Capacitive and Piezoelectric Resonators 77
5.4.2 Comparison between High and Low Resistivity Substrates 80

Chapter 6 Conclusion and Future Work 84
6.1 Summary and Contributions to the RF-MEMS Field 84
6.2 Future Work 86

References 90

About the Author End Page

List of Tables

Table 2.1 – Properties of most common piezoelectric materials 19

Table 2.2 – Mechanical properties of the materials used for the development of MEMS resonators. 26

Table 2.3 – Direct analogy between electrical and mechanical domain 29

Table 3.1 – Properties of piezoelectric materials 34

Table 5.1 – Thermal expansion coefficient for silicon and ZnO 69

Table 5.2 – Summarized characteristics of electrostatically- and piezoelectrically-transduced MEMS resonators. 72

Table 5.3 – SOI wafer's electrical equivalent parasitic elements 82

List of Figures

Figure 1.1 – Block diagram for a typical super-heterodyne transceiver 3

Figure 1.2 – Simplified block diagram of RF-MEMS-enabled channel select transceiver. 4

Figure 1.3 – (a) A 37 MHz VHF free-free beam mechanical filters. 6

Figure 1.4 – Micromechanical contour-mode disk resonator operating at 156 MHz under atmospheric pressure. 7

Figure 1.5 – (a) SEM image of a self-aligned radial contour-mode disk resonator. 8

Figure 1.6 – (a) SEM image of an internal dielectrically-transduced resonator. 9

Figure 1.7 – Schematic of a typical SAW resonator. 10

Figure 1.8 – BAW resonators with different types of acoustic isolation mechanisms: (a) air cavity, and (b) Bragg's Reflector. 11

Figure 1.9 – (a) SEM image of a bandpass filter formed by piezoelectric resonator in L-ladder configuration. 12

Figure 1.10 – (a) Electrical response and SEM image of a 435-MHz of lateral monolithic filter. 13

Figure 2.1 – Illustration of the direct and reverse piezoelectric effects. 18

Figure 2.2 – Schematic-view diagram of a piezoelectric 1-port square-plate resonator (a) and a 2-port circular-disk capacitive resonator (b). 21

Figure 2.3 – Vibration modes of a piezoelectric rectangular plate resonator. 22

Figure 2.4 – 1-port piezoelectric on substrate resonator. 23

Figure 2.5 – Finite-element simulation of a ZnO-on-silicon disk resonator in its (a) fundamental radial contour-mode at 91.5 MHz and (b) wine-glass mode at 67.5 MHz. 25

Figure 2.6 – Longitudinal-mode rectangular plate resonator. 27

Figure 2.7 – Equivalent lumped-element model of a micromechanical resonator. 30

Figure 3.1 – XRD curves for ZnO samples deposited at different oxygen concentrations. 35

Figure 3.2 – XRD curves for ZnO samples deposited at different substrate temperatures. 36

Figure 3.3 – Five-masks post-CMOS compatible fabrication process of thin-film piezoelectric-on-silicon (TPoS) resonator. 38

Figure 3.4 – (a) SEM photo of a TPoS resonator fabricated using the process described above. 39

Figure 3.5 – Experimental set up for on-wafer probing of MEMS resonators. 40

Figure 3.6 – Frequency response of a 60 μm × 150 μm TPoS plate resonator with 15 μm Si device layer excited in its fundamental extensional contour-mode. 41

Figure 3.7 – Frequency response of a 60 μm × 150 μm TPoS plate resonator with 6 μm Si device layer excited in its fundamental extensional contour-mode. 42

Figure 3.8 – SEM picture of a 60 μm × 150 μm TPoS plate resonator fabricated on SOI wafer with 15 μm-thick device layer. 43

Figure 3.9 – Illustration of the working principle for a mechanically-coupled resonator filter vibrating in (a) in-phase mode; (b) out-of-phase mode; with (c) predicted bandpass frequency characteristic; and (d) electrical equivalent circuit model. 45

Figure 3.10 – Simulated dual fundamental length-extensional mode of a 60 μm x 30 μm ZnO plate resonator (a) symmetric resonance-mode and (b) asymmetric resonance-mode. 46

Figure 3.11 – Simulated dual fundamental length-extensional mode of a 70 μm × 30 μm ZnO plate resonator (a) symmetric resonance-mode; and (b) asymmetric resonance-mode. 46

Figure 3.12 – (a) Equivalent electrical circuit model for a 2nd order acoustically-coupled filter; (b) Normalized frequency response for a 2nd order acoustically coupled filter. 47

Figure 3.13 – Frequency response for the fabricated 115 MHz monolithic filter with 100 µm x 200 µm lateral dimensions. 48

Figure 3.14 – Frequency response for the fabricated 114 MHz monolithic filter with 100 µm x 190 µm lateral dimensions. 48

Figure 4.1 – Schematic showing of ALD self-limiting process. 52

Figure 4.2 – Schematic illustration of CMP process. 53

Figure 4.3 – Two steps photolithograph process of capacitive resonator. 54

Figure 4.4 – (a) SEM image of a capactively-transduced resonator. 55

Figure 4.5 – Experimental set up for on-wafer probing of the capacitive micro-resonators. 56

Figure 4.6 – S-parameter for the 24µm disk resonator vibrating in wine-glass mode. 57

Figure 4.7 – (a) Electrical equivalent circuit of a mechanical resonator. 58

Figure 4.8 – Transmission response vector subtraction. 59

Figure 4.9 – S-parameter for the 24µm disk resonator vibrating in wine-glass mode. 59

Figure 4.10 – Resonating transmission response of the disk resonator under various DC bias conditions. 60

Figure 4.11 – (a) Junction structure before the device release. 61

Figure 5.1 – Single-mask fabrication for electrostatically-transduced resonator. 63

Figure 5.2 – 280 nm gap generated by using aforementioned single-mask nano-gap process. 64

Figure 5.3 – (a) Plasma-Therm high aspect ratio (50:1) DRIE Si etch with 100 nm openings. 65

Figure 5.4 – DC bias electrical connection of resonator frequency tuning off (a) and on (b). 66

Figure 5.5 – Frequency response of the resonator for three different tuning potentials. 70

Figure 5.6 – Resonator frequency tuning characteristics. 70

Figure 5.7 – Fabrication process of the dual-transduced resonator. 74

Figure 5.8 – SEM image of dual-transduced hybrid resonator. 75

Figure 5.9 – Frequency response from three different types of resonators up to 1 GHz. 78

Figure 5.10 – Illustration of leakage feedthrough signal travel paths for different resonators. 79

Figure 5.11 – (a) A faraday cage structure engineered into the substrate. 80

Figure 5.12 – Frequency response from 60 µm × 150 µm resonators residing on SOI substrates with different resistivity. 81

Figure 5.13 – Equivalent circuit model representation of SOI wafer. 82

Figure 5.14 – Frequency response from test pad structures residing on SOI substrates with different resistivity. 83

Figure 6.1 – Original proposed fabrication process for the hybrid resonator. 88

Abstract

Due to the recent rapid growth in personal mobile communication devices (smartphones, PDA's, tablets, etc.), the wireless market is always looking for new ways to further miniaturize the RF front-ends while reducing the cost and power consumption. For many years, wireless transceivers and subsystems have been relying on high quality factor (Q) passives (*e.g.*, quartz crystal, ceramics) to implement oscillators, filters, and other key RF front-end circuitry elements. However, these off-chip discrete components occupy large chip area and require power-demanding interfacing circuits. As a result, a great deal of research effort has been devoted to the development of micromechanical resonators that are much more amenable to direct integration with integrated circuit (IC).

Over the past few years, vibrating RF MEMS (Micro-Electrical-Mechanical-System) resonator technology has emerged as a viable solution, most notably, the film bulk acoustic resonator (FBAR) and surface acoustic wave (SAW) resonator, which have already been successfully implemented into commercial products. Undoubtedly, micromechanical resonators such as FBAR's can perform as well as if not better than its bulky conventional counterparts and facilitate the miniaturization and power reduction of conventional RF systems. However, in some cases when multi-frequency functionality on a single-chip is needed, FBAR simply won't deliver.

To address this dilemma, contour-mode MEMS resonators have been developed and regarded as the most viable on-chip high-Q alternative. Unlike FBAR, contour-mode resonators

use lateral dimensions to define its resonating frequencies, thus allowing for single-chip multi-frequency functionality. However, there is still room for improvement with respect to lowering the motional resistance of these devices to allow matching to 50 Ω electronics, while retaining low power consumption, small size, and simpler manufacturing process.

This dissertation presents the design, fabrication, characterization and experimental analysis of two types of micro-mechanical resonators. Piezoelectrically- and electrostatically-transduced micromechanical resonators will both be shown. Both types of resonator will be fabricated in the same micro-fabrication run, which makes the comparison between the two much more impartial. The impacts of substrate's resistivity over the device performances will also be studied.

Among the most significant results, this dissertation also presents several ideas that are enabled by the use of silicon-on-insulator (SOI) wafer. A novel single-mask fabrication process that can produce capacitive resonator with nano-meter gap is demonstrated. The concept of dual-transduced micro-mechanical resonator is introduced by combining both piezoelectric and capacitive based resonators. Finally, frequency tuning of MEMS resonator are explored and detailed in this work as well.

Chapter 1

Introduction

1.1 Overview

Since the first wireless transmission in 1895 by Guglielmo Marconi, wireless communications have revolutionized the way how human and the society interact with one and another. Nowadays, wireless technologies are used in a wide variety of applications such as satellite transmission, radio and television broadcasting, sensor networks, global positioning system (GPS), mobile communications, and, most importantly, a new generation of multifunctional, small size, and low cost communication devices such as smartphones and lab-on-a-chip systems.

Due to the recent rapid growth multifunctional wireless communication devices, the wireless market is always looking for new ways to further miniaturize the RF front-ends while reducing the cost and power consumption. For many years, wireless transceivers and subsystems have been relying on high quality factor (Q) passives (*e.g.*, quartz crystal, ceramics) to implement oscillators, filters, and other key RF front-end circuitry elements. However, these off-chip discrete components occupy large chip area and require power-demanding interfacing circuits. As a result, a great deal of research effort has been devoted to the development of micromechanical resonators that are much more amenable to direct integration with integrated circuit (IC).

Over the past few years, vibrating RF MEMS (Micro-Electrical-Mechanical-System) resonator technology has emerged as a viable solution, most notably, the film bulk acoustic resonator (FBAR) and surface acoustic wave (SAW) resonator, which have already been successfully implemented into commercial products. Undoubtedly, micromechanical resonators such as FBAR can perform as well as if not better than its bulky conventional counterparts and facilitate the miniaturization and power reduction of conventional RF systems. However, in cases when multi-frequency functionality on a single-chip is needed, FBAR simply won't deliver.

To address this dilemma, contour-mode RF MEMS resonators have been developed and regarded as the most viable on-chip high-Q alternative. Unlike FBAR, contour-mode resonators use lateral dimensions to define its resonating frequencies, thus allowing for single-chip multi-frequency functionality. However, there is still room for improvement with respect to lowering the motional resistance of these devices to allow matching to 50 Ω electronics, while retaining low power consumption, small size, and simpler manufacturing process.

1.2 Modern Day Transceiver Architecture

A transceiver is a wireless device that consists of both a transmitter and a receiver that share a mutual circuitry. As the name suggested, a transceiver is responsible for transmitting and receiving radio frequency signals. A transmitter modulates, up-converts, and amplifies a local baseband signal into carrier frequency for transmission by the antenna. Contrarily, a receiver is to demodulate, down-convert, and filter the said signal transmitted over the air. Understandably, the design requirement for the receiver is much more critical and challenging to the overall performance of a wireless system since receiver has to process signals that have been distorted and interfered by the surrounding wireless noisy environment.

One of the most popular transceiver configurations is the super-heterodyne architecture, which has been used in the majority of wireless system since its invention by Edwin Armstrong in 1917. A general schematic of a modern day transceiver circuit is shown in Figure 1.1. As shown in the schematic, a wireless signal has to go through a series of filtration, amplification, and signal processing. Amplification and signal processing have been successfully implemented with integrated circuit (IC) technologies. In contrast, the filtration aspect still requires the use of off-chip components such quartz crystals, surface acoustic wave (SAW) and bulk acoustic wave (BAW) devices. Even though BAW and SAW enabled oscillators and filters outperform their semi-conductor counterparts in terms of insertion loss, quality factor, and percent bandwidth, they are bulky and energy consuming. Moreover, these off-chip components need to be interfaced with IC circuit at the board level, thus hindering the miniaturization of transceiver.

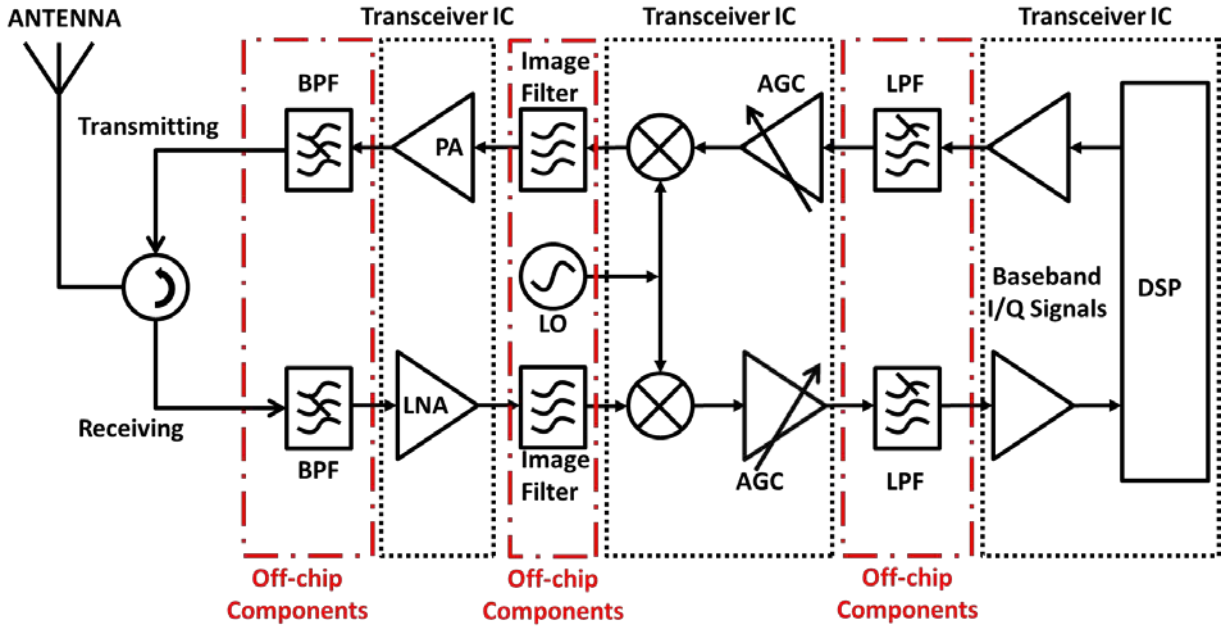

Figure 1.1 – Block diagram for a typical super-heterodyne transceiver

Although super-heterodyne transceiver architectures incorporating off-chip BAW and SAW devices fulfill the requirements for current wireless communication systems, as the

demand for high selectivity, high quality factor keep on increasing, our current technology implementation will not be able to keep up and provide satisfactory performance in regards of size and power consumption. Some efforts have been made in the development of alternative transceiver architectures such as direct conversion [1], low-IF [2], and RF sampling down-conversion [3]. While these alternatives show great potential in solving our current dilemma [4], it still requires MEMS to provide the much needed high quality factor, IC compatible filter and oscillator.

1.3 MEMS Technology Enabled Transceiver Architecture

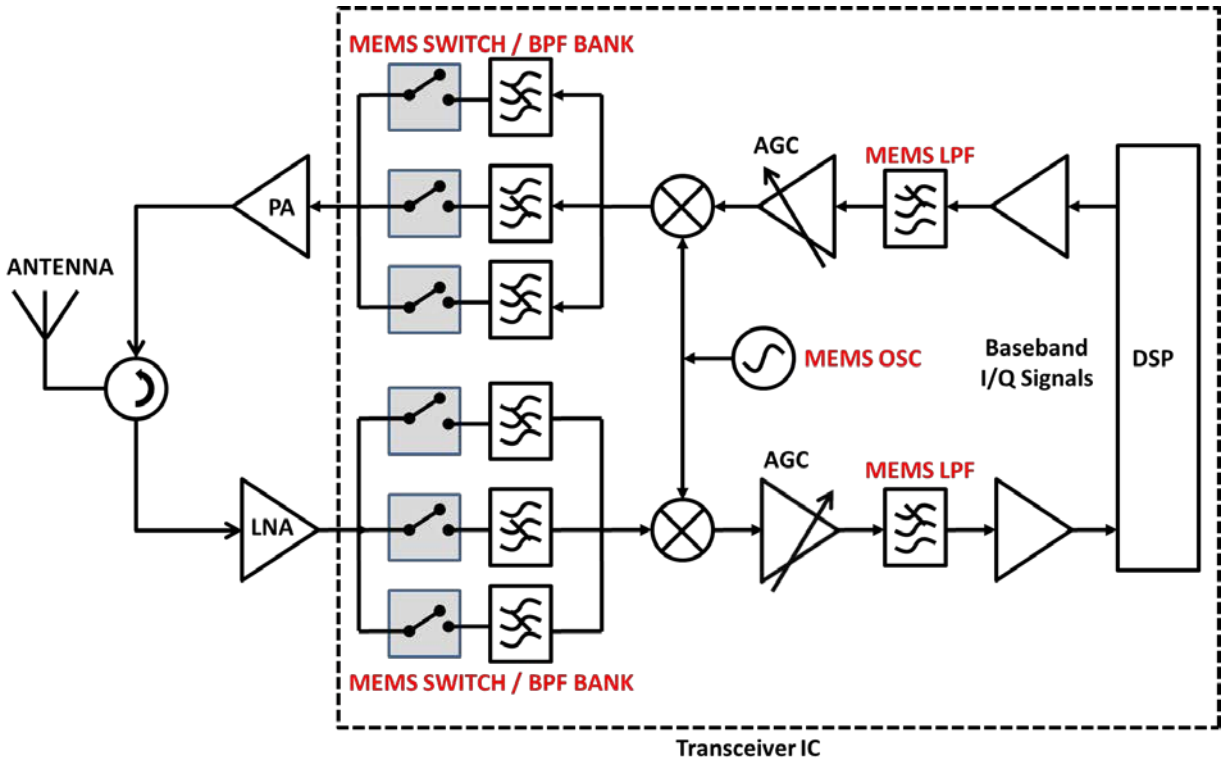

Figure 1.2 – Simplified block diagram of RF-MEMS-enabled channel select transceiver.

One of the most actively pursued methods for total transceiver IC integration is CMOS-compatible RF MEMS technology. Not only has RF MEMS enabled the transceiver to have smaller foot print and lower power consumption, but it also improves the performance greatly.

The selectivity needed for architecture such as direct-heterodyning can only be obtained through RF MEMS. Selectivity, which is the ability to pick up the wanted signal while rejecting adjacent frequency interference, has become one of the most important characteristics of a receiver. The selectivity of a filter is determined by its quality factor, Q, given by:

$$Q = \frac{f_0}{BW} \tag{1.1}$$

CMOS-compatible RF MEMS devices with Q >10,000 at GHz have been demonstrated previously [5], and the advancement in MEMS technology have made possible for the fabrication of on-chip RF MEMS components, such as RF switches [6], voltage controlled oscillators (VCO) [7, 8], and mixers. Figure 1.2 is an example of how a RF MEMS-enabled transceiver can be integrated into one single monolithic circuit by eliminating all the external components such as SAW, BAW devices, and the quartz crystals oscillators. Besides the size and power consumption reduction advantages stated above, the new RF MEMS-enabled transceiver architectures can create a new generation of reconfigurable multi-band, multi-frequency portable wireless communication devices, which one single transceiver IC can cover several services operating over a wide range of frequencies.

1.4 Review of Current State of the Art

The concept of micro-electromechanical (MEM) resonator was introduced for the first time in the 60's by Nathanson [9]. Though the concept was sound, it wasn't till the late 90's that it started to be used in RF/MW applications due to the advancements in material science and fabrication process. Clark Nguyen [10] and William C. Tang [11] popularized RF MEMS concept by introducing comb drive mechanical systems as the major building block for RF/MW components – resonators and filters. These devices were capable at medium-frequency range (300 kHz to 3 MHz), and such band pass filter has shown 0.1 dB insertion loss [12]. Shortly

afterwards, MEMS for wireless communication started to garner mainstream attention, and as a result, a huge amount of effort have been devoted into extending the operational frequency to high-frequency (HF - 3 to 30MHz) and very high frequency range (VHF – 30 to 300 MHz), as well as widening the working bandwidth. Free-free beam poly-silicon resonators were successfully demonstrated operating at frequencies from 30 to 100 MHz with quality factors as high as 8,400 in vacuum [13]. It is further proven that a bandpass filter with 4 dB insertion loss and 1.7% bandwidth at 37 MHz can be realized using the free-free beam resonator as the building block as shown in Figure 1.3 [14].

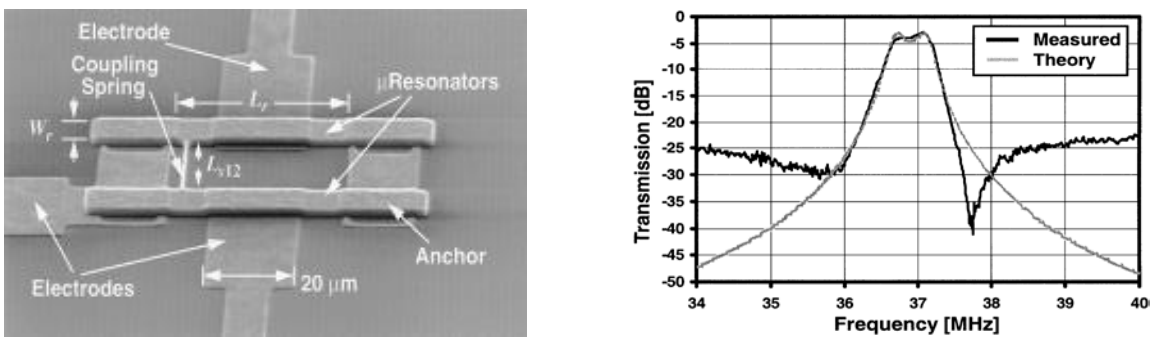

(a) (b)

Figure 1.3 – (a) A 37 MHz VHF free-free beam mechanical filters. (b) Transmission response of the filter measured under 50 μtorr and the equivalent model simulation.

1.4.1 Electrostatically-Transduced MEMS Resonators

As the need for frequency got pushed higher and higher, it is necessary to scale down the structure's geometry to meet the demand, however, these actions bring unfavorable effects upon the traditional MEMS beam vibrating structures. As the dimension of the mass body goes down, its anchor started to become in-dismissible, such that it created mass loading effect on the structures, lowering the *Q*, deteriorates the intended designs. Moreover, these types of devices require to work under vacuum in order to obtain its optimum performances at higher frequencies. To address these issues, Clark introduced the contour-mode MEMS resonator. Opposite to the

beam type resonator, its electrostatic force was being supplied to the structure in the lateral direction causing the mass body to expand/contract along its radius/length/width. Clark was able to demonstrate mechanical resonator at 156 MHz with Q exceeding 9,400 under atmospheric pressure [15]. Another major benefit of contour-mode actuation scheme is the device size. Under the same operating frequency, the footprint of a contour-mode resonator is still larger than the beam type, in other words, it has more headroom to scale down to further pursue higher operating frequencies.

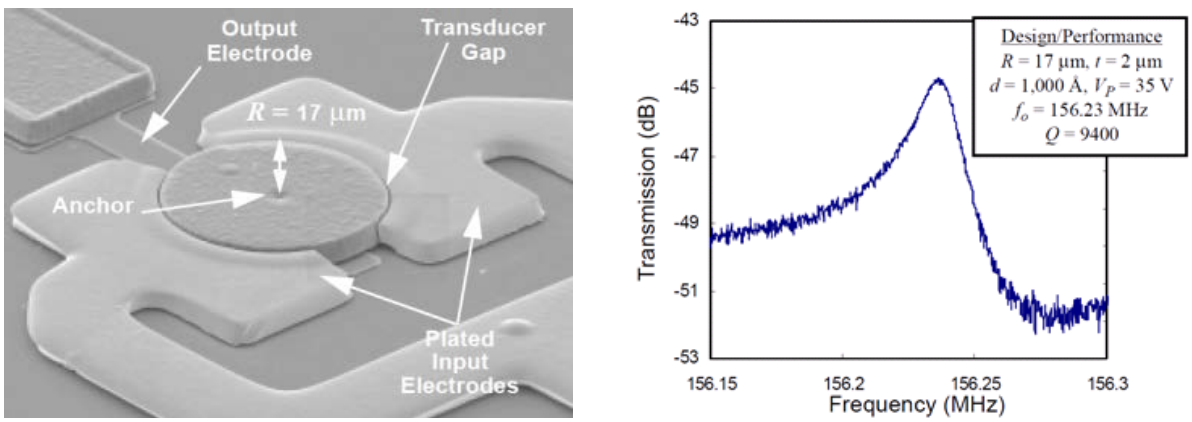

(a) (b)

Figure 1.4 – Micromechanical contour-mode disk resonator operating at 156 MHz under atmospheric pressure. (a) SEM image of the resonator. (b) Transmission response.

One of the most important breakthroughs in capacitive resonator should be credited to Wang's work on the self-aligned radial contour-mode disk resonator. The self-aligned stem introduced by Wang pushed the performance of such device to the next level. With the incorporation of nano-crystalline diamond (NCD), the disk resonator was able to show *Q* at around 3000 while resonating at 1.156 GHz under atmospheric pressure [16]. The novel design in the self-aligned anchoring stem and implementation of diamond material helped reduce the mechanical loss significantly allowing resonator to have extremely high *Q* while not sacrificing any aspects of the power handling and structure size. Following the radial contour-mode

resonator, the wine glass mode disk resonator was demonstrated [17]. Albeit operating at a lower frequency, its unique resonating mode allows the resonator to have non-intrusive anchoring scheme resulting in *Q* exceeding 100,000 at 74 MHz [5].

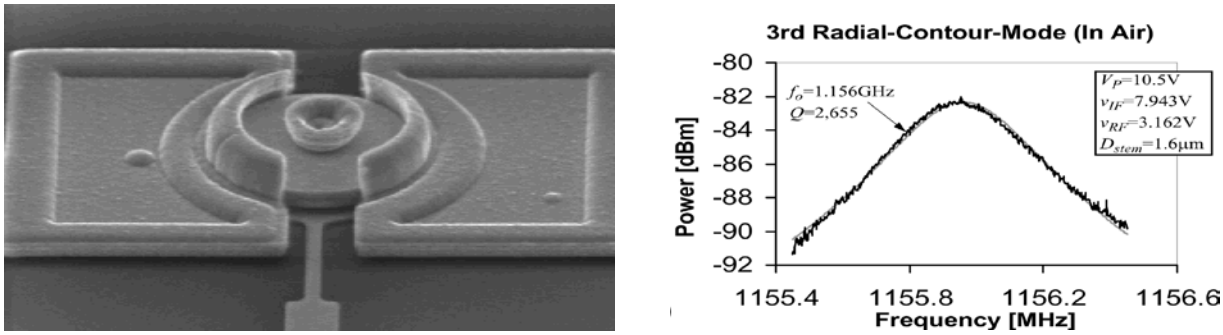

(a) (b)

Figure 1.5 – (a) SEM image of a self-aligned radial contour-mode disk resonator. (b) Frequency response of the resonator at its 3rd order mode resonating frequency – 1.156 GHz.

Despite the high-*Q* and frequency range achieved by radial contour disk resonators, their large motional impedance (> 1 MΩ) is far too high to be integrated with conventional 50 Ω RF components. Several strategies have been proposed such as replacing the capacitive air gap that is employed by most of capacitively-transduced resonators with a solid gap filled by high-k dielectrics or reducing the gap to sub-micron range (<100 nm). Capacitive resonators with sub-100 nm air and solid gaps operating at VHF and UHF range have been successfully demonstrated with *Q* as high as 20,000 and motional impedances less that 10 kΩ [18-20].

In 2009, Weinstein *et al.* [21] introduced a longitudinal-mode silicon acoustic resonator with internal dielectric films. A 6.2 GHz electrostatically-transduced silicon bar-shaped resonator with 15 nm nitride solid gap and quality factor above 4,000 has been demonstrated. As shown in Figure 1.6, the frequency-*Q* product of 3.1×10^{13} at 4.7 GHz is the highest ever reported in micromechanical resonators [17].

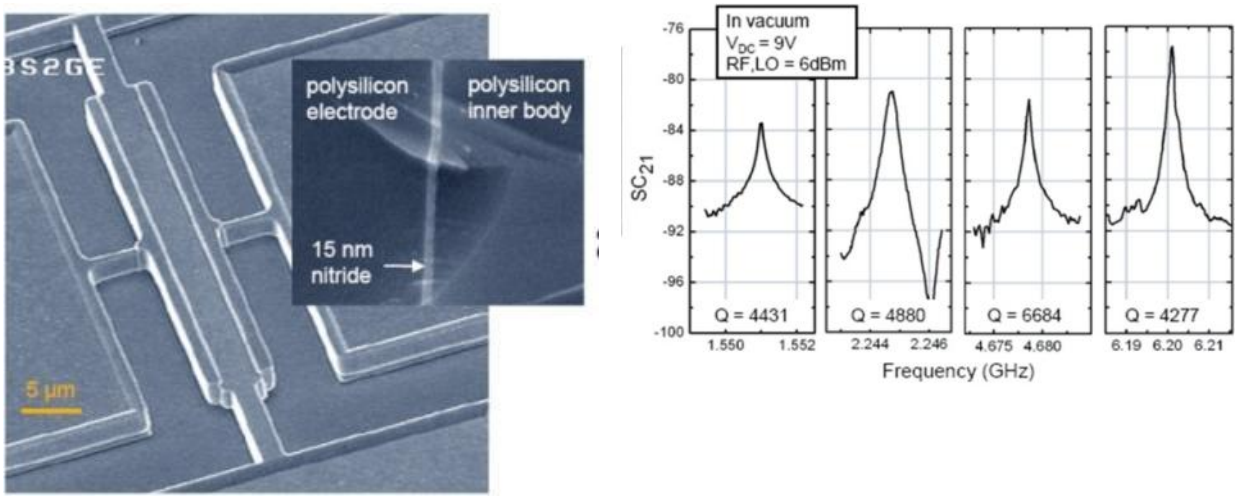

(a) (b)

Figure 1.6 – (a) SEM image of an internal dielectrically-transduced resonator. (b) Frequency response at different resonant frequencies.

Even with all these efforts in pushing the envelope of the performances for capacitive MEMS resonator, there has always been another underlying problem: its complex fabrication process. In order to achieve precise anchor alignment and sub-micron capacitive gap junctions, often time it requires sophisticated fabrication process and demanding techniques. To deal with this problem, Pourkamali *et al.* [22, 23] have demonstrated techniques such as thick oxide mask and trench refill to simplify the fabrication of such resonators. However, the trade-off for the simplified process is usually the ultimate gap size. When shooting for sub-micron nano-gap, aspect ratio of the trench becomes a major concern. The side wall of high aspect trenches often experiences striation and taping effect causing variation in gap distance along the top and the bottom. On the other hand, gap reduction technique often resulted in non-uniform gap shrinkage. The top of the trench got reduced faster than the bottom creating air pocket. Although these techniques can produce gap as small as 100 nm, it is still quite challenging to push for the minimum gap junction 50 nm or below.

1.4.2 Piezoelectrically-Transduced MEMS Resonators

Another popular type of resonator is the piezoelectric material based vibrating structure. Unlike the capacitive based resonator, which will work with most of the conductive materials (metal, polysilicon, doped diamond, *etc.*), piezoelectric resonator's working principle relies on the piezoelectric effect of certain material where charges are generated when deformed, and vice versa. Some of the most common materials are Zinc Oxide (ZnO), Aluminum Nitride (AlN), Barium Titanate and Lead-Zirconate-Titanate (PZT). These types of material offer order of magnitude higher electrical mechanical coupling coefficient than their capacitive counter parts. As a result, lower motional impedance can be easily obtained, hence making the piezoelectric the dominant technology within the current RF/MW wireless applications.

Due to the aforementioned advantages, piezoelectric resonators such as surface acoustic wave (SAW) and bulk acoustic wave resonator (BAW) have already been implemented in mass consumer electronics, which are currently the two most important classes of piezoelectric resonators.

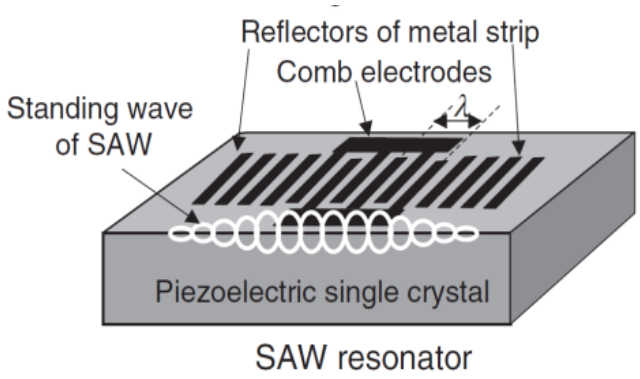

Figure 1.7 – Schematic of a typical SAW resonator.

SAW devices are highly capable at frequency lower than 2 GHz (Figure 1.7). However, as current mobile communication kept on pushing for higher frequency and more spectrum real

estate, SAW devices have reached its limit. As frequency approaches 3 GHz, SAW devices' *Q* dropped dramatically, and its electrodes approach sub-micron scale making it economically unfeasible for mass production [24].

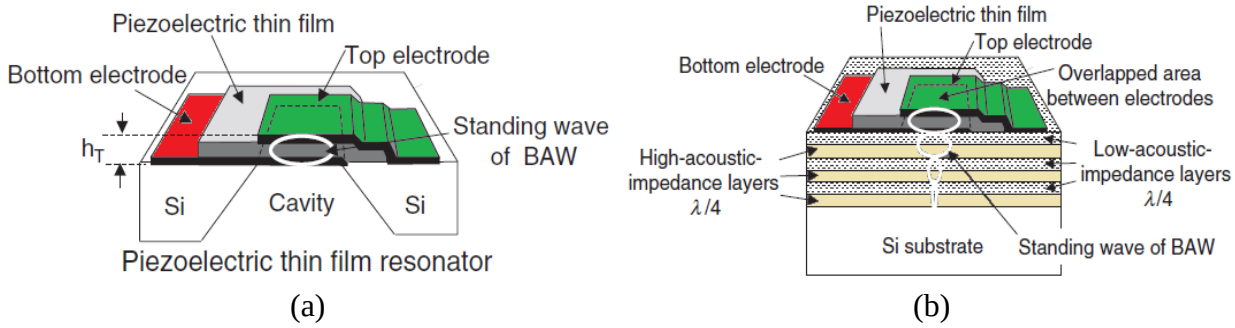

Figure 1.8 – BAW resonators with different types of acoustic isolation mechanisms: (a) air cavity, and (b) Bragg's Reflector.

On the other hand, BAW resonators (Figure 1.8) have attracted attention since its introduction by Lakin *et al.* [25], due to its simple electrode design, higher quality factor, sharp-cut off characteristic, high frequency range, and the possibility of realizing monolithic filters devices with active RF devices. At the moment, two main variants of BAW filters have been successful commercialized on the wireless market: film bulk acoustic wave resonator, FBAR [26], in which the resonant structure isolated from the carrier substrate via air gaps, and solid mounted bulk acoustic resonator (SMR) [27], which uses Bragg acoustic reflectors as method of isolation. Nonetheless, despite BAW devices' astounding performances, it still suffers one major flaw: the operating frequency is determined by the piezoelectric film's thickness. Therefore, in order to achieve precise frequencies, the thickness of the piezoelectric film must be accurately controlled. For this reason, single-chip multi-frequency selective array cannot be fabricated on the same substrate. Accordingly, the BAW device is often dealt as an off-chip component undermining the goal of integrating RF MEMS with transistor circuits. Nevertheless, the present-

day telecommunication progression demands for single-chip multi-frequency transceivers that operate over a wide range of services as opposed to discrete components integrated on board level.

Similar to the evolution of capacitively-transduced counterparts, contour-mode excitation method also finds its place in the piezoelectric material based resonators. Piazza *et al.* introduced and have successfully demonstrated a contour-mode piezoelectric resonator (see Figure 1.7 below) [28-30]. Multiple AlN resonators with operating frequency ranging from 23 MHz to 230 MHz have been demonstrated with high *Q* (around 4000) and low motional impedance (50 to 700 Ω). These single resonators were also cascaded into L-ladder network yielding low loss (I.L. ~ 4 dB) and high rejection bandpass filters. Its operating frequency was determined by its lateral dimension which makes single-chip multi-frequency implementation feasible, and yet it still retained all the advantageous characteristic of a BAW device (low motional resistance, high *Q*, and flexible frequency range).

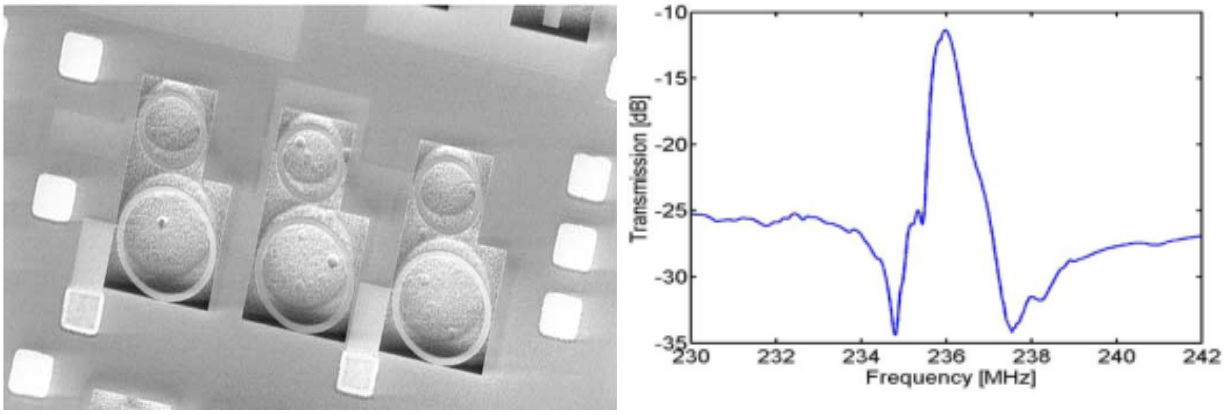

(a) (b)

Figure 1.9 – (a) SEM image of a bandpass filter formed by piezoelectric resonator in L-ladder configuration. (b) Transmission response of the filter.

A conventional piezoelectric device uses the piezoelectric material itself as the resonant body structure. Unfortunately, its material advantages (high mechanical coupling coefficient)

also become its very own drawback, namely, unsatisfactory mechanical properties. A mechanical resonator's operating frequency is highly dependent upon the structure body's Young's modulus and material density, and as mentioned before, there are only three kinds of material suitable for piezoelectric resonators, which, ultimately, restricted the development of such technology in higher frequency domain. In order to relieve this issue, Abdolvand introduced a new generation of piezoelectric resonator called thin-film piezoelectric-on-substrate (TPoS) resonators, which separated the driving and resonating aspects of a mechanical resonator by putting a thin layer of piezoelectric on top of a Si body [31]. By combining piezoelectric material's high electrical mechanical coupling and Si's superior mechanical properties, a low motional impedance mechanical resonator with *Q* on par to the capacitive counterpart were successfully demonstrated. TPoS Resonator has been utilized to fabricate UHF filters in a single substrate. Using the same technology, thickness mode filters have also been demonstrated at frequencies ranging from 600 MHz to 3.4 GHz with motional impedance less than 700 Ω as shown in Figure 1.5 below [32, 33].

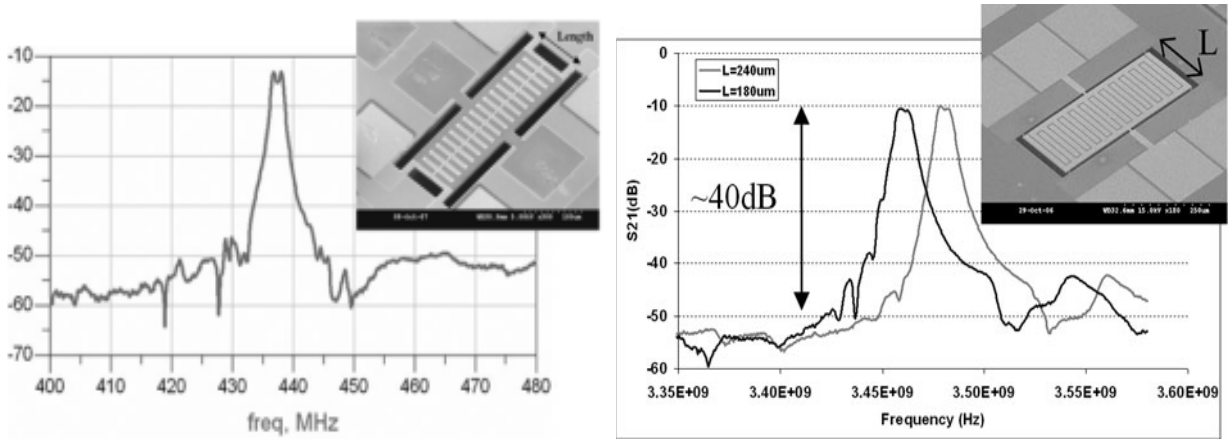

(a) (b)

Figure 1.10 – (a) Electrical response and SEM image of a 435-MHz of lateral monolithic filter. (b) Measured frequency response plots and the SEM picture of 3.5 GHz thickness mode monolithic TPoS filters.

1.5 Summary of Current State of the Art

There is no doubt capacitively-transduced micromechanical resonator can achieve quality factor and operating frequency that cannot be matched by piezoelectric counterparts. However, these devices usually suffer from high motional impedance which leads to high insertion loss if interfaced with standard RF 50 Ω system. Although efforts have been made in reducing the motional impedance by shrinking the actuating gap down to sub-100 nm, its highly complex fabrication process still poses as a challenge when compared to its piezoelectric counterparts. Moreover, the process often involved the use of non-standard semi-conductor processing materials and equipment. In order to achieve the goal of true integration between capacitive MEMS resonator and CMOS circuitry, the fabrication process need to do without the use of such exotic materials and equipment.

MEMS resonator based on piezoelectric effect have already reached a phase of maturity. As SAW and BAW devices have been produced in large volumes and used in mass-produced commercial electronics for more than a decade. Nonetheless, they are still off-chip component that won't be able to satisfy the need for the much more demanding system-on-a-chip applications. Instead, contour-mode piezoelectric resonators have been demonstrated to be the idea technologies at VHF and UHF with moderate Q and low insertion loss. However, their performances still rely vastly on the mechanical and electrical properties of the piezoelectric layer, which limited the freedom of design. Though piezoelectric variations such as TPoS configuration mitigate the limited material selection, it sacrifices some its electrical mechanical coupling.

1.6 Dissertation Organization

This dissertation is organized into six chapters. The first chapter presents an overview of the current state of the art technologies and describes the goals of this dissertation research. Chapter 2 reviews fundamentals and basic formulations for both piezoelectric and capacitive types of resonators. Additionally, the equivalent mechanical and electrical lumped circuit representation for the MEMS resonators are presented here as well.

The micro-fabrication process and experimental results for the piezoelectric resonators and filters are detailed in Chapter 3. Similarly, the micro-fabrication process and experimental results for capacitively-transduced resonators are shown in chapter 4. Chapter 5 presents several ideas such as single-mask nano-gap capacitive resonator, dual-transduced resonator, and frequency tuning enabled by the use of silicon-on-insulator (SOI) wafers. Studies of substrate resistivity's impact over the performance of the fabricated resonators are shown in this chapter as well.

Chapter 6 summarized the results and the accomplishments of this work. In addition, possible directions for future research topics are presented in the end.

1.7 Contributions

The main contribution from this dissertation work is the complete study of both types of resonators. Both piezoelectric and capacitive resonators have been fabricated, measured, and studied. Both resonators are fabricated under the utmost identical conditions, using the same substrate and undergo the same process equipment and materials, which, to the author's best knowledge, yield the most unbiased comparison study of both resonators to date. The study of the substrate resistivity's impact is much clearer since the comparison test is carried out on the

same substrate. It sheds more lights on which type of resonator is more prone to the feedthrough parasitic.

Two innovative ways to simplify the fabrication process for capacitive resonator with nano-meter dielectric gap have been demonstrated. By combining the techniques of chemical mechanical polishing (CMP) and deep reactive ion etching (DRIE), it is possible to produce sub-100 nm gap resonator within one or two photolithography steps.

In addition, a robust and high-yield micro-fabrication process for thin-film ZnO-on-silicon resonators has been successfully developed. The process is compatible with standard CMOS foundry process with thermal budget well below the required 400ºC, which facilitates future monolithic transceiver integration between RF MEMS and CMOS electronics.

This work also demonstrates a tunable piezoelectric resonator. Not only the tuning mechanism is reversible, it is also fairly simple to achieve such configuration due to the use of silicon-on-insulator (SOI) wafer. Substrate's resistivity impact on both types resonator is studied, and equivalent model is developed to aid future design of MEMS resonator. Moreover, efforts have been made in attempting to create a brand new concept of resonator by combining both piezoelecrtric and capacitive driven mechanisms into one dual-transduced resonator.

Chapter 2

Background

Electrostatically- and piezoelectrically-transduced resonators use two different types of driving mechanism, but their working principals are essentially the same. In either type of resonator, the goal is to excite the vibration body system into resonance mode by supplying mechanical forces that match the mechanical structure's resonance frequency. In piezoelectric resonator, the mechanical excitation is provided through piezoelectric material itself. When electric field is applied to the piezoelectric thin film, the film is then deformed accordingly. If said sinusoidal electric field matches the resonance frequency of the mass body, the structure is then driven into its resonating mode. This behavior is called piezoelectric effect. On the other hand, an electrostatic (also known as capacitive) resonator operates in the same way. The goal is to drive the mass body, usually a conductive material, into resonance mode. However, since capacitive resonator does not have the advantage of built-in characteristic like piezoelectric effect, it requires the use of external electrostatic force to supply the necessary mechanical excitation to drive the mass body into resonance.

Detailed discussion with regards to the resonance frequency, piezoelectric effect, and material properties are presented in this chapter. Mechanical and electrical equivalent model are also provided to facilitate the simulation of MEMS devices as an electrical circuit component in hope of aiding integration between MEMS and conventional electronic circuitry.

2.1 Piezoelectric Effect

Piezoelectricity was first discovered in 1880 by the brothers Pierre Curie and Jacques Curie. Following the discovery, the first engineering application using piezoelectricity characteristic was an ultrasonic sensor for submarine detection in 1916 by Paul Langevin. Eventually, this leads to the invention of mechanically vibrating crystal knows as the quartz crystal, which is now implemented in many engineering applications such as microphones, sensors, transducers, and frequency/timing circuits. Most importantly, quartz crystal has become the building block for the ever continuously growing radio-telecommunications industry. The piezoelectric effect is understood as the linear electromechanical interaction between the mechanical and the electrical state in crystalline materials with no inversion symmetry [34]. When a mechanical stress/force is applied to the piezoelectric material, the material is able to generate an electric charge. This behavior is known as the direct piezoelectric effect. Conversely, one can generate mechanical deformation in a piezoelectric material by supplying an electrical field. This is behavior is known as reverse piezoelectric effect. Piezoelectric effect is a reversible energy conversion mechanism. Figure 2.1 below summarize the phenomenon of piezoelectric effect.

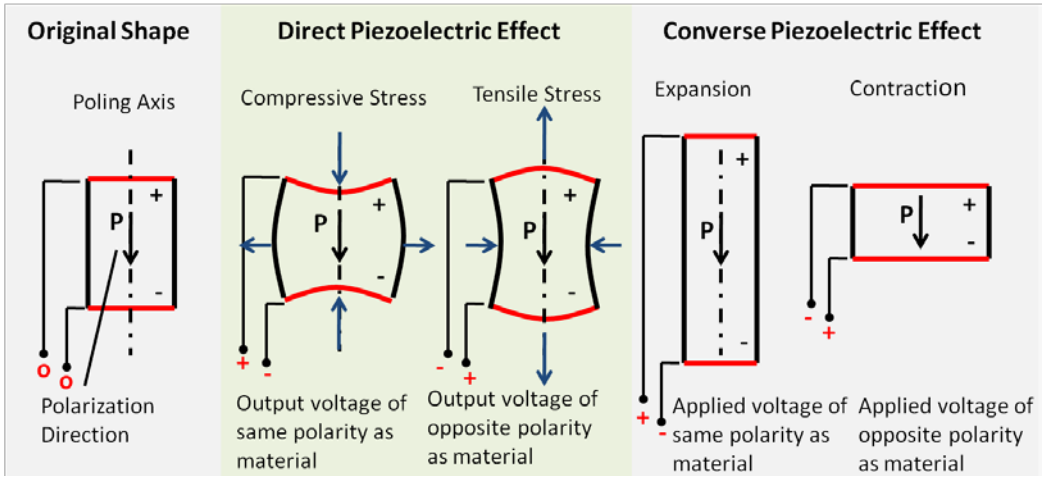

Figure 2.1 – Illustration of the direct and reverse piezoelectric effects [34].

2.2 Piezoelectric Materials

Although there are several ceramic materials that exhibit piezoelectric effect, the most readily available materials are Aluminum nitride (AlN), Zinc oxide (ZnO), Barium titanate ($BaTiO_3$) and Lead-Zirconate-Titanate (PZT). Table 2.1 below summarizes the properties of these materials. $BaTiO_3$ is an excellent material for transducer applications because of its high electromechanical coupling coefficient and ease of fabrication. However, it also has high thermal expansion coefficient and low Curie point prohibiting itself from being further developed. PZT has taken the place of $BaTiO_3$ and become the most used material in off-chip piezoelectric applications due to its high electromechanical coupling factor and low thermal expansion coefficient. However, PZT contains the element of lead, and it is not compatible with many CMOS technology and foundry processes employed today.

Table 2.1 – Properties of most common piezoelectric materials [34-36].

Material	Density (kg/m^3)	Dielectric Constant	Acoustic Velocity [m/s]	Piezoelectric Coefficient d_{31} [pC/N]	Temperature Expansion Coefficient
Quartz	2650	3.8-4.5	3158	2	0.6×10^{-6}/°C
BaTiO3	6020	1500	4800	33.4	0.5×10^{-6}/°C
PZT	7600	400 – 1000	3300	180	-6.0×10^{-6}/°C
ALN	3270	8	11400	1.8	4.5×10^{-6}/°C
ZnO	5766	8.8	6330	4.7	4.0×10^{-6}/°C

Currently, AlN and ZnO are the most used piezoelectric materials in MEMS applications. High quality AlN and ZnO films can be obtained by sputter deposition at a relatively low temperature (< 400 °C) which is compatible with CMOS technology. Unlike PZT, AlN and ZnO are not ferroelectric, where PZT can easily exhibit high electromechanical coupling coefficient without special deposition condition. Both AlN and ZnO require individually tuned deposition conditions in order to obtain quality film with high electromechanical coupling coefficient.

2.3 Mathematical Model of the Piezoelectric Effect

Since piezoelectric materials are anisotropic, their physical properties (*e.g.*, permittivity, elasticity, and piezoelectricity coefficients) are vector quantities. The electrical behavior of a piezoelectric material can be expressed as:

$$D_{3x1} = \varepsilon_{3x3} E_{3x1} \tag{2.1}$$

where D is the electric density displacement, ε is the dielectric constant, and E represents the electric field. Equivalently, the mechanical behavior of piezoelectric materials is modeled using the Hooke's law which describes the stress-strain relationship of material which is given by:

$$S_{6x1} = c_{6x6} T_{6x1} \tag{2.2}$$

where S represents the strain, c is the compliance, and T is the stress. These equations can be combined into a coupled equation, which relate the mechanical and electrical variables and completely described the behavior of piezoelectric materials. The fundamental electro-mechanical coupled equation is given by:

$$T_{6x1} = c_{6x6} \cdot S_{6x1} - e_{6x3} \cdot E_{3x1} \tag{2.3}$$

$$D_{3x1} = e_{3x6} \cdot S_{6x1} - \varepsilon_{3x3} \cdot E_{3x1} \tag{2.4}$$

These sets of equations are known as the stress-charge form of the piezoelectric equations or d-form piezoelectric equations.

2.4 Operating Principle of MEMS Resonators

Outside of excitation force mechanism, there is little difference to how an electrostatic and piezoelectric resonator operates. The resonating frequency/mode of a particular structure is pre-determined by the structure's physical geometry and material's mechanical properties. If given the same geometry and mechanical properties, both piezoelectrically- and electrostatically-transduced resonator will have the same response in resonant frequency.

2.4.1 Piezoelectric MEMS Resonators

A piezoelectrically-transduced MEMS resonator consists of a piezoelectric body suspended from a tethered anchor, and it is sandwiched in-between two metal electrodes as shown in Figure 2.2(a). When a sinusoidal electrical signal is applied, the piezoelectric effect takes place and excites the body mass into motion. These electrodes are strategically patterned and positioned with respect to each application. Depending on the location and size, it is possible to achieve multi-port or multi-mode response for frequency filtering applications.

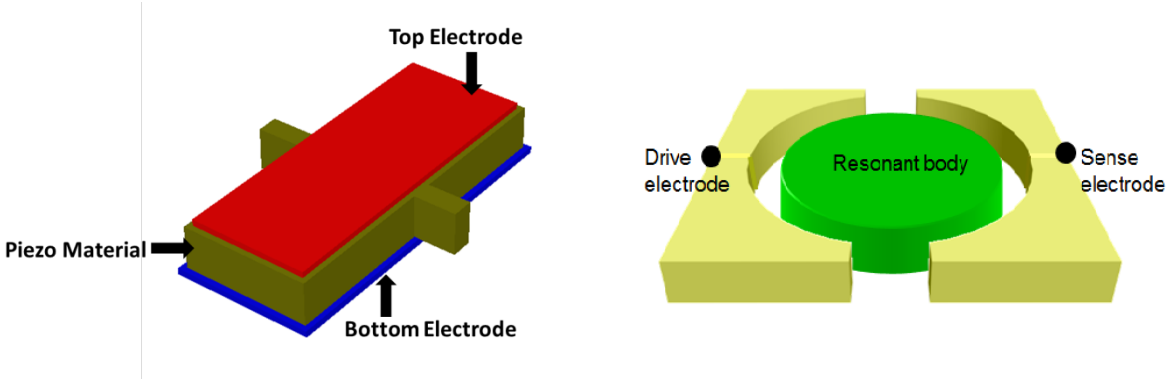

(a) (b)

Figure 2.2 – Schematic-view diagram of a piezoelectric 1-port square-plate resonator (a) and a 2-port circular-disk capacitive resonator (b).

Even with the same pattern of electrodes, the same structure of piezoelectric resonator can be excited in different frequencies. As shown in Figure 2.3, multiple resonating modes can co-exist within one specific structure. A device like Figure 2.2(a) can be actuated either in thickness-mode (by means of d_{33}), lateral shear-mode (by means of d_{15}), or contour-mode (by means of d_{31}).

According to the applications, some situations are desired to have multiple modes to co-exist forming a filter response. Contrarily, some applications require the suppression of all modes other than the targeted frequency to produce the strongest and cleanest signal response.

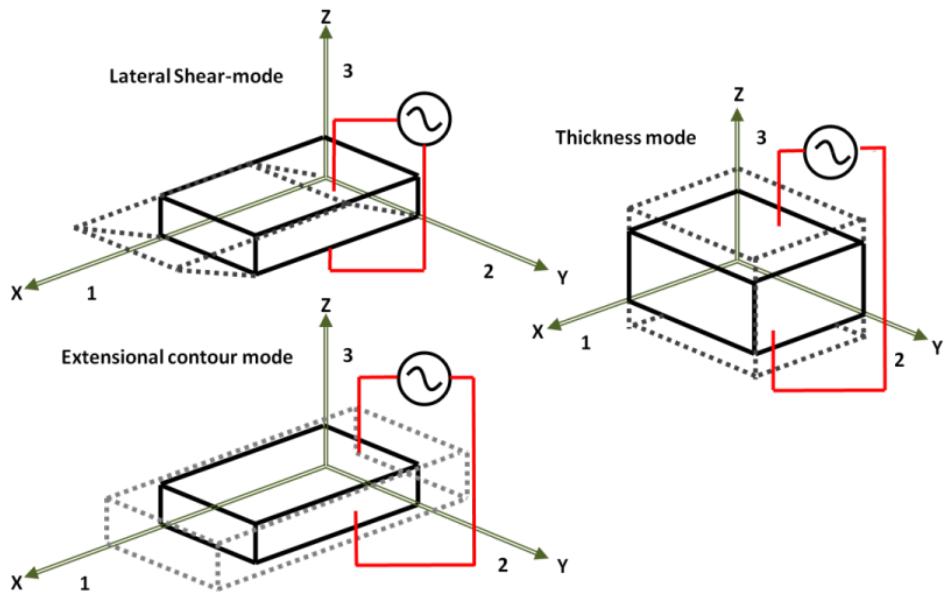

Figure 2.3 – Vibration modes of a piezoelectric rectangular plate resonator [37].

2.4.2 Capacitive MEMS Resonators

Similarly, a capacitive resonator just means the mechanical force is in the form of parallel plate electrostatic force instead of piezoelectric effect. As shown in Figure 2.2(b), the parallel plate surface is formed between the resonant body and the electrode. The gap of the parallel plate has to be small enough so the electrostatic force is more effective to drive the body into resonance mode. Usually, the gap distance is on the order of 100 nm or smaller.

The parallel plate formation is essentially a parallel plate capacitor. Equation (2.5) below shows the total charge (Q) residing within the capacitor, where V is the constant polarization DC voltage between the body and the electrode.

$$Q = V * C \tag{2.5}$$

When a sinusoidal signal is applied, the gap distance is varying with respect to time due to the exerted electrostatic force on the resonating body. Apply differentiation with respect to time to equation (2.5), and the result becomes:

$$\frac{dQ}{dt} = I_{out} = V * \frac{dC}{dt} \tag{2.6}$$

As shown in equation (2.6), the output current (I_{out}) of sense electrode is strongly correlated to the DC bias voltage and the gap capacitance. In other words, the performance of a capacitive resonator relies heavily on the capacitor's dielectric gap material and distance.

2.4.3 Thin-film Piezoelectric-on-Silicon (TPoS) Resonators

An alternative design known as thin-film piezoelectric-on-silicon (TPoS) resonator is shown in Figure 2.4. A TPoS resonator is essentially a piezoelectric resonator sitting on top of a Si mass body. Compared to piezoelectric material, Si is a much superior material with low acoustic loss. When a sinusoidal electric field is applied across the piezoelectric film between the top and bottom electrodes, instead of resonating with the piezoelectric thin film, the device is excited into silicon's resonance mode. The applied electrical field across the piezoelectric-film will drive the Si resonator body to expand and contract through the converse piezoelectric effect. In return, the body's physical deformation induces periodic piezoelectric charges on the surface of the output electrodes. The piezoelectric related resonator works presented in this work are all done in the TPoS configuration.

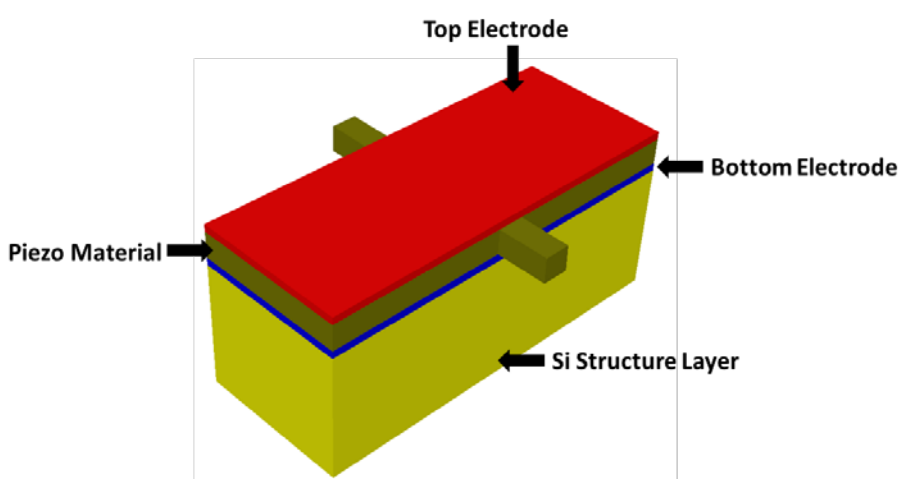

Figure 2.4 – 1-port piezoelectric on substrate resonator

2.5 Contour-Mode Resonators

From Figure 2.3, it is shown that one specific structure can have multiple modes of resonance, and it doesn't matter if it is a piezoelectric or capacitive type. Even for capacitively-transduced resonators, it is possible to form the parallel plate in the vertical direction to excite it in the thickness mode. However, if the device operates in the thickness mode, it is then called a FBAR device, where the thickness of the piezoelectric film determines the resonating frequency. As mentioned in previous chapter, FBAR is not desired for multi-frequency integrating applications since the thickness only allows one operating frequency. For devices operating in shear-modes, the electrical field must be applied perpendicular to edges of the plate in order to drive the structure into resonance, which is a very challenging feat, thus complicating the fabrication process.

For the contour-mode, the resonance frequency is set by the lateral dimension (*i.e.* radius, length, width) of the structure. Such dimensions can be precisely and easily defined by the device CAD layout, All the resonator studies presented in this work are designed to operate in the contour-mode. Most of the designs are in the shape of circular disk and rectangular plate.

2.5.1 Contour-Mode Circular Disks

Figure 2.5 presents the finite element modal analysis of a 60 µm-diameter ZnO TPoS resonator using CoventorWare. The structure consists of 15µm-thick silicon device layer, a 500 nm-thick ZnO piezoelectric film, and a set of top and bottom metal electrodes. This configuration permits the excitation of the radial contour-mode and the wine glass mode that operates at different resonance frequency. To minimize the loss of acoustic energy through the anchor (not shown here), it is the best practice to place the anchor at a nodal point (blue part in the simulation figures) where it has the least amount of displacements. If such locations are in-

accessible, the anchor dimensions are best designed to have the smallest width that is possible, and with length equals to multiples of quarter wavelength with respect to the resonance frequency. A simplified frequency equation for a disk resonator vibrating in a radial contour-mode is given by [38]:

$$f_o = \frac{\alpha}{R}\sqrt{\frac{E_p}{\rho_p(1-\mu^2)}} \tag{2.7}$$

where E_p , ρ_p and μ represent the material's Young's modulus, density and Poisson's ratio of the structural material respectively. R is the radius of the disk, and α is a mode dependent scaling factor. For example, if $\mu = 0.3$, then α equals to 0.342 and 0.272 for the first radial contour-mode, and the fundamental wine glass mode, respectively.

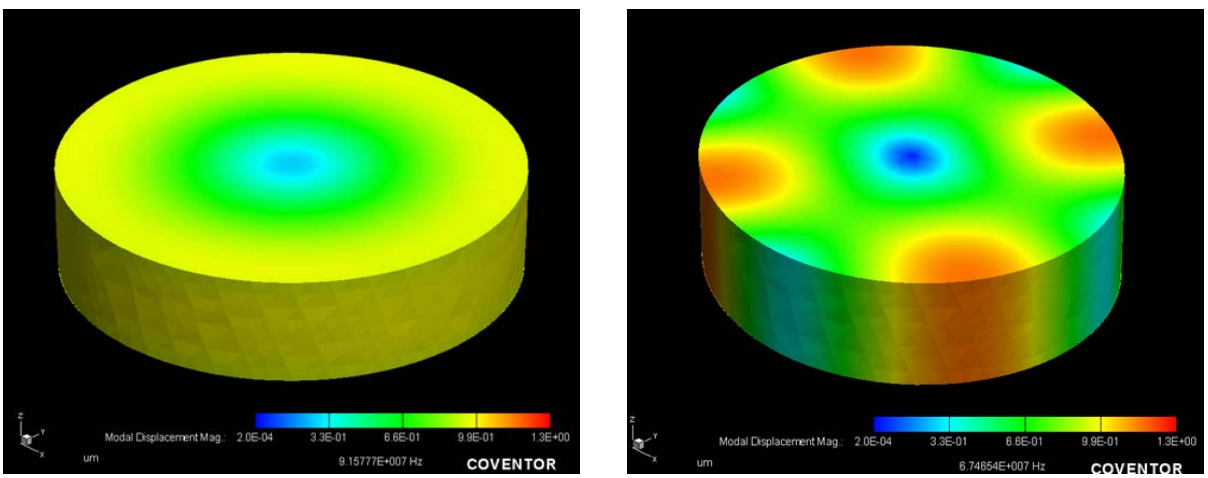

(a) (b)

Figure 2.5 – Finite-element simulation of a ZnO-on-silicon disk resonator in its (a) fundamental radial contour-mode at 91.5 MHz and (b) wine-glass mode at 67.5 MHz.

In idea situation, the mechanical vibrating body should only consists of only the mechanical vibrating mass, however, without proper circuitry such as electrodes and transducers, one cannot function as a proper electrical device. Therefore, it is inevitable to attached extra weight (*i.e.* electrodes) to the mechanical vibrating body, thus the term mass loading effect. The

add-on weight tends to damp the total acoustic energy which degrades the overall performance. In order to model the mass loading effect more effectively, the resonance frequency Equation (2.7) is modified as below:

$$\rho_{eq} = \frac{\rho_{top}T_{top} + T_{bott}\rho_{bott} + \rho_p T_p + \rho_{dev}T_{dev}}{T_{top} + T_{bott} + T_p + T_{dev}} \tag{2.8}$$

$$v_{eq} = \left[\frac{E_p T_p + E_{top}T_{top} + E_{bott}T_{bott} + E_{dev}T_{dev}}{\left(\rho_{top}T_{top} + T_{bott}\rho_{bott} + \rho_p T_p + \rho_{dev}T_{dev}\right)(1-\mu^2)}\right]^{1/2} \tag{2.9}$$

$$f_o = \frac{\alpha}{R} v_{eq} \tag{2.10}$$

where v_{eq} and ρ_{eq} represents the equivalent acoustic velocity and equivalent density of the resonator of a TPoS resonator structure respectively. Substitute the equivalent mass and velocity into Equation (2.7) comes Equation (2.10).

A similar analysis could be carried out for equivalent Poisson's ratio. However, for simplicity, a Poisson's ratio of $\mu = 0.3$ has been kept as constant. The changes in Poisson's ratio have little impact on the overall frequency shift. The mechanical properties of the materials used for the development of MEMS resonators in this work are listed in Table 2.2.

Table 2.2 – Mechanical properties of materials used for the development of MEMS resonators.

Material	Young's Modulus (GPa)	Density (Kg/m^3)	Poisson's ratio
Si	170	2329	0.226
ZnO	123	5676	0.330
Al	70	2700	0.350
Pt	168	21450	0.380

The equivalent mass, M_{eq}, can be obtained by dividing the total kinetic energy by one half of the velocity square at any location of the micromechanical resonator [39]. The mass at the disk perimeter can then be obtained using the relation:

$$M_{eq} = \frac{2\pi\rho_{eq}T_{eq}\int_0^R J_1^2\left(\frac{\omega_n}{v_{eq}}r\right)dr}{J_1^2\left(\frac{\omega_n}{v_{eq}}r\right)} \tag{2.11}$$

where J_1 is the Bessel function of the first kind. The contour-mode electromechanical coupling coefficient can then be calculated as:

$$\eta = \frac{Q_{Total}}{u_{max}} = \frac{2E_p}{1-\mu}\iint\left(\frac{\partial u_r}{\partial r} + \left(\frac{u_r}{r} + \frac{1}{r}\frac{\partial u_\theta}{\partial \theta}\right)\right)dA \approx E_p d_{31}\pi\frac{R}{2} \tag{2.12}$$

Please note Equation (2.12) is derived specifically for the circular disk resonator with two splitted top electrodes that each covers half of the resonator body.

2.5.2 Contour-Mode Rectangular Plates

For a contour-mode rectangular plate resonator as shown in Figure 2.6, the resonance frequency can be calculated from a series of differential equations knows as the wave equations [38]. It is worth noting that the example given here is greatly simplified, but this analysis method can be extended to different geometries and mode shapes.

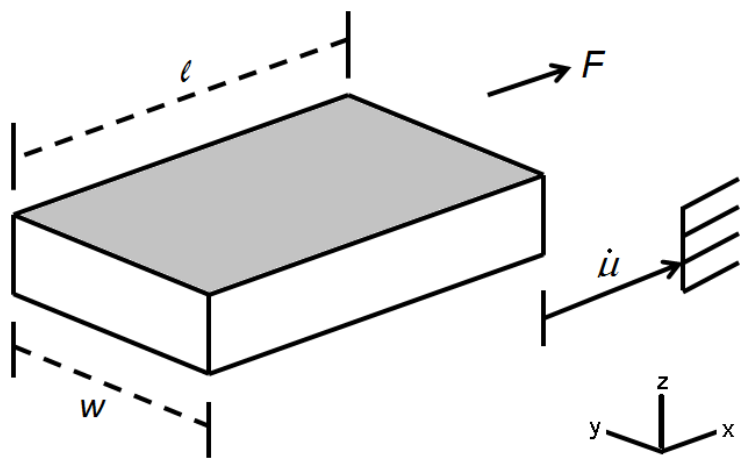

Figure 2.6 – Longitudinal-mode rectangular plate resonator [40].

Please refer to R. A. Johnson *et al.* [38] for a more detailed analysis of this technique. The analysis for the rectangular plate starts with the wave equation:

$$\frac{E}{\rho}\frac{\partial^2 u}{\partial x^2} = -\omega^2 u \tag{2.13}$$

where E, ρ, u, represents the Young's modulus, density of the material, and the displacement, respectively. Using the theory of linear differential equations, the general solution to Equation (2.13) is expressed as follows:

$$u(x) = A \sin kx + B \cos kx \tag{2.14}$$

where x is the coordinate in the length direction, and k is the propagation constant. By applying boundary condition, x = 0, to Equation (2.14), the value of A can be found as:

$$\left.\frac{\partial u}{\partial x}\right]_{x=l}^{x=0} = Ak \cos kx - Bk \sin kx = 0 \tag{2.15}$$

$$Ak \cos kx - 0 = 0, \text{ or } A = 0 \tag{2.16}$$

$$u(x) = B \cos kx \tag{2.17}$$

Applying the boundary condition at $x = l$ to Equation (2.15), it gives:

$$\sin kl = 0, \text{ for } k_n l = n\pi, n = 1,2,3, \ldots.. \tag{2.18}$$

By substituting Equation (2.17) in the wave Equation (2.13), term k can be expressed as follows:

$$k = \omega\sqrt{\frac{\rho}{E}} \tag{2.19}$$

Next we substitute the values of k_n from Equation (2.18) into Equation (2.19) and solve for the frequency, then it gives the resonance frequency of a rectangular plate vibrating along its length in the nth mode:

$$f_n = \frac{n}{2l}\sqrt{\frac{E}{\rho}} \tag{2.20}$$

2.6 Mechanical Resonator Modeling

Over the years, a vibration mechanical system consists of spring, mass, and damper has been associated directly with electrical system analog. A mechanical resonator is no different than a convention mechanical vibrating system albeit the micro-scale size. Therefore, it is possible to define the mechanical behavior of MEMS resonator by equivalent electrical components using mechanical-electrical analogy. A spring and mass within a mechanical system store energy as potential and kinetic energy, just like capacitor and inductor store energy in electric and magnetic field. Similarly, a mechanical damper dissipates energy into heat, just as a resistor dissipate current into heat. Regardless of the shape or type of the MEMS resonator, this analogy is always applicable. Table 2.3 summarizes the analogy between the mechanical and electrical domain, where mechanical parameters such as force and velocity correspond to electrical variables such as voltage and current.

Table 2.3 – Direct analogy between electrical and mechanical domain

Mechanical Domain		↔	**Electrical Domain**	
Force	F	↔	Voltage	V
Velocity	$\dot{u}$	↔	Current	I
Mass	M_{eq}	↔	Inductance	L_m
Compliance	$1/K_{eq}$	↔	Capacitance	C_m
Damping	C_{eq}	↔	Resistance	R_m

Using the electrical-mechanical analogy, the lumped-element mechanical model representation (Figure 2.7(a)) can be transformed entirely using electrical lump elements (Figure 2.7(b)). The equivalent electrical circuit consists of a series LCR tank, two transformers, and an input/output port capacitance. The two transformers here represented the electro-mechanical coupling efficiency (η) of the MEMS resonator. With the electric equivalent model identified, the task of integrating MEMS devices and convention circuitry has become much more feasible.

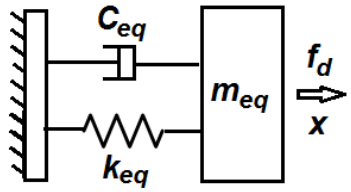

(a)

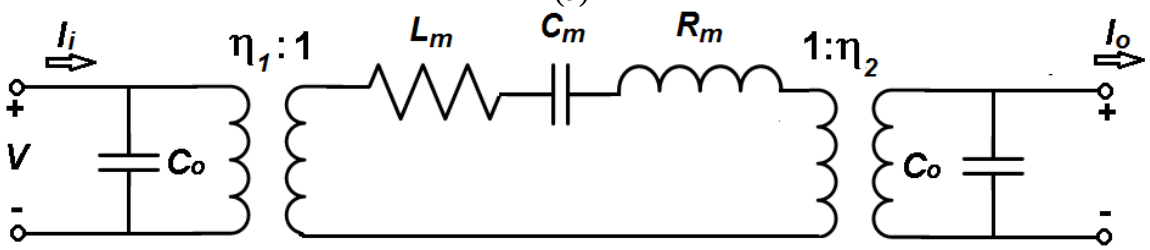

(b)

Figure 2.7 – Equivalent lumped-element model of a micromechanical resonator [40]. (a) Equivalent mass-spring-damper model; (b) Equivalent LCR circuit model.

2.7 Model Parameters for Equivalent Electrical Circuit

Continuing from previous section, the equivalent electrical parameters of a resonator can be extracted given the properties from the mechanical domain. The example given here is for a rectangular shaped resonator device only. For the case of a rectangular piezoelectric plate vibrating along its length, the electrical parameters can be calculated by [28]:

$$M_{eq} = \frac{\rho l w T}{2} = \frac{M_{static}}{2} \tag{2.21}$$

$$C_{eq} = \frac{\omega_n M_{eq}}{Q} \tag{2.22}$$

$$K_{eq} = \omega_n^2 M_{eq} \tag{2.23}$$

where w, l and T are the width, length and thickness of the resonator respectively. Q is the quality factor, and ω_n is the resonant frequency for the nth resonance mode. The electromechanical coupling coefficient can be determined as:

$$\eta = \frac{Q_T}{u_{max}} \tag{2.24}$$

where Q_T is the total charge induced on the electrodes, and u_{max} is the maximum displacement. With the use of Table 2.3, mechanical variables can now be converted into electrical parameters as follows:

$$R_m = \frac{C_{eq}}{\eta_1 \eta_2} \tag{2.25}$$

$$C_m = \frac{\eta_1 \eta_2}{k_{eq}} \tag{2.26}$$

$$L_m = \frac{M_{eq}}{\eta_1 \eta_2} \tag{2.27}$$

Chapter 3

Development of Piezoelectrically-Transduced Resonator

One of the major advantages of piezoelectric based resonator over capacitively-transduced resonator is the simplified fabrication process. Due to the piezoelectric effect from the material itself, the resonator body can deform upon the presence of an applied electric field without the need of complex sub-micron parallel plate gap setup.

Another advantage of piezoelectrically-transduced micromechanical resonator is their potential to be monolithically integrated with current CMOS technology. One of the major challenges of post-CMOS integration is that the process temperature for the MEMS fabrication has to be kept below 400 °C which is the allowable thermal budget of CMOS circuitry. As mentioned before, the most common type of piezoelectric material are ZnO, AlN, and PZT. Since PZT contains the element of lead, it render itself incompatible with most of the state of the art CMOS devices and foundry process. Subsequently, it makes ZnO and AlN become the most widely chosen material in the past decade for FBAR and SAW devices. However, due to the need of multi-function and multi-frequency in modern day systems, contour-mode type of devices have more appeal to the future.

The fabrication process utilized to manufacture the piezoelectrically-transduced resonators studied in this work is presented in this chapter. Based on the type of the wafer used, two different types of piezoelectrically-transduced resonator can be obtained. If a bare silicon wafer is used, the resonator is called the piezoelectric thin film resonator where the piezoelectric

material serves as both the transducing and resonating elements. If silicon-on-insulator (SOI) wafer is used, the end product will be considered as TPoS, where silicon is used as resonanting structure, and ZnO film is used as the piezoelectric transducer. All the piezoelectric related resonator works reported in this work are all done in the TPoS configuration.

3.1 Selection of Material

The final material used in the development of micro-mechanical resonator in this work was made after considering device performance, available tools, and ease of processing in the Nanotechnology and Research Education Center (NREC) at the University of South Florida. Two materials were initially considered and tested: ZnO and AlN. PZT was not even considered though it provides the highest transverse piezoelectric coefficient (d_{31}) and shall yield the best device performance, but the lead element within PZT tends to contaminate the processing equipment, which is not suitable for a multi-user facility like NREC. AlN has the higher acoustic velocity and relatively low acoustic losses when compared to ZnO, nevertheless, it requires chlorine gas based reactive ion etching system in order to pattern the AlN film which is not available at our school.

ZnO is ultimately selected for the development of resonator due its ease of processing. Compared to AlN sputtering deposition, ZnO does not require the use of reactive ion sputtering, and it can achieve 100 nm/hr deposition rate, whereas the rate for AlN is merely 30 nm/hr based on our preliminary experiment. Considering the resonator will require up to 400 to 700 nm thick of piezoelectric layer, ZnO is the obvious choice. Another advantage of ZnO is the availability of CH_4/Ar dry etching recipe offered by the deep reactive ion etching (DRIE) system. This enablement is critical in producing piezoelectric resonators, since dry etching provides more

precise control over dimensions and exhibit nearly straight sidewalls. Table 3.1 summarizes the important properties of the three most common piezoelectric materials.

Table 3.1 – Properties of piezoelectric materials

Material Properties		**ZnO** [34]	**PZT** [35]	**AlN** [35]
Density [kg/m^3]	ρ	5676	7600	3260
Young's Modulus [GPA]	E	123	53	330
Acoustic Velocity [m/s]	v_p	6630	3300	10400
Poisson Ratio	μ	0.18 – 0.36	0.25 – 0.31	~0.24
Piezoelectric Strain Coefficient [pC/N]	d_{31}	-4.7	-130	-1.8
Electrical Resistivity [Ω·cm]	ρ_e	$10^8 - 10^9$	$10^7 - 10^9$	$10^{10} - 10^{14}$

3.2 ZnO Characterization

The key to achieve the highest performance of the ZnO resonator is obtaining a high transverse piezoelectric coefficient (d_{31}) piezoelectric film. The contour-mode resonators vibrate within the lateral dimension while the electrical field is applied orthogonally through the piezoelectric transducer layer, so a highly c-axis orientated ZnO films are desirable for the development of the contour-mode resonators. To obtain the best quality film, a systematic study on the quality of the ZnO films has been carried out. Two of the sputtering deposition parameters, oxygen concentration and termpaerature, have been varied and documented. The quality of the films are then determined by using x-ray diffraction (XRD). During the experiments, the substrate to target distance, the deposition base pressure (5 mtorr), and the RF power (100W) are kept as constant.

3.2.1 Effects of Oxygen Concentration

Unlike AlN reactive ion sputtering, ZnO is sputtered directly through a 99.99% ZnO sputtering target. In theory, it is possible to sputter ZnO thin films without the need of extra oxygen. However, as the sputtering target is bombarded by the argon plasma ion, some ZnO

molecule will disassociate after leaving the target forming free zinc and oxygen species. The overall film quality is then lowered if the free zinc atom reaches the substrate and incorporates itself within the film. Therefore, the presence of oxygen is needed to compensate for this loss and allowed the zinc atoms to recombine and form ZnO again [41, 42].

This experiment is setup to study the change in ZnO thin film's quality under different argon to oxygen ratio. The oxygen percentage is set to four different ratios: 20%, 30%, 50%, and 70%. The rest of deposition parameters such as power and pressure are kept at the conditions stated above (100 Watt and 5 mtorr). The deposition temperature is set to 300 °C. Figure 3.1 shows the XRD spectra for the ZnO thin films deposited under different oxygen concentrations. The XRD peaks indicates all four films are c-axis orientated. As the oxygen concentration increased from 20% to 50%, the dielectric effect becomes stronger. When the oxygen concentration is increased beyond 50%, it shows degradation in the quality. In the end, 50% argon to oxygen ratio is chosen for the development of piezoelectric resonator.

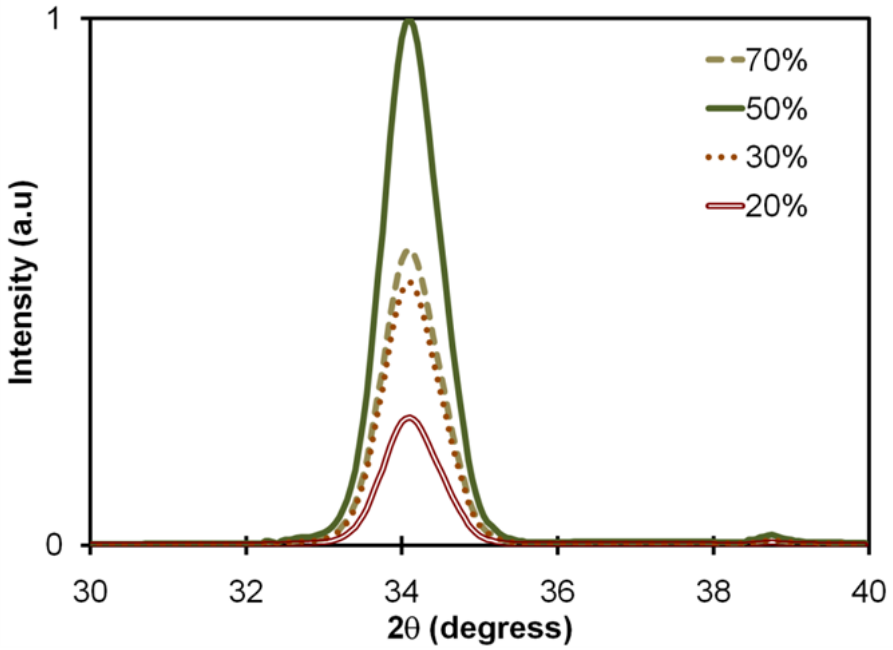

Figure 3.1 – XRD curves for ZnO samples deposited at different oxygen concentrations [40].

3.2.2 Effects of Substrate Temperature

Once the oxygen concentration is determined, we start varied the deposition temperature and examine its impact on the film's quality. Substrate temperature plays an important role in determining the film's quality. The surface temperature of the substrate greatly effects the sputtered particles' energy once it hit the substrate which greatly effects the formation of the thin film. Several depositions ranging from room temperature to 300 °C are carried out, and the results are shown in Figure 3.2. From the XRD spectra, the film deposited at 300 °C exhibits the strongest (002) peak intensity. At higher temperatures, the intensity maintains the same order of magnitude, however, due to the grain increase in grain size, the FWHM, sharpness, decreased gradually.

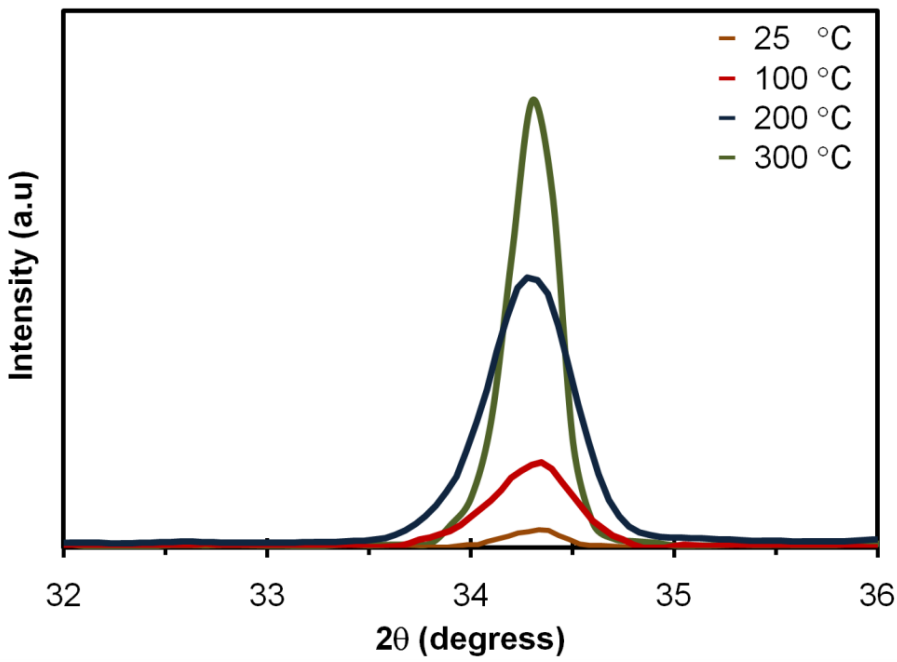

Figure 3.2 – XRD curves for ZnO samples deposited at different substrate temperatures [40].

In summary, the final ZnO thin deposition recipe used throughout this work is: 100 Watt RF, 5 mtorr base pressure, 300 °C substrate temperature, and 50% oxygen to argon ratio.

3.3 Fabrication Process for Thin-film Piezoelectric on Silicon

Figure 3.3 below shows the cross-sectional fabrication process for the TPoS piezoelectric resonators that uses ZnO piezoelectric thin film. This process begins with etching away the buried oxide layer so the resonating body is suspended. The release is done by submerging the wafer with pre-etched through holes under a 49% hydrofluoric acid (HF) for 75 minutes. Since HF attacks ZnO aggressively, the release process has to be done before the deposition of ZnO. The bottom electrode is then deposited and patterned onto the wafer. The material of choice for the bottom electrode is platinum (Pt). Other metals such as molybdenum (Mo), aluminum (Al), and gold (Au) were considered for the bottom electrode, however, these materials proved to be problematic during the subsequent fabrication process. Aluminum and molybdenum are appealing for its mechanical properties. They have low acoustic loss and high acoustic velocity when compared to platinum. Nonetheless, both materials oxidized too easily due to the high temperature and oxygen presence during the sputtering of ZnO, which not only lower its own conductivity, but also reduce the quality of the piezoelectric film. On the other hand, gold has wonderful conductivity and doesn't oxidize under our process condition. However, the presence of the gold film on the wafer prohibits the use of the most optimal temperature for the deposition of ZnO film. At around 300 °C, gold have the tendency to spiking into the ZnO thin film and render the whole process short circuited. After the formation of bottom electrode, ZnO (500 nm in thickness) is then sputtered onto the wafer using the condition stated in previous section, and followed by a deposition and patterning of the top electrode, aluminum. A light density material is chosen here because aluminum has the minimal loading effect. Via holes for access to the bottom electrode underneath the ZnO layer is opened using diluted hydro chloric acid (HCl :

H_2O = 200 : 1). Finally, ZnO and the Si device layers are patterned using DRIE. A layer of gold pad is added here for the convenience of coplanar waveguide (CPW) probing measurement.

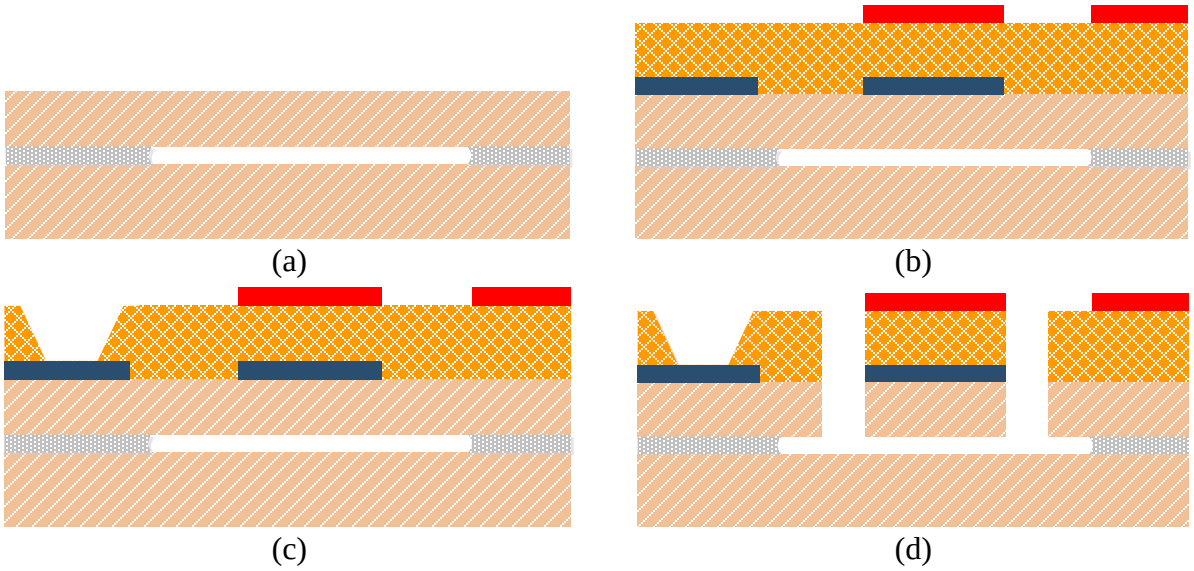

Figure 3.3 – Five-masks post-CMOS compatible fabrication process of thin-film piezoelectric-on-silicon (TPoS) resonator.

Figure 3.4(a) shows a SEM photo of a ZnO-on-SOI resonator using the fabrication process depicted above. Figure 3.4(b) shows a close-up view of the DRIE etched sidewall profile of a ZnO-on-SOI resonator. Ideally, the highest device performance can be achieved when the sidewall for both the piezoelectric layer and the Si device layer are perfectly straight. From the close-up view, it is clearly shown that the in-house ZnO etch recipe produced nearly vertical sidewall. The scalloping profile observed along the sidewall of the Si device layer can be attributed to the characteristics of the DRIE's Bosch process used to etch the silicon. This non-straight profile could potentially affect the performance of the fabricated resonators as demonstrated in [28]. Although achieving perfectly straight side wall is possible with further fine tuning of DRIE recipe, it is not in the scope of this work.

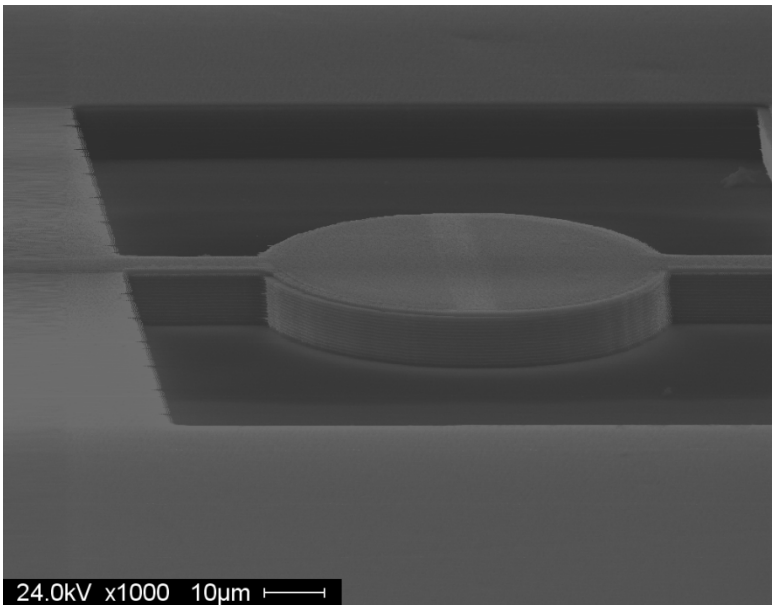

(a)

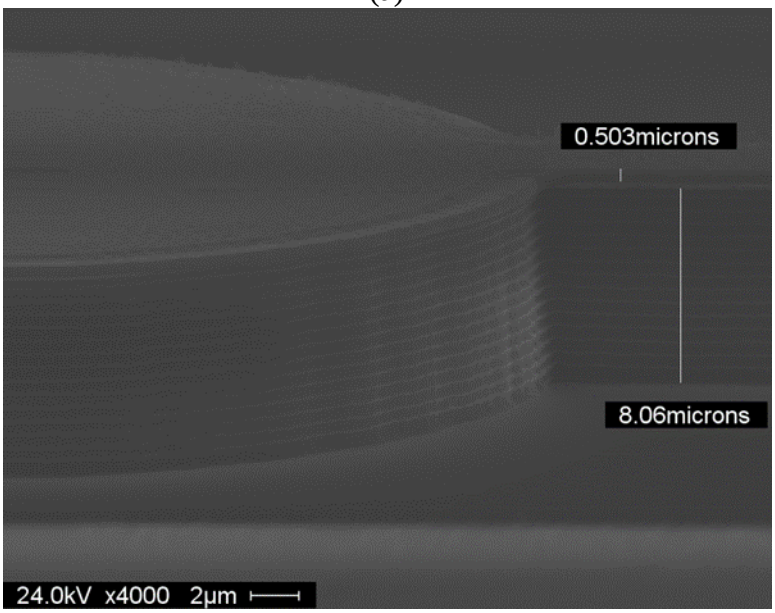

(b)

Figure 3.4 – (a) SEM photo of a TPoS resonator fabricated using the process described above. (b) A close-up view of a TPoS resonator fabricated on an 8 µm device layer SOI substrate with 500 nm thick of ZnO.

3.4 Experimental Results

The fabricated micromechanical resonators are tested by on-wafer probing using a RF probe station under atmospheric pressure and room temperature. The scattering parameters (S-

parameters) of the devices are extracted using an Agilent 8753E vector network analyzer (VNA). A Short-Open-Load-Thru (SOLT) calibration using GGB CS-5 calibration substrate is performed before extracting each device's S-parameter. Figure 3.5 below shows the measurement setup used in extracting the S-parameter data.

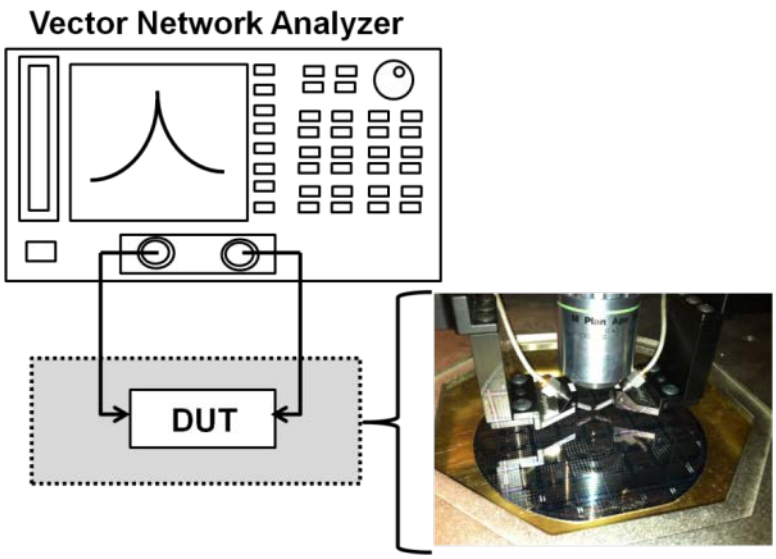

Figure 3.5 – Experimental set up for on-wafer probing of MEMS resonators.

The advantage of TPoS resonators over traditional piezoelectric resonators is the separation of transducing and resonating mechanisms. Traditional piezoelectric resonators rely on the piezoelectric layer to acts as both functions, which means the end results highly depends on the piezoelectric material itself. From chapter 2, it shows the resonant frequency, *Q* factor, and performance are highly regulated by the material properties, therefore, traditional piezoelectric resonator design is locked into the chosen material providing minimal design of freedom. By separating the two, one can use mechanically sound materials such as crystalline silicon and diamond to act as the resonating structure and only use the piezoelectric layer to actuate it. By doing so, the device can achieve higher quality factor. Due the availability of SOI wafers, it has greatly simplified the process of making devices in such configuration. In TPoS

resonators, the acoustic energy is mostly contained within the SOI wafer's low acoustic loss Si device layer, which leads to improved quality factor as compared to a traditional piezoelectric resonator counterpart. In this work, various contour-mode disk resonators are fabricated using SOI wafers with 6 µm and 15 µm thick Si device layer.

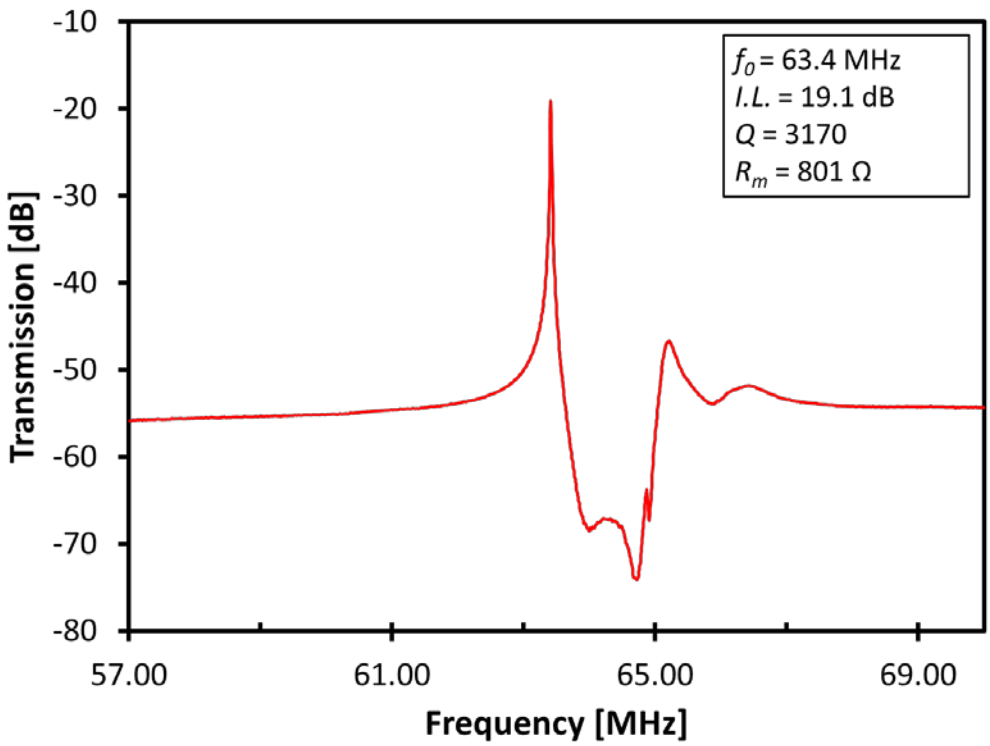

Figure 3.6 – Frequency response of a 60 µm × 150 µm TPoS plate resonator with 15 µm Si device layer excited in its fundamental extensional contour-mode. It is showing a Q of 3170 at 63.4 MHz

Figure 3.6 presents a 60 µm by 150 µm piezoelectric-on-silicon plate resonator operating in its fundamental extensional contour-mode at 63.4 MHz with a measured Q of 3,170. The resonator body is composed of a 15 µm thick silicon device layer and a 500 nm-thick ZnO piezoelectric layer. This device's anchor width is 6 µm. The length of the anchor is quarter wavelength long with respect to its resonant frequency which minimizes its damping loss to the overall structure. Due to the improved quality factor (Q ~ 3,100), the device is able to achieve

motional impedance in the order of hundred-ohms. In order to explore the impact of the silicon device layer thickness, an identical device with 6 µm Si device layer is fabricated and measured as well. As can be seen in, both the motional resistance and quality factor decreased when compared to its 15 µm counterpart. Few interesting conclusions can be drawn here. First, when a TPoS resonator vibrates, it is the actuation layer, ZnO, that excites the Si resonating body. When a thicker, in other words, heavier device layer is used, this mechanical motion is damped due to the fact that the same amount of piezoelectric force now needs to drag along a bigger amount of mass. Therefore, the overall electrical-mechanical coupling coefficient is attenuated, resulting in a weaker electrical signal and higher motional impedance. As verified by the measurement results, the motional resistance increased by 20% when a 15 µm Si layer is used instead of 6 µm.

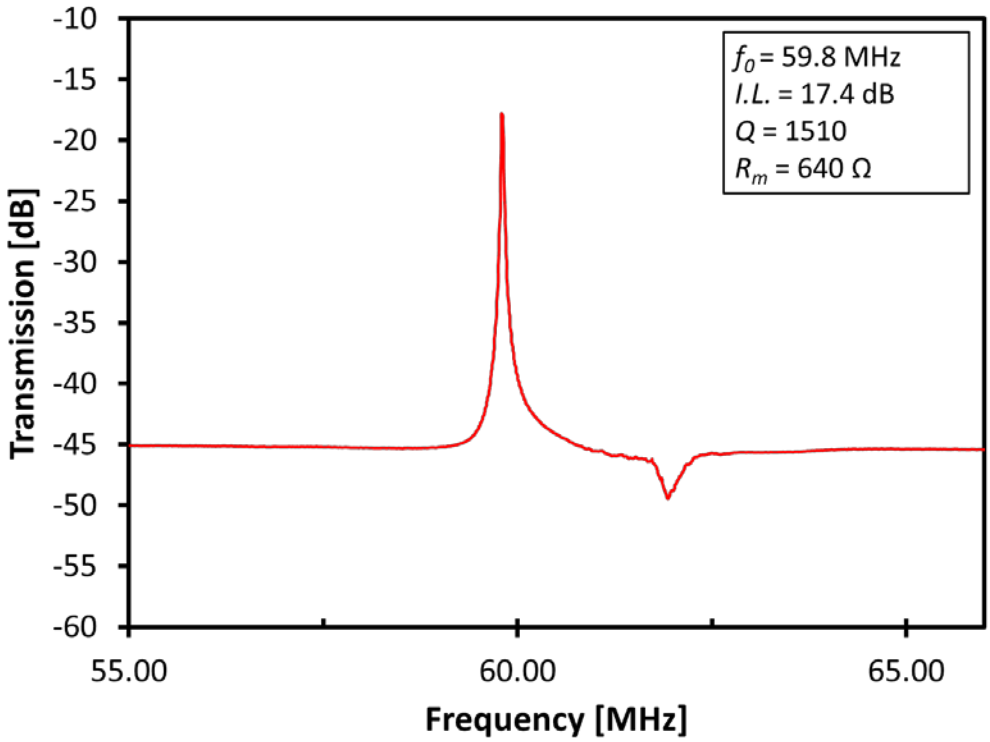

Figure 3.7 – Frequency response of a 60 µm × 150 µm TPoS plate resonator with 6 µm Si device layer excited in its fundamental extensional contour-mode. It is showing a Q of 1510 at 59.8 MHz.

As opposed to the motional resistance, the quality factor increases when thicker Si layer is used. This behavior is caused by mass loading effect as expressed in equation (2.9). In a TPoS configuration, a thick layer of Si device layer means the dominant material is the Si which is a low acoustic loss material. If thinner Si device layer were used, the relative proportion of piezoelectric and metal layers increased, and hence the decrease in overall quality factor.

Another worthy observation here is the shift in resonant frequency. By mathematical formula (Eq. (2.20)), the resonance frequency with such dimension should be 68 MHz. Even though both devices have the same dimension, the resonance frequencies for 6 μm and 15 μm Si layer devices are 59.8 MHz and 63.4 MHz, respectively. This also can be explained by mass loading effect. The equivalent phase velocity of a TPoS resonator with 15 μm Si layer device is closer to a pure Si resonator, and as a result, the resonance frequency is closer to the ideal value.

Therefore, a trade-off must be made between quality factor and motional resistace. Based on the measurement results and the behavior observed, the optimal device layer thickness should reside within 8 μm to 12 μm for 500 nm thick piezoelectric ZnO layer.

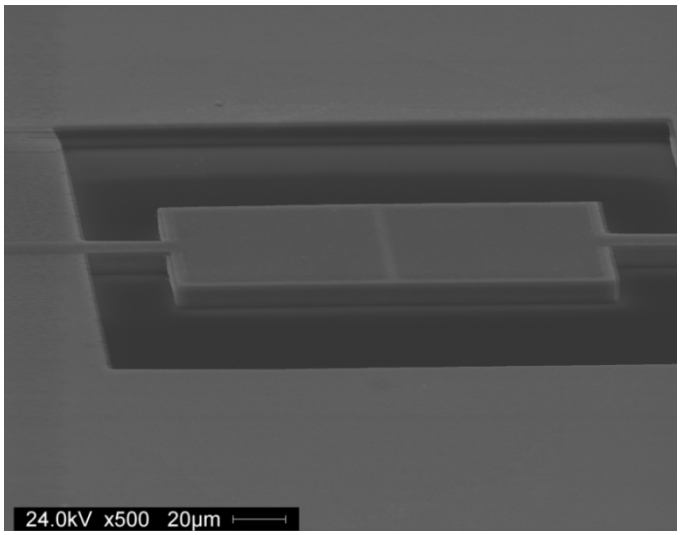

Figure 3.8 – SEM picture of a 60 μm × 150 μm TPoS plate resonator fabricated on SOI wafer with 15 μm-thick device layer. Device shown here is a 2-port configuration with splitted top electrodes.

3.5 Piezoelectric RF MEMS Filter

The goal of this dissertation work is to develop MEMS resonator that can meet today's industry and market demands for complete system-on-a-chip solution. Up to this point, we have solidify the idea of contour-mode piezoelectric MEMS resonators have quality factor and performance as good as BAW and SAW devices, while satisfying the stringent requirements for single-chip multi-frequencies applications. The ultimate goal out of all this is to use the developed resonator and produce RF band bass filter for miniaturization of the transceiver. The MEMS filters need to have characteristics such as high selectivity, low insertion loss, and excellent out-of-band rejection, but it also needs to be compatible with standard CMOS process. Though not the focus of this work, this section attempted in building RF bandpass filter using piezoelectric MEMS resonator, which shows the huge potential of RF MEMS device for future applications in wireless telecommunication system.

3.5.1 MEMS Filter Operating Theory

Depending on the coupling method, usually multiple constituent resonators need to be couple together to form a filter response [39, 43, 44]. For example, in mechanical beam coupling method; it uses a beam, which acts as a spring, to connect two vibrating bodies together, therefore, forming in/out of phase response that constitutes a filter response. See Figure 3.9 below for a detail illustration. There are many ways to couple individual MEMS resonator into a configuration that has a filter characteristic. Some are done mechanically (*e.g.* beam coupling method) [45, 46], and some are implemented through electrical domain (*e.g.* capacitive coupling method) [47]. Since this section is just a demonstration of the possibility of MEMS resonator as a potential RF filter, acoustic coupling method is chosen for simplicity reasons.

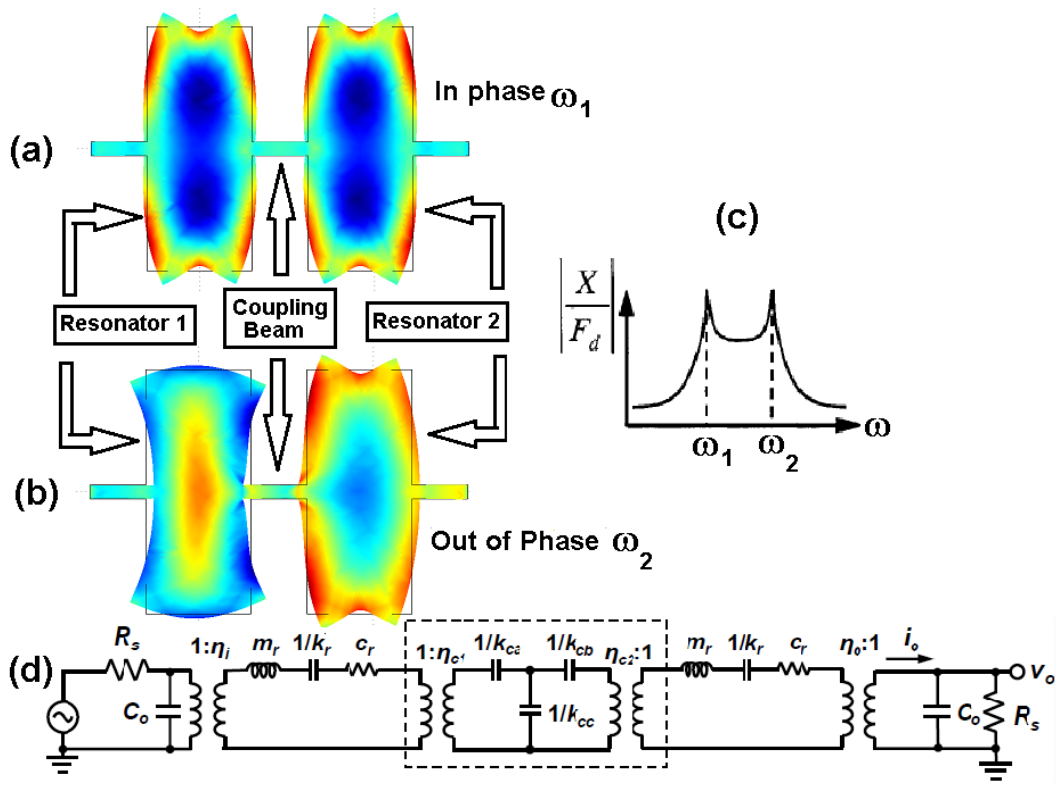

Figure 3.9 – Illustration of the working principle for a mechanically-coupled resonator filter vibrating in (a) in-phase mode; (b) out-of-phase mode; with (c) predicted bandpass frequency characteristic; and (d) electrical equivalent circuit model [40].

Acoustic coupling is one of the easiest filter coupling method [48]. Unlike electrically and mechanically coupled methods, it does not require the use of multiple resonators in order to form a filter response. It uses two closely-spaced orthogonal resonances from a single piezoelectrically-transduced plate resonator. This filter synthesis technique removes the need for additional mechanical coupling elements (*i.e.* beam and capacitance) which improves the design accuracy while demanding minimum fabrication effort.

Figure 3.10 and Figure 3.11 show examples of acoustically coupled monolithic filter. It is shown in both figures that an acoustically-coupled filter is very similar to a plate resonator shown in section 3.4, however, by strategically placing the top electrode, a second resonance mode can exist within close proximity. In the symmetric mode, the entire resonating body are in-

phase (Figure 3.10(a)), whereas in the asymmetric mode the two halves of the body are 180º out of phase (Figure 3.10(b)).

f_o = 67.58 MHz **f_o = 69.46 MHz**

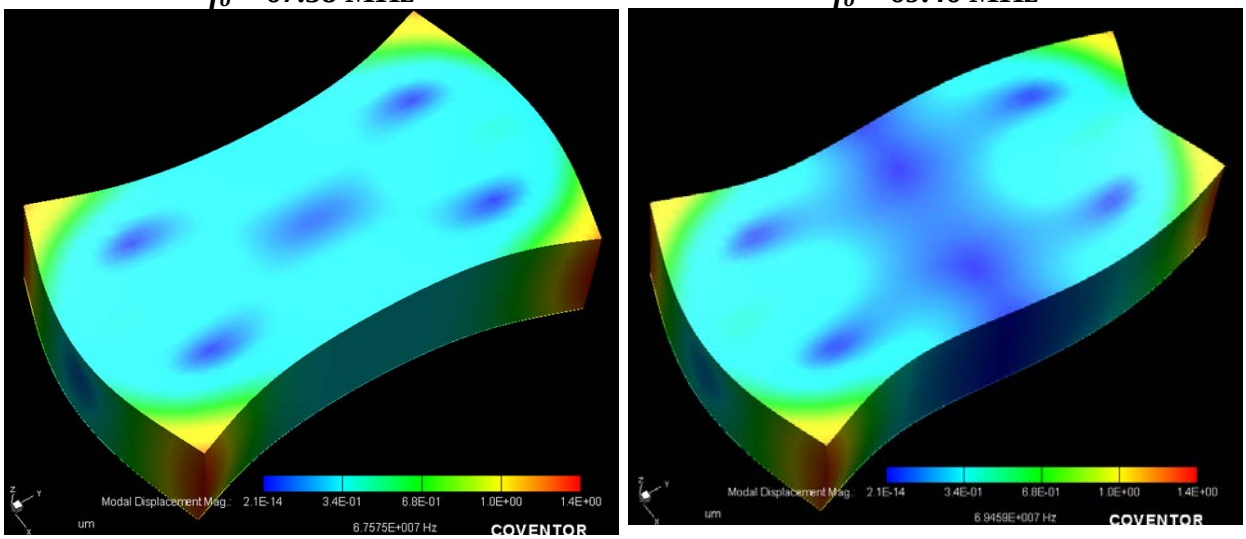

(a) (b)

Figure 3.10 – Simulated dual fundamental length-extensional mode of a 60 µm x 30 µm ZnO plate resonator (a) symmetric resonance-mode and (b) asymmetric resonance-mode.

f_o = 67.87 MHz **f_o = 68.97 MHz**

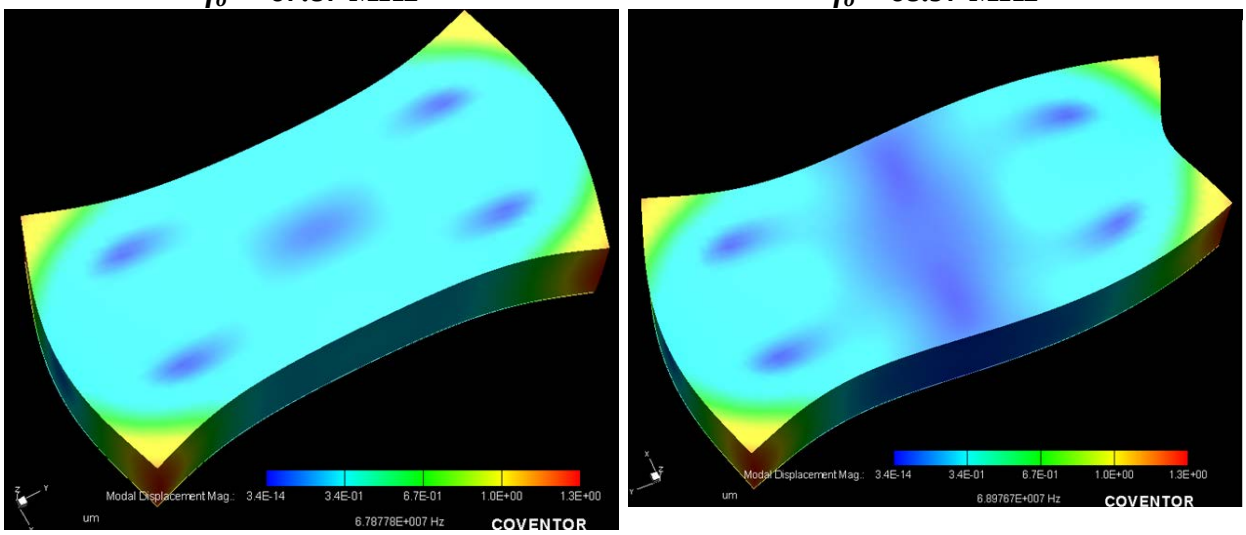

(a) (b)

Figure 3.11 – Simulated dual fundamental length-extensional mode of a 70 µm × 30 µm ZnO plate resonator (a) symmetric resonance-mode; and (b) asymmetric resonance-mode.

As is shown in Figure 3.11, by varying the dimension of the plate, both modes' resonant frequency shifted slightly resulting in smaller bandwidth. Therefore, it can be concluded that the bandwidth of an acoustically-coupled filter can be fine-tuned from the CAD layout design.

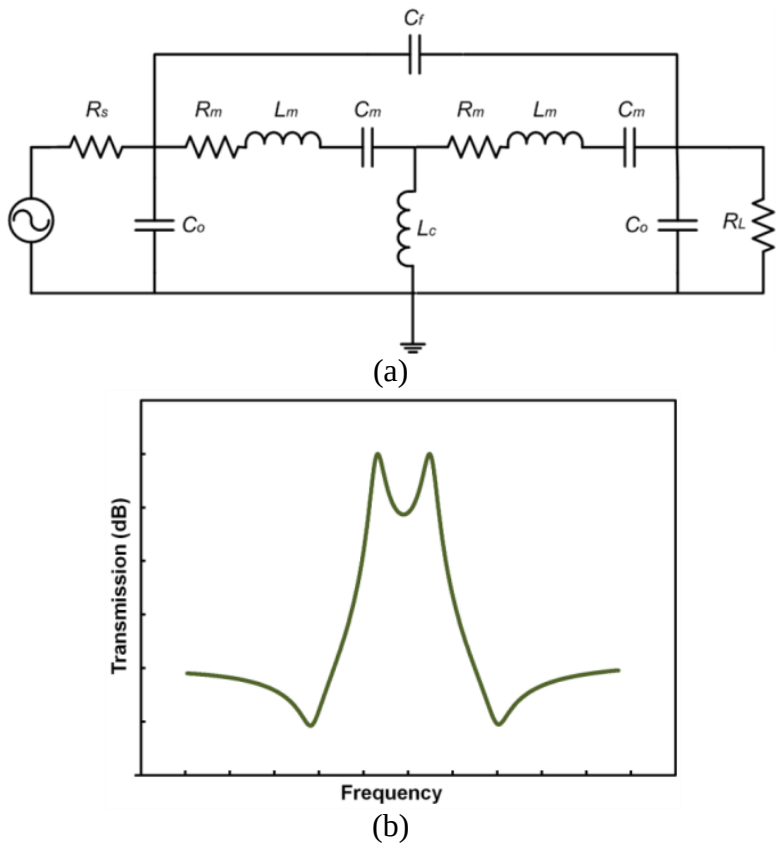

Figure 3.12 – (a) Equivalent electrical circuit model for a 2nd order acoustically-coupled filter; (b) Normalized frequency response for a 2nd order acoustically coupled filter [40].

Unlike mechanical beam coupled filter, the two adjacent mechanical vibration modes in an acoustically coupled filter is coupling through the device itself. The equivalent electrical circuit model for 2nd order acoustically-coupled filter is shown in Figure 3.12. The coupling element in this model is represented by an inductor, L_c.

3.5.2 Experimental Results

Figure 3.13 shows the frequency response of a fabricated thin film piezoelectrically-transduced monolithic filter with center frequency at 115 MHz. The device dimension is 100 µm

by 200 µm. As mentioned previously, if the length that defines the in-phase resonance frequency is set to constant, the bandwidth will shift when the width is varied. Figure 3.14 shows the frequency response for the same monolithic resonator but with the width decreased to 190 µm. Compare the two measured frequency responses, the bandwidth of the synthesized filter changed from 0.83% to 1.2% as a result of a 10 µm variation in the width of the plate resonator.

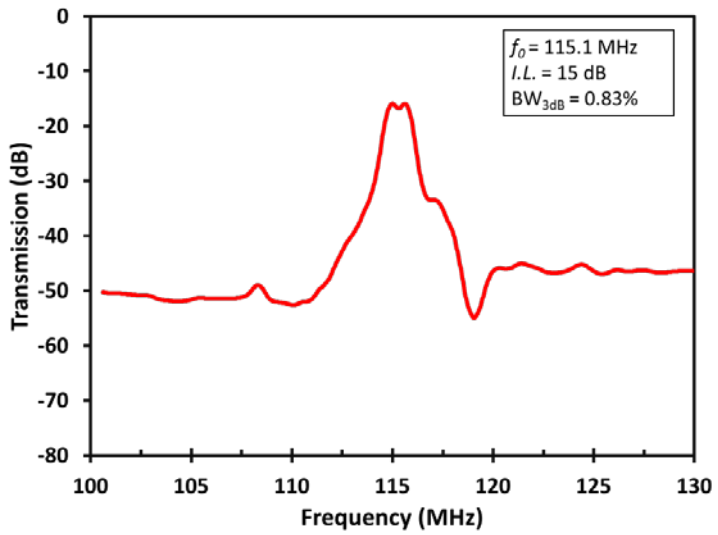

Figure 3.13 – Frequency response for the fabricated 115 MHz monolithic filter with 100 µm x 200 µm lateral dimensions.

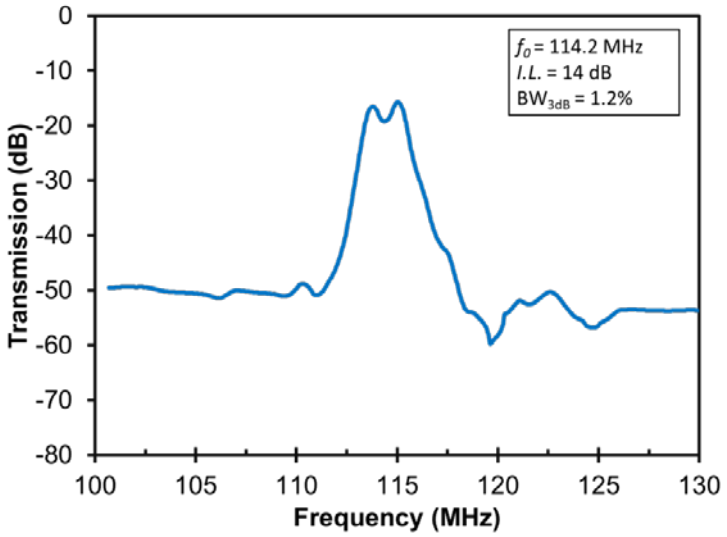

Figure 3.14 – Frequency response for the fabricated 114 MHz monolithic filter with 100 µm x 190 µm lateral dimensions.

It is worth noting that there is no closed-form mathematical solution to predict the secondary dimension's effect on the filter bandwidth. The design process for acoustically-coupled MEMS filter usually involves the use of finite element modal analysis. Softwares such as Comsol and CoventorWare are used in optimizing the dimensions of the micro-structure for obtaining the desired resonance frequency and bandwidth. The drawback for acoustically-couple filter is that the maximum obtainable bandwidth is smaller than mechanically- and electrically-coupled counterparts. Like every engineering solution, there is always trade-off between loss, bandwidth, and rejection. Further design theory and analysis of RF MEMS filter can be found in the work by J. Dewdney [40].

Chapter 4

Development of Electrostatically-Transduced Resonator

From the fabrication point of view, piezoelectrically-transduced resonator has a huge advantage over electrostatically-transduced counterpart. Piezoelectric resonators do not required sub 100 nm parallel plate gap, which is quite complicated to achieve. Nonetheless, this disadvantage does not stop capacitively-transduced resonator from becoming one of the most well developed and studied technologies for the past decades. Unlike piezoelectric type resonators, which can only be built from a very limited selection of piezoelectric materials, capacitive resonators can be made from literally any conductive material with appropriate mechanical properties. Previous research works have demonstrated it can be made from metals such as nickel [49, 50] or non-metals material like crystalline Si and diamond [51, 52]. It is entirely possible to build capacitive resonator from Si alone without using any metals or exotic dielectric material. This advantage alone gives the edge to capacitive resonators being more capable at integrating with CMOS technology than piezoelectric resonators. In addition, capacitively-transduced resonator has a built-in on/off switch that is needed in MEMS enabled transceiver introduced back in section 1.3. This eliminates the need of incorporating additional switches in front the bandpass filter bank, which further reduces the footprint and complexity of the transceiver.

The capacitive resonator's working principle is similar to the piezoelectric counterpart. The goal is to excite the vibration body mass into its resonance mode. However, unlike

piezoelectric materials, which the piezoelectric film can deform upon the presence of electric field, electrostatically-transduced resonator required the use of parallel plate electrostatic force to provide the necessary physical excitation.

As mentioned before, the biggest drawback to capacitive resonators is the complexity of the fabrication process. To build a state of the art capacitive resonating device, the process usually involves relatively more photolithography steps, and more sophisticated equipment such as LPCVD, furnace anneal, and low-stress nitride film [23]. One of the contributions of this work is the successful development of a fabrication process that greatly simplified the process of producing electrostatically-transduced resonators with sub 100 nm parallel plate gap. The newly developed process utilize processing techniques such as atomic layer deposition (ALD) and chemical mechanical polishing (CMP) to reduce the processing steps down to merely two photo mask sets. This chapter presents the fabrication process and experimental results of a capacitive resonator fabricated from the newly developed process.

4.1 Atomic Layer Deposition

Atomic Layer Deposition (ALD) is one of the keys to the enablement of the newly developed and simplified process for the making of capacitive resonators. ALD has many advantages such as uniform coating over a large area, precise control of thickness, and high aspect ratio conformal coverage [53, 54]. ALD is a self-limiting process that gives users precise control over its thickness. At each cycle, gaseous precursor is introduced into the chamber and reacts with the substrate's surface. ALD has excellent conformal coverage due the gaseous nature of the precursor. Precursor atoms are then absorbed to the substrate surface with the excess atoms being purge out [55]. During an ALD deposition process, usually two precursors are sequentially pulsed into the chamber, and the pulses are separated by a purge with inert gas,

so the two precursors never see each other. Without adequate purge time in between, the two gaseous precursors will come in contact with one another and form chemical vapor deposition (CVD) that could contaminate the entire deposition system and the film.

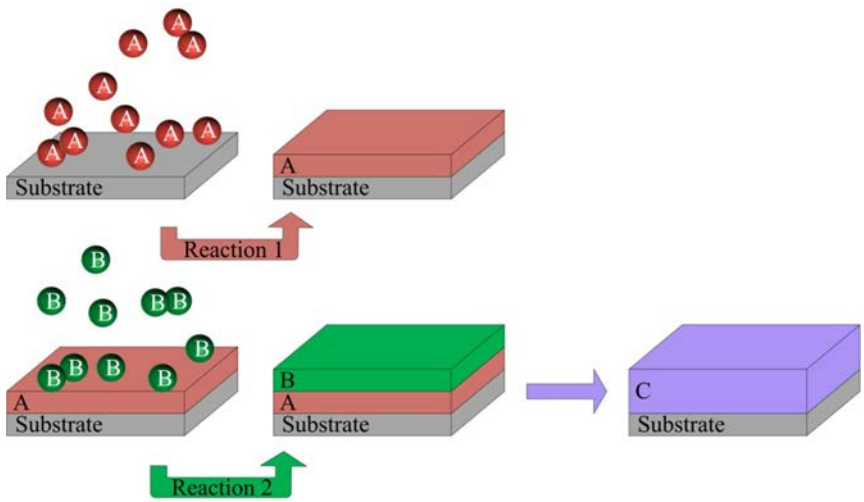

Figure 4.1 – Schematic showing of ALD self-limiting process [55].

The system used for the development of this work is from Cambridge Nanotech Inc. – model Savannah 200. The ALD thin film is incorporated into capacitive resonator as the dielectric gap filler material. Depending on the material used, the dielectric material can either be used as a solid gap material to enhance the capacitance, or as a sacrificial material that can be later removed forming sub 100 nm air gap within the resonator. In this work, two materials were used in the development of capacitive resonators: Hafnium Oxide, HfO_2, and Aluminum Oxide, Al_2O_3.

4.2 Chemical Mechanical Polishing

Another key element of the newly developed fabrication process is chemical mechanical polishing (CMP). CMP is commonly used in the MEMS fabrication to achieve smooth and planar surfaces on wafers or to bulk remove target material [56, 57]. The CMP process consists of three major components: polishing pad, specimen carrier, and abrasive slurry. The wafer is

attached to the carrier and rotates against the polishing pad. The polishing pad helps transferring the slurry's abrasive forces to the substrate removing materials from the surface.

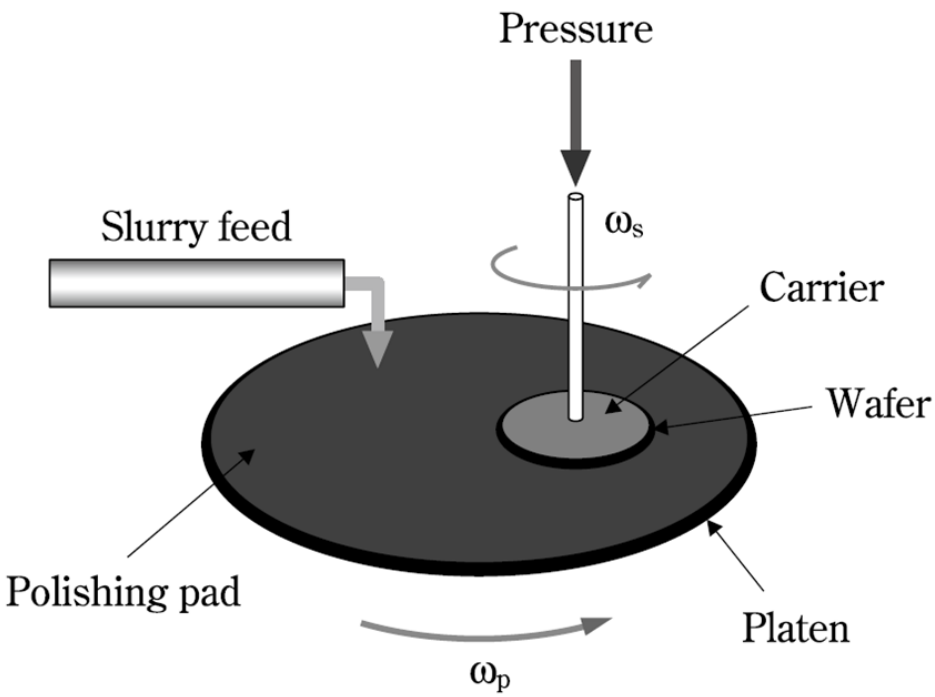

Figure 4.2 – Schematic illustration of CMP process. ω_s and ω_p refer to angular velocity of carrier and platen respectively [58].

In a typical CMP process, the slurry is usually an aqueous solution with certain PH level that accelerates the removal rate of targeted material. For our specific purpose, we tuned the CMP process to have a more uniform removal pattern and rate regardless of the materials being polished. This is achieved by leaning more towards the mechanical aspect of the CMP process by using diamond abrasive slurry. Because diamond is much harder than most materials, the process was able to attain relatively more uniform rate of removal with respect to a variety of materials such as copper and silicon. The system used here is Logitech PM5 lapping/polishing machine, and the carrier fixture is South Bay Technology VersaLap 164DV. The abrasive slurry used is 3 micron diamond suspension.

4.3 Fabrication of Electrostatically-Transduced Resonator

Figure 4.3 below depicts a two masks fabrication process of a capacitive resonator. This greatly simplified fabrication process is achieved through the use of silicon-on-insulator (SOI) wafer. First the wafer is patterned by the DRIE to define the resonator body, and then followed by ALD dielectric layer and metal seed layer depositions. Thick metal side electrodes are plated in selected area defined by the patterned photoresist. The substrate is then planarized from the top uniformly until the Si layer interface is exposed. The device is then released by etching away the photoresist, metal seed layer, dielectric film, and finally the buried oxide. Figure 4.3(e) shows the optical image of a fabricated disk resonator completed with GSG gold probe pads.

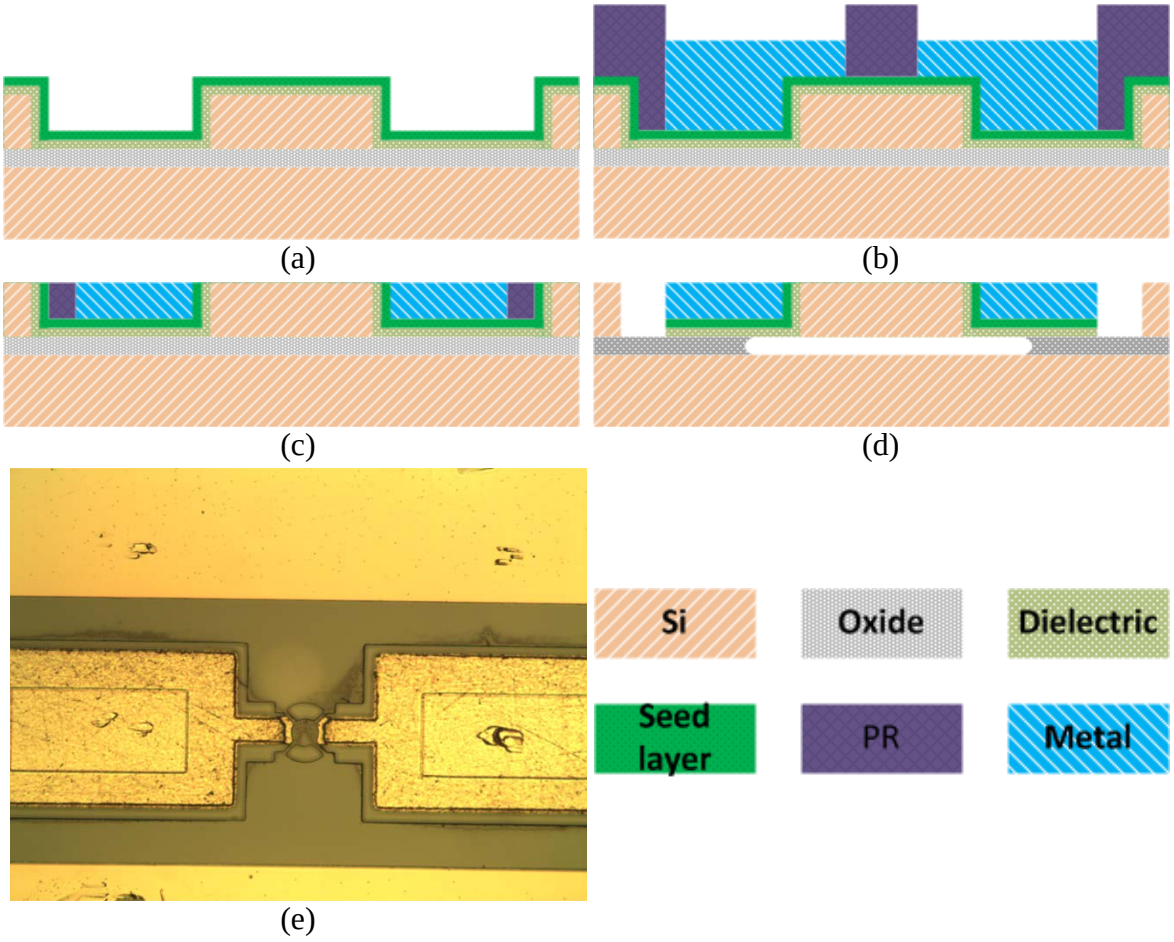

Figure 4.3 – Two steps photolithograph process of capacitive resonator.

Figure 4.4(a) below shows a SEM photo of a capacitively-transduced resonator using the fabrication process depicted above. Figure 4.4(b) shows a close-up view of the parallel plate capacitor gap formed by using ALD dielectric gap spacer.

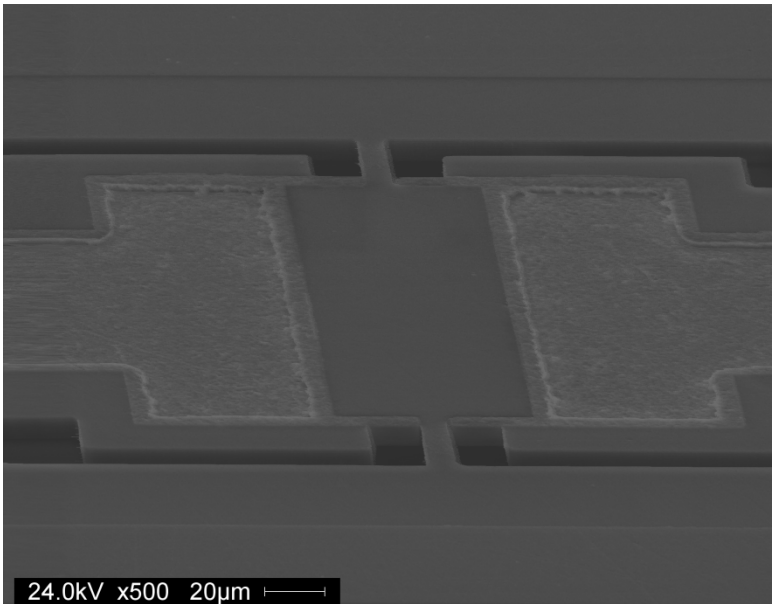

(a)

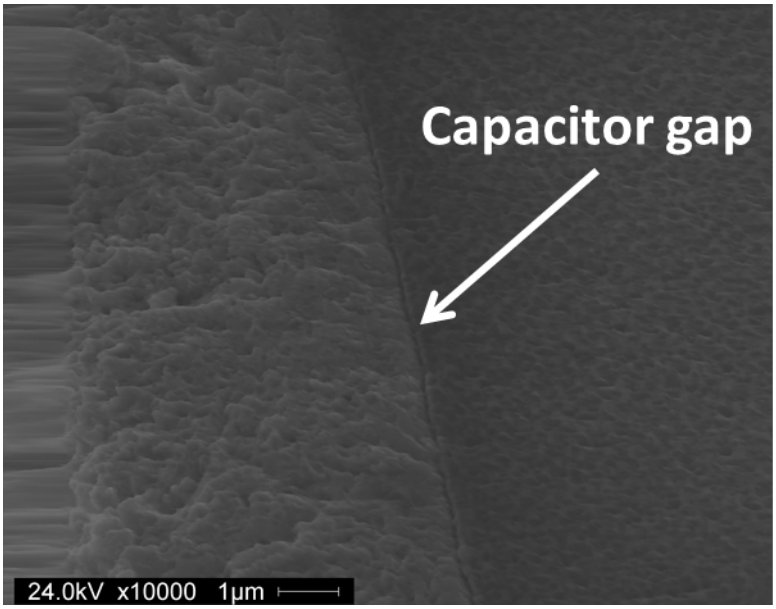

(b)

Figure 4.4 – (a) SEM image of a capactively-transduced resonator. (b) Close-up view at the parallel plate gap.

4.4 Experimental Result

The capacitive micromechanical resonators' S-parameters are extracted using the same calibration and equipment as the piezoelectric resonators. Since the operating principle is electrostatic actuation, DC voltage is supplied through the addition of bias-tees. The test is also done by on-wafer probing using a RF probe station under atmospheric pressure and room temperature.

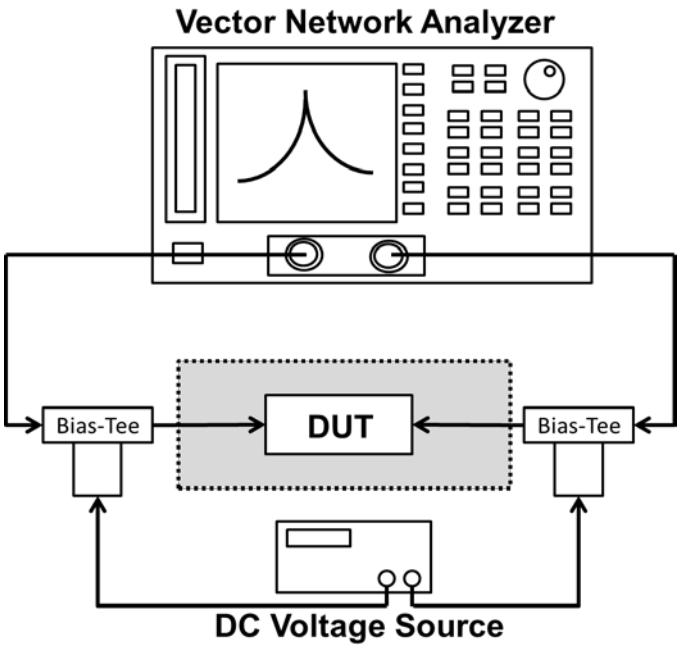

Figure 4.5 – Experimental set up for on-wafer probing of the capacitive micro-resonators.

Figure 4.6 presents the S-parameter of a 24 µm-diameter disk resonator operating in its wine-glass mode. Both on and off states of the resonator response were measured. The on and off states are achieved through switching the DC bias voltage on and off. Due to a mis-calculated mistake (will be discussed later), the response of the resonator is severely attenuated. Moreover, the parasitic feedthrough signal masked and distorted the true response of the resonator. As shown in Figure 4.6, the overall resonating peak wasn't even 3 dB higher than the noise floor, therefore making it hard to extract data such as quality factor.

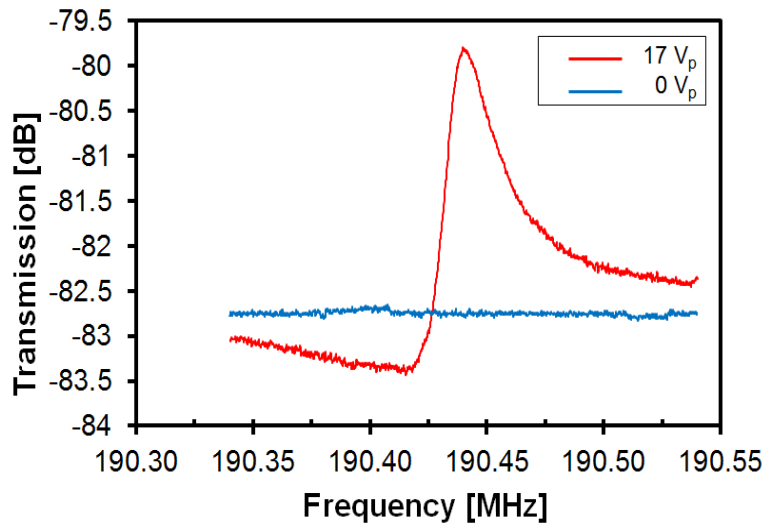

Figure 4.6 – S-parameter for the 24µm disk resonator vibrating in wine-glass mode. (a) As measured S-parameter with device bias on (17 Vp) and off (0 Vp).

Parasitic feedthrough signal is an impediment that is inherent to all types of micron scale resonant devices, resulting in increased challenges to their integration with other electrical circuits, particularly as devices are scaled to operate at higher frequencies for RF applications. Particularly, electrostatically-transduced micromechanical resonators are vulnerable to the parasitic elements due to its parallel plate capacitors that appears across the input and output ports. Figure 4.7(a) below is a greatly simplified equivalent circuit model of a mechanical resonator.

The inductance (L_m), capacitance (C_m), and resistance (R_m) correspond to the inertia, compliance, and damping of the mechanical systems, respectively. There is also a parasitic capacitance, C_f, connecting the input and output of the system, which represent the feedthrough signal path. Such leakage is usually caused by the electrical signal traveling between electrodes directly through the substrate and resonator structure body without going through the electrical-mechanical transformation of the system.

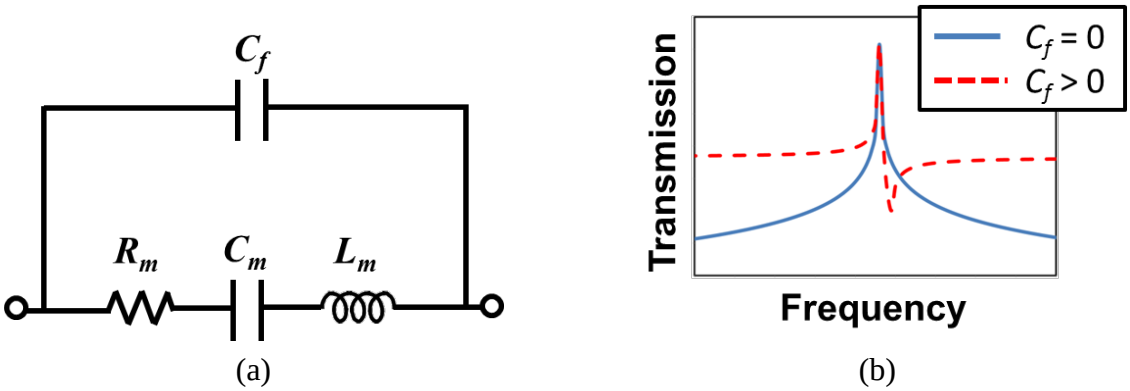

Figure 4.7 – (a) Electrical equivalent circuit of a mechanical resonator. (b) Simulation of C_f's effects on the resonator's transmission response.

High leakage current leads to distorted, masked transmission response, and it diminishes mechanical resonators' supposed sharp roll off rejection band. The influence of the leakage current became even more significant at higher frequencies. Figure 4.7(b) demonstrates the effects of the feedthrougth capacitance on an ideal resonator. The parallel resonance caused by C_f could easily distort the response and generate asymmetricity within the transmission response resulting in great challenges for it to be used as reliable mechanical resonators and filters, let alone interfacing with other transistor circuits.

In order to better understand the device behavior, one technique is used here to post process the data to eliminate the effects of the leakage signal contributed by the parasitic capacitance. As depicted in following Figure 4.8, a capacitive resonator's electrical response can be attributed to two parallel circuits: the *LCR* resonator body, and the leakage feedthrough, C_f. When the device is turned on, the measured response is contributed both by the C_f and the *LCR* circuits. When the device is turned off, the *LCR* components became inactive, while the measured response is solely contributed by the feedthrough circuit. By theory, performing vector subtraction between the on and off transmission parameters, the feedthrough portion is canceled out yielding the theoretical *LCR* response of the resonator.

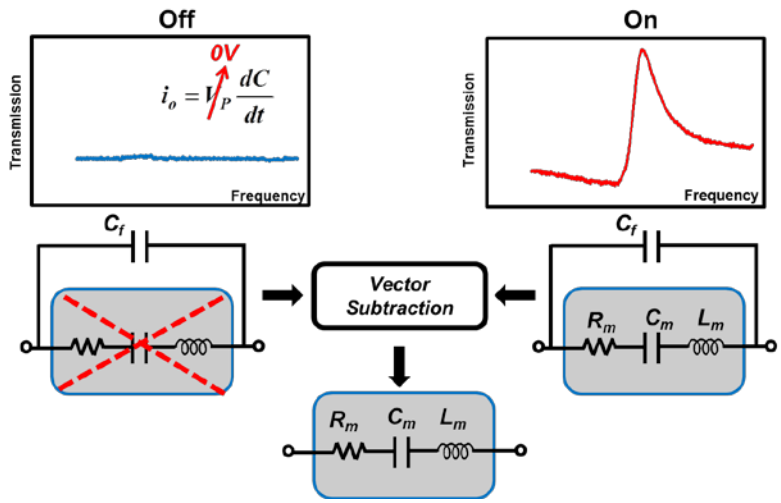

Figure 4.8 – Transmission response vector subtraction.

Figure 4.9 below shows the ideal transmission response of the aforementioned resonator. It is clearly shown that the superiority in Si mechanical properties over piezoelectric material resulted in quality factor above 10,000. However, due to the high insertion loss, the motional impedance is on the order of mega-ohms, which renders it unfeasible to be integrated with traditional IC circuitry.

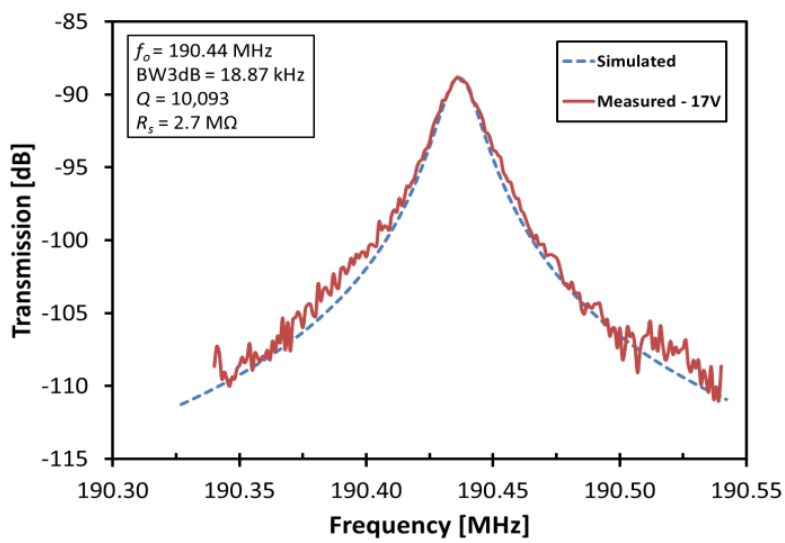

Figure 4.9 – S-parameter for the 24µm disk resonator vibrating in wine-glass mode. (a) As measured S-parameter with device bias on (17 Vp) and off (0 Vp).

The motional resistance, R_s, of a capacitivley-transduced resonator is governed by the following equation [59]:

$$R_s = \frac{k_r}{\omega_0 Q V_p^2} \cdot \left(\frac{\partial C}{\partial x}\right)^{-2} \cong \frac{k_r}{\omega_0 Q V_p^2} \cdot \frac{d_0^4}{\varepsilon_r^2 \varepsilon_0^2 A^2} \tag{4.1}$$

Therefore, varying the bias voltage (V_p) will change the resonator's electrical response. Transmission S-parameter with respect to voltage is plotted in Figure 4.10 below. The motional impedance is inverse proportional to the second power of the bias voltage, hence by increasing the DC bias voltage, V_p, it will effectively reduce the total motional impedance. When the bias voltage is increased from 10 V to 17 V, the motional impedance shows a drop from 7.8 MΩ to 2.7 MΩ.

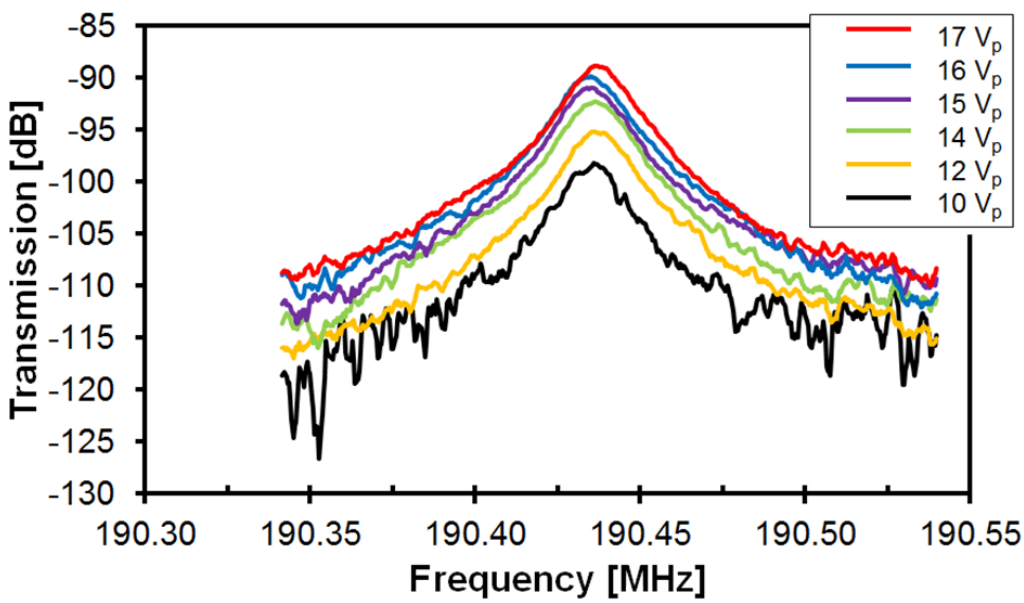

Figure 4.10 – Resonating transmission response of the disk resonator under various DC bias conditions.

4.5 Formation of Parallel Plate Capacitor Gap

The high insertion loss is caused by a mistake during the fabrication process. The plating seed layer (300 nm) and ALD dielectric layer (80nm) was much thicker than necessary. The

combined layer thickness caused a major flaw during the final device release step. As Figure 4.11 depicts below, during wet chemical release of nano-gap devices, it often relies on the surface tension of the wet chemical to prevent etching of the junction gap. However, during the seed layer removal, 300nm was wide enough to diminish the effects of surface tension which allowed the chemical to easily etch deep into the seed layer at the junction. This results in a big opening for the subsequent HF oxide release which now has a big contact surface with the dielectric material. All in all, this resulted in a wide air gap with inconsistent junction gap as opposed to the planned 100 nm solid gap (Figure 4.11(b)). As suggested in equation (4.1), the motional impedance is direct proportional to the gap distance, d_0, to the fourth power, therefore, a small variation in the gap could have enormous effect on the overall impedance of the resonator. Fortunately, this mistake was a not a result in the device design rather a miscalculated fabrication run, which can be easily corrected.

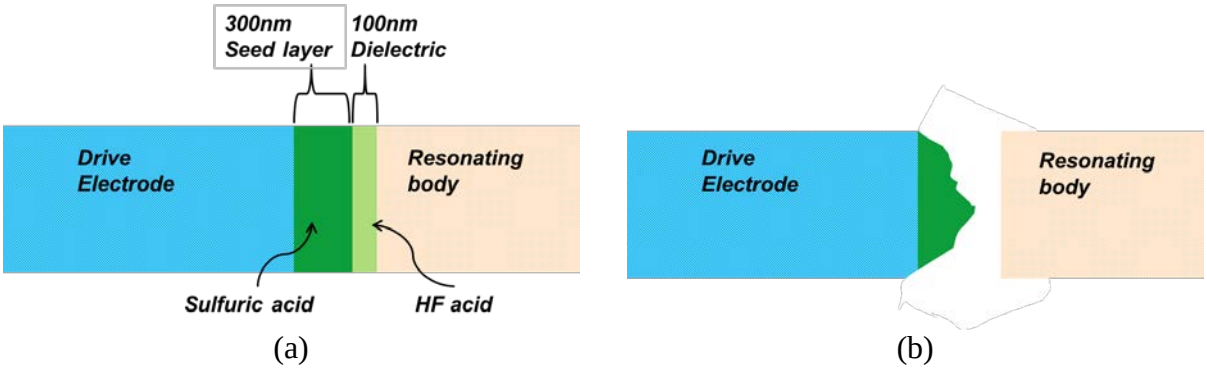

Figure 4.11 – (a) Junction structure before the device release. (b) Wide opening caused the etchant to seek through the junction resulting in inconsistent junction gap.

Chapter 5

Micromechanical Resonators Applications Using SOI Wafer

Chapter 5 here presents applications and ideas that are made possible due to the use of SOI wafer. SOI technology is one of several manufacturing strategies employed in the industry to allow the continued miniaturization of microelectronic devices. In conventional integrated circuit design, SOI wafer provides benefits such as lowered parasitic capacitance and improved electrical isolation. However, the unique layered structure of SOI wafer provides MEMS technology another degree of freedom in designing devices. Clearly, the works shown in previous sections have demonstrated the benefit of SOI technology in simplifying the fabrication process of MEMS resonator. In this chapter, a unique yet simple way of tuning the frequency response of a MEMS resonator will be demonstrated. Thanks to the extra Si layers provided by SOI wafer, by strategically selecting the resistivity of the device and handle layer, a frequency tuning configuration can be easily surmounted. Needless to say, the effectiveness of SOI wafer in reducing the parasitic feedthrough plaguing the performance of micromechanical resonators will also be explored.

5.1 Single-Mask Nano-Gap Electrostatically-Transduced MEMS Resonator

In Chapter 4, a two-steps fabrication process for making capacitive resonator is presented. This section introduces yet another technique that is even more simplified. It is possible to fabricate a capacitive resonator with nano-meter gap by only one single photolithography mask. From previous sections of this work, fabrication process introduced for piezoelectric and

capacitive resonators are CMOS compatible. However, due to the nature of the materials and chemicals used in the fabrication, the processes are more likely to be post-CMOS compatible. The technique documented here addresses the problem, and it has huge potential to be readily deployed in today's CMOS foundry process. The process only requires the use of one single layer of photolithography mask, and the capacitive resonator is made entirely out-of silicon. No direct-write methods such as e-beam lithography are used, which makes this process applicable in mass production environment as well. Figure 5.1 below depicts the single-mask process flow.

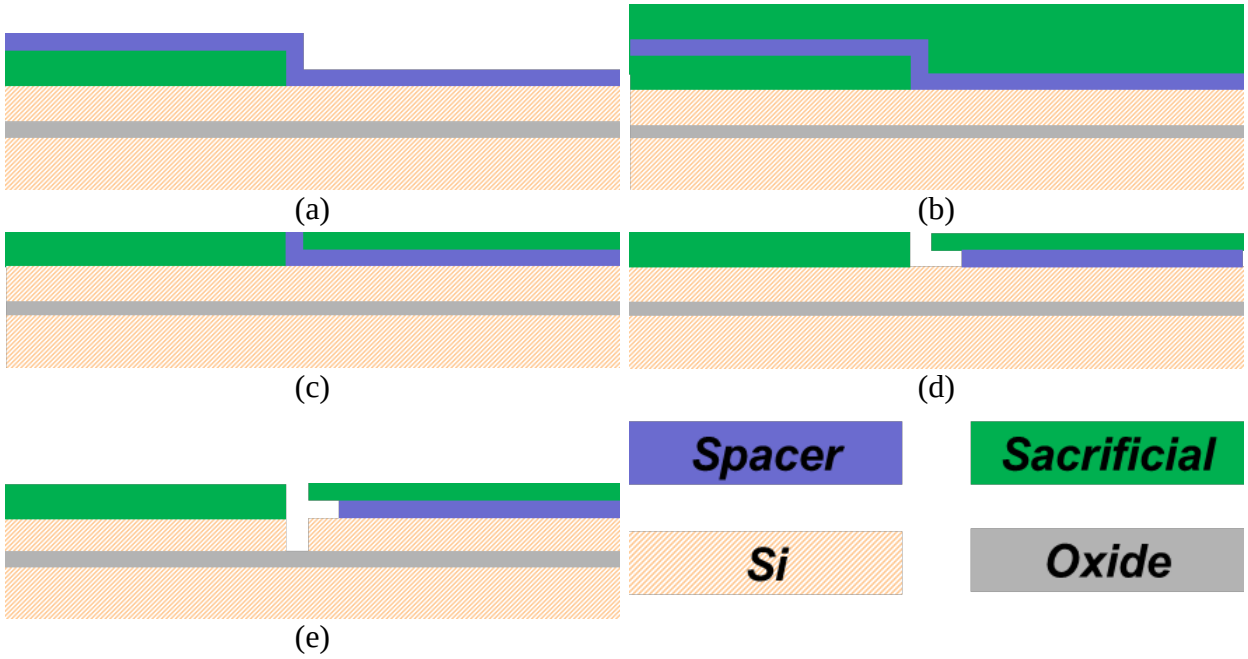

Figure 5.1 – Single-mask fabrication for electrostatically-transduced resonator.

The process begins with a patterned layer of sacrificial material. This material can either be silicon dioxide or photoresist such as AZ4620. A thin layer of gap spacer material is then deposited over the sacrificial layer. It is optimal to have the gap spacer material to be something that can be easily etched away in the subsequent step. In this work, ZnO is chosen to be the gap spacer material as it can easily be etched away by diluted hydrochloric acid which does not attack any other layers. Another layer of sacrificial material is then spun/deposited over the

wafer. CMP planarization or etch back technique is used to expose the vertical spacer gap opening. After, etching away the gap spacer material, the sacrificial layer becomes the mask layer used for DRIE Si etching. SEM pictures (Figure 5.2) shown below is the nano-gap hard mask with 280 nm openings produced using the single-mask process. The opening width can be further reduced by using a thinner gap spacer layer.

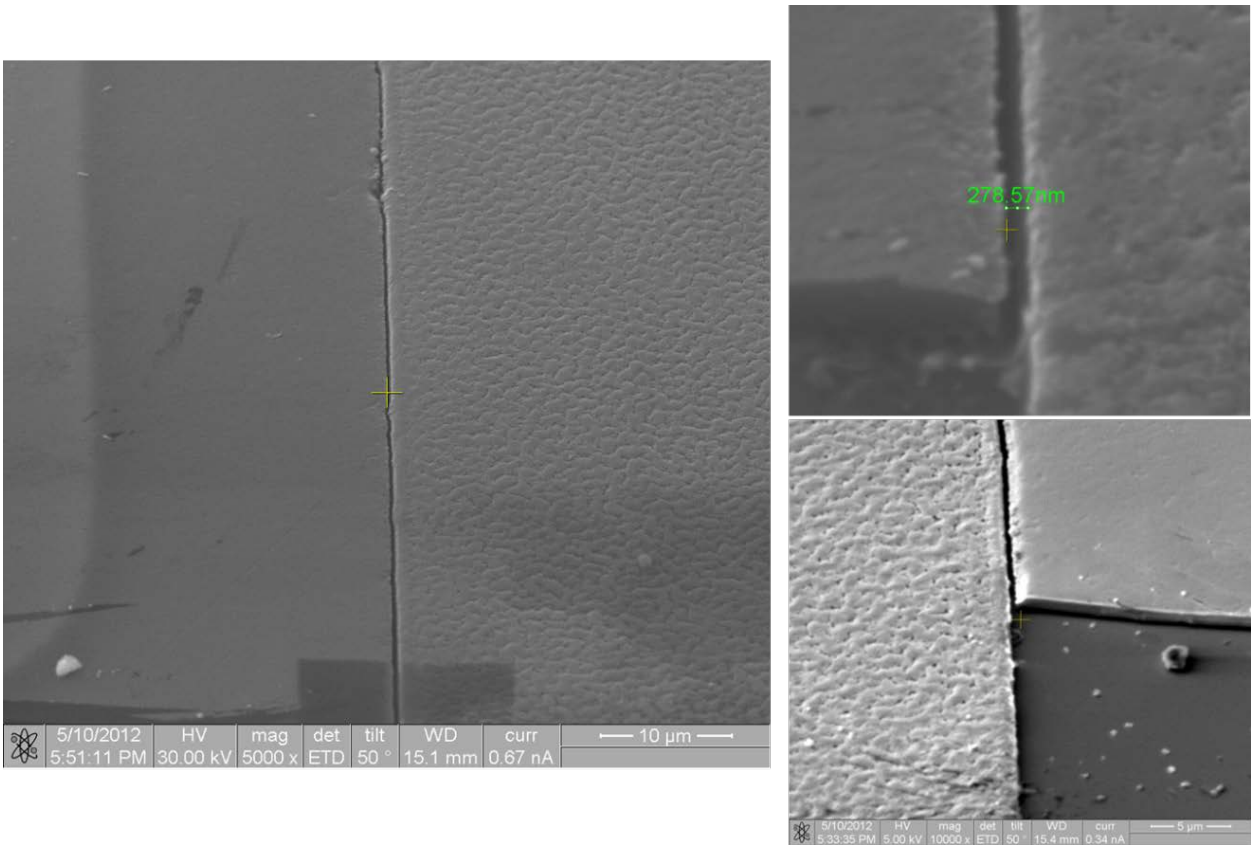

Figure 5.2 – 280 nm gap generated by using aforementioned single-mask nano-gap process.

After creating nano-gap mask layer, the sample undergoes a specially tuned DRIE Si etching recipe created by Plasma-Therm to create the crucial nano-meter gap for capacitive resonator. This recipe is specifically made for etching high aspect ratio Si with nano-meter opening. As shown in Figure 5.3, the DRIE etch recipe is more than capable of producing high aspect ratio Si etch with straight sidewall. The specially tuned etching recipe has no problem

processing gap size as small as 100 nm either. Conventional DRIE Si etch recipe tends to shown taper effect towards the bottom of the etched trench [60, 61]. The straight-ness in the sidewall is critical to the performance of the capacitive resonator. Varying gap distance between the electrode and vibrating body can significantly reduce the total effective actuation area and electro-mechanical coupling factor of an electrostatically-transduced resonator.

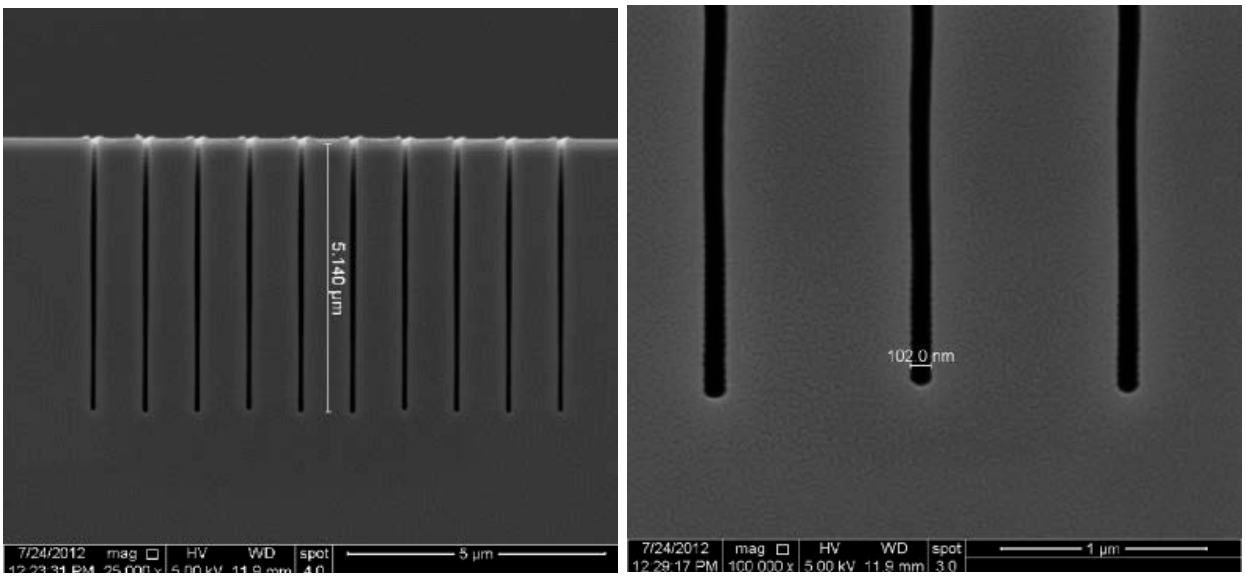

(a) (b)

Figure 5.3 – (a) Plasma-Therm high aspect ratio (50:1) DRIE Si etch with 100 nm openings. (b) Close-up view of the etched trench with sidewall roughness of 7 nm.

Unfortunately, there are no S-parameter measurement results for the single-mask nano-gap capacitive resonator. Though samples completed with nano-gap mask layer have been sent to Plasma-Therm for Si etching, it has yet to be completed as of the writing of this work.

5.2 RF MEMS Resonator and Filter Frequency Tuning

Frequency tuning is another area that has garnered much attention in the past years. Several methods have been proposed over the years. They can be mostly categorized into active- and passive-tuning. Active tuning techniques such as electrostatic and electrothermal are designed to alter the material mechanical properties (*e.g.*, spring constant) [62, 63]. To the

contrary, passive tuning involves changing the resonator's dimension or equivalent mass by using post-deposition and ion milling techniques [64, 65]. It is fairly simple to achieve electrostatic frequency tuning configuration with resonators fabricated on SOI wafer. As shown in section 3.3, the process used to fabricate the piezoelectric on substrate resonators implemented in SOI substrates leave a capacitive gap between the structure and the handle wafer (see illustration in Figure 5.4 below).

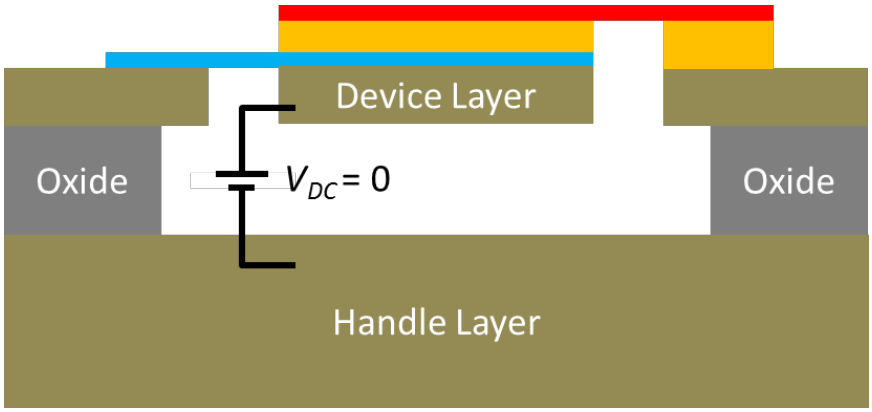

(a)

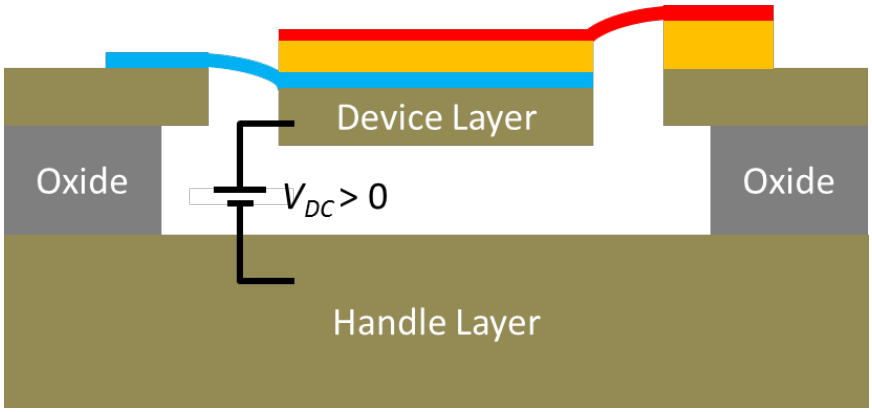

(b)

Figure 5.4 – DC bias electrical connection of resonator frequency tuning off (a) and on (b).

If the handle and the device layer are selected to be low resistivity (*e.g.*, 0.01 Ω•cm) and given that the device layer is in contact with the bottom electrode, the electrical potential of this layer is connected to ground. Applying a DC voltage to the handle layer, an electrostatic force

proportional to the device bending of the resonant structure is generated. This force [66] can be represented as an electrical stiffness (k_e) that is subtracted from the mechanical spring constant of the resonator (k_m) changing its resonance frequency to:

$$f_0' = \sqrt{\frac{k_{re}}{m_{re}}} = \sqrt{\frac{k_m - k_e}{m_{re}}} = f_o \left[1 - \frac{k_e}{k_m}\right]^{1/2} \tag{5.1}$$

where m_{re} is the effective mass of the disk; k_{re} is the effective stiffness at that same location with the dc voltage applied; k_m is the purely mechanical stiffness (*i.e.*, with no voltages applied) of the disk. Form the electro-mechanical analogy presented in section 2.6 and the theory of parallel plate capacitors, the electrical stiffness of the resonator can be expressed as:

$$k_e = V_{DC}^2 \frac{C}{d^2} = V_{DC}^2 \frac{\varepsilon_0 A}{d^3} \tag{5.2}$$

where ε_o is the permittivity of the free space, A is the area of the resonator tangential to the device vibration, and d is the gap distance between the device layer and the handle substrate. The relative change in the resonance frequency can be expressed by:

$$\frac{\Delta f}{f_0} = -\frac{1}{2} V_{DC}^2 \frac{\varepsilon_0 A}{k_m d^3} \tag{5.3}$$

It is worth to mention there is electrostatic force threshold in which this mechanicals system goes unstable, causing the resonator to suddenly snap down onto the handle substrate. This is known as the pull-down voltage, V_P, which is represented as [67]:

$$V_p = \left[\frac{8 k_s d^3}{27 \varepsilon_0 A}\right]^{1/2} \tag{5.4}$$

where k_s does not represent the spring constant of the resonator itself, it represents the combine stiffness of the resonator tethers.

It can be seen from equation (5.3) and (5.4) that both frequency tuning and the allowed maximum voltage heavily depend on the gap distance between the bottom of the resonator and

the handle substrate. It is critical to find the right balance between the pull-in voltage and the frequency tuning percentage. If there is too much of gap spacing, the electrical stiffness induced could be insignificant and cause no shift in frequency. On other hand, if there is not enough gap distance, the mechanical structure could enter premature failure before any substantial change in frequency occurs.

5.2.1 Experimental Result

A 30-µm radius ZnO-on-silicon resonator, with 20-µm device layer and 2-µm gap height between the device and the handle substrate is electrically connected as shown in Figure 5.4. Unfortunately, there is no sign of change in frequency response. It is believed that the gap distance, 2 µm, is too big to produce any sizeable electrical stiffness onto the structure. Obliviously, fabricating resonator using SOI wafer with 1 µm buried oxide layer is the next logical step. However, due to the lack of a properly functioned critical point CO_2 dryer at USF facility, device releasing with only 1 µm or less buried oxide layer is not possible. For small release gap, the surface tension of the water will cause stiction to occur, which will break the device entirely when drying the sample.

An alternative electrothermal frequency tuning method is then pursued. The resonant frequency of a resonator is a parameter that is governed by its Young's modulus, the material density and geometry. The temperature coefficient of the resonance frequency (TCF) for mechanical resonator is mainly governed by the temperature dependence of the aforementioned parameters [51, 68, 69]. The temperature coefficient of frequency is generally expressed in ppm per degree Celsius and is given by:

$$TCF = \frac{1}{f_0}\frac{\partial f}{\partial T} = -\frac{1}{a}\frac{\partial a}{\partial T} + \frac{1}{2}\frac{1}{E_p}\frac{\partial E_p}{\partial T} - \frac{1}{2}\frac{1}{\rho}\frac{\partial \rho}{\partial T} \tag{5.5}$$

where f_o is the resonance at the normal temperature operation point (*i.e.*, room temperature), a is the fundamental geometrical parameter that sets the resonator center frequency and T represent the temperature of operation. This equation is very general and does not take into account the particular mode of vibration of the structure. The third term in equation (5.5) can be eliminated due to its low impact on the overall coefficient. The TCF is then expressed in a simplified form as follows:

$$TCF = -\alpha_p + \frac{1}{2} TC_{E_p} \tag{5.6}$$

where α_p is the thermal expansion coefficient of the vibrating body (piezo, Si, *etc.*), and TC_{Ep} is the temperature coefficient of the young's modulus of the piezo layer or the device layer depending on the resonator design. The metal electrodes also contribute to the overall value of the TCF, however, they were not taken in account in order to simply model. See Table 5.1 below for the typical coefficient number for Si and ZnO.

Table 5.1 – Thermal expansion coefficient for silicon and ZnO (adapted from [59])

Material	α	TC
Silicon	-2.6ppm/ºC	-40ppm/ºC
Zinc Oxide	(-4.4) – (-5.6) ppm/ºC	-50 ppm/°C

To generate electrothermal heating within the mechanical, the device's device layer and handle layer is intentionally shorted electrically while keeping the DC bias connection the same. When bias voltage is applied, a current is drawn which in turns heats up the mechanical structure. Results from the shift in the resonance frequency versus the applied voltage are shown below. The frequency response of the resonator for three different tuning potentials is shown in Figure 5.5.

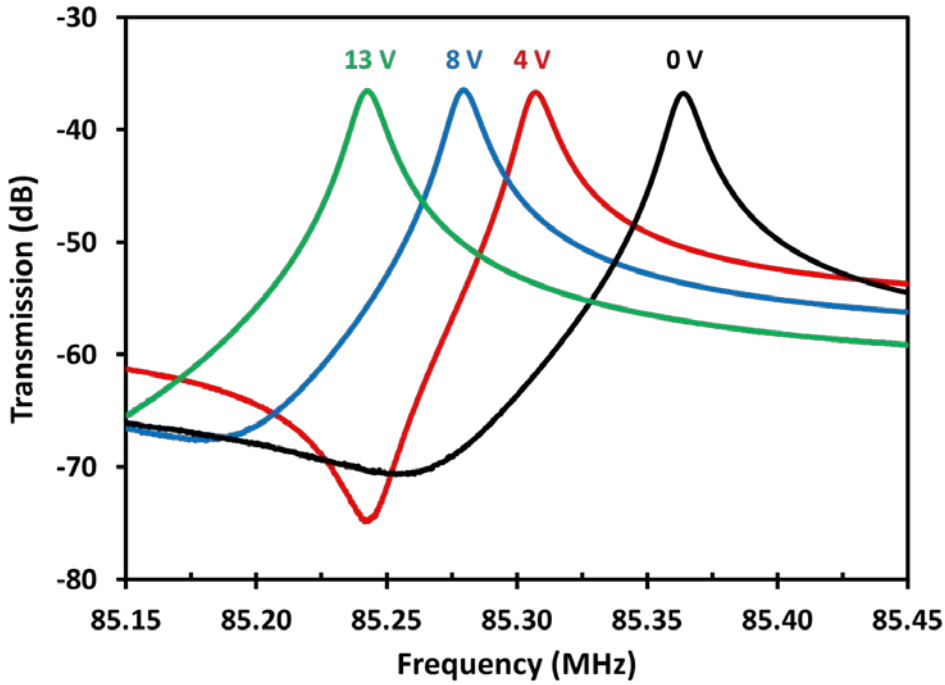

Figure 5.5 – Frequency response of the resonator for three different tuning potentials.

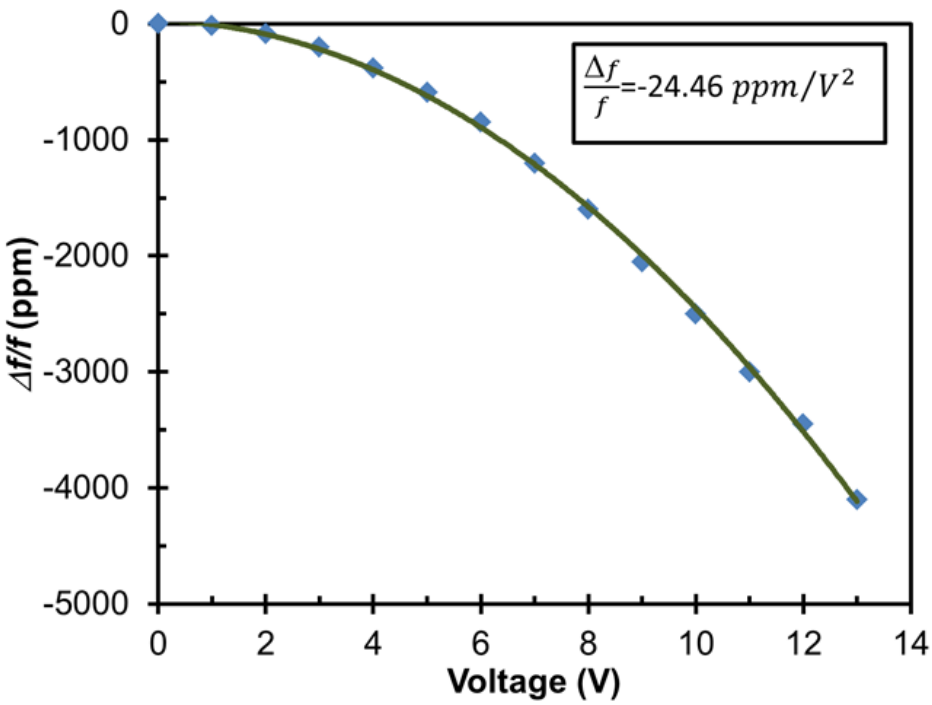

Figure 5.6 – Resonator frequency tuning characteristics. The device achieves up to 4000 ppm of tuning for a voltage of 13 V.

As expected, the change in TCF caused the resonance frequency to shift, and the heat tuning mechanism is reversible. At 13 V, the current draw is nearly 250 mA, which isn't ideal for modern day's mobile wireless communication devices due to the high power consumption. It is worth mentioning that due to the imperfect post-process electrical shorting, the total current draw from the source goes through the entire wafer instead of just one single device. The current draw can be greatly reduced provided that proper shortening method is integrated into future fabrication process. Nonetheless, this proves MEMS resonators have the potential to be incorporated into re-configurable RF front end applications [70]. Overall, the MEMS resonator is able to achieve up to 4000 ppm in frequency tuning at 13 V (Figure 5.6).

5.3 Dual-Transduced Hybrid MEMS Resonator

Two of the most widely-studied on-chip micro resonator technologies leverage either piezoelectric or electrostatic transduction mechanisms. Electrostatically-transduced resonators exhibit better temperature coefficient, on/off self-switching capability, and generally much higher Q at higher frequencies. It has been demonstrated at operating frequency up to 6.2 GHz while still exhibiting Q higher than 4000 [21]. Mixers, filters, and oscillators using capacitive resonator as building block have all been proven to work [10]. However, its extremely high motional impedance and complicated fabrication process hinder itself from being properly implemented into current wireless communication infrastructure. On the other hand, contour-mode MEMS resonator based on piezoelectric material have been demonstrated with 50Ω matched motional impedance, and it's relatively easy to fabricate. Filters using piezoelectric material have shown insertion loss (I.L.) as low as 3dB [32]. However, it lacks any of the aforementioned advantages of its electrostatic-based counterpart.

Even after all these advancements in mechanical resonators, none of the technologies can truly claim being the definitive solution for the much needed single-chip multi frequency RF front-end applications. Coincidently, it just so happens that the two transduction mechanisms complement each other. Table 5.2 below summarizes the results of the two major types of resonators.

Table 5.2 – Summarized characteristics of electrostatically- and piezoelectrically- transduced MEMS resonators.

	Capacitive	**Piezoelectric**
Quality factor	High	Moderate
Fabrication	Complicate	Relatively easy
Motional impedance	High	Low
Reconfigurability	DC bias On/Off	None
Material availability	Most of the conductive materials	Only mainstream piezo materials

A hybrid resonator, combining the low loss acoustic characteristic of an electrostatic micro resonator with piezoelectric material's high electro-mechanical coupling values, could have the potential to solve all the problems MEMS resonators are currently facing. The primary goal of this section will be focusing on producing a high-*Q* hybrid resonator that addresses the drawbacks of traditional contour-mode mechanical resonators of both types. This dissertation work attempts in combining both piezoelectric and capacitive into one hybrid resonator to achieve micro-mechanical resonators with low insertion loss and small motional resistance while still retains all the other aforementioned benefits. Some may argue that a TPoS (presented in Chapter 3) structure is a hybrid resonator, however, this type of device still uses piezoelectric

material itself as both the driving and sensing elements. TPoS structure sacrifices some of its high electrical mechanical coupling in order to achieve the necessary *Q* and frequency for the intended applications. In the end, what TPoS really achieved is a compromise between piezoelectric and capacitive resonators. The hybrid concept presented here truly merges both types of resonators into one, not a compromise. It actually segregates the driving and sensing electrodes into two different mechanisms. Not only will it exhibit all the benefits of a TPoS MEMS resonator, it also inherits the capacitive resonator's self-switching capability, voltage controlled configurability, better thermal stability. Moreover, the electrode configuration of such device also allowed the use of a middle ground plane to achieve true input and output isolation. With the hybrid design, a designer can produce resonators with multi-port configuration and asymmetric input-output characteristic behavior.

5.3.1 Fabrication Process

The fabrication process is almost identical to fabricating a capacitive and piezoelectric resonator back-to-back. Figure 5.7 below illustrates the fabrication process for the dual-transduced hybrid resonator. (a) Start with patterning the device layer of the SOI wafer to define the Si vibrating body, and then followed by a blanket of plating seed layer and ALD gap dielectric film. (b) Photoresist is then defined for selective area copper metal plating. (c) Afterwards, the wafer undergoes CMP planarization until the Si interface is exposed completely. (d) Bottom electrode is deposited and patterned by lift-off. (e) 500 nm of ZnO is then sputtered onto the entire wafer. After depositing and patterning the top electrode, (f) ZnO is etched by diluted HCl and DRIE to define the bottom electrode via and resonator body. (g) DRIE is used again to create isolation between ports and ground. (h) Finally, the device is released from the backside by performing through-wafer etch.

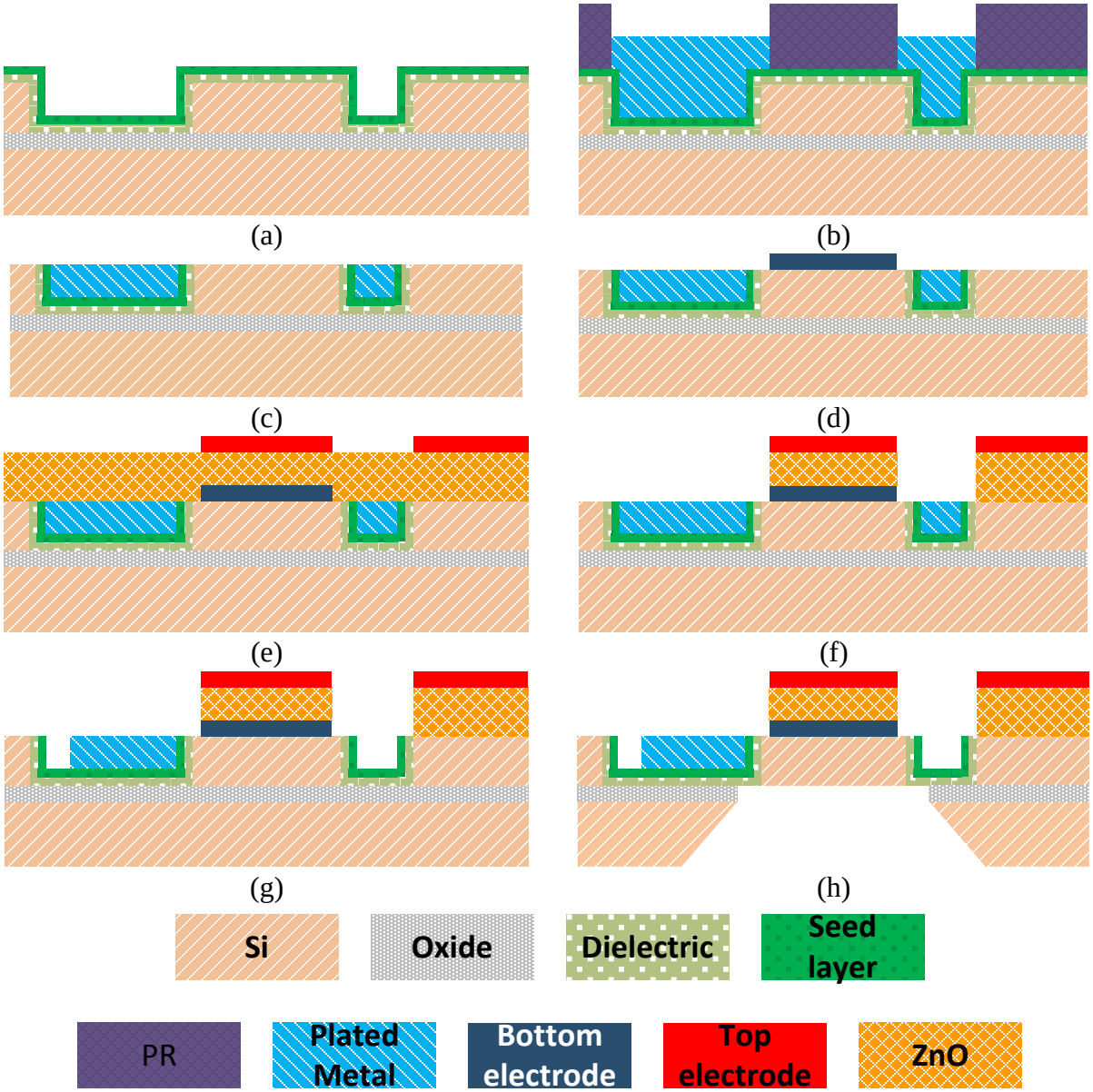

Figure 5.7 – Fabrication process of the dual-transduced resonator.

The major modification in this process is the device release method. Wet release method from previous fabrication process cannot be used because HF solution attacks the ALD dielectric film at an enormous rate. Typically it required approximately forty minutes to fully release a 40 µm rectangular plate resonator with HF, but it only takes less than five minutes to etch away the entire ALD thin film. As shown in Figure 5.7(c), the plated metal sits atop the ALD layer, and if

the dielectric layer got etched away entirely, the plated metal will be released from the substrate. Therefore, it is chosen to release the resonator device from the backside. SEM picture of the final fabricated hybrid resonator is shown in Figure 5.8 below.

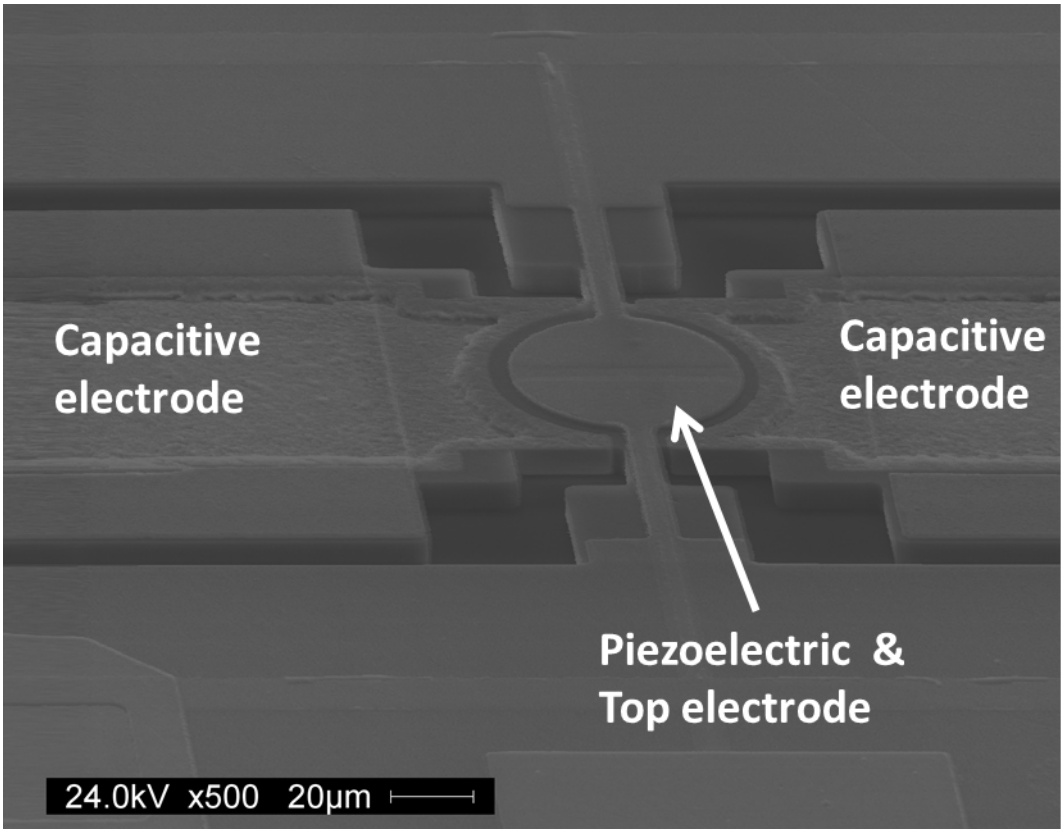

Figure 5.8 – SEM image of dual-transduced hybrid resonator.

5.3.2 Experimental Result

Regrettably, due to the extremely complicated fabrication process, (total of nine mask layers), the yield rate is almost non-existent. The frequency response could not be reported due to several factors. To start with, because of the ALD dielectric material precedes the step of device release, it creates major hurdle in releasing the mechanical structure for it to vibrate freely. If harsh chemicals such as HF are used, it will eat away the footing of the plated metal electrode and cause everything to fell off the surface of the wafer. Backside release was

performed to resolve this problem, however, after Si through-wafer etch is complete, removing of the buried oxide layer proves to be another major challenge. Using wet chemical such as buffer HF (BOE) solution didn't work as expected. The micro-meter size openings and surface tension of the chemical prohibited the solution from entering into the release hole. This phenomenon is also known as the bubble blocking. Small bubbles can be seen forming at the openings blocking the entry of chemical. Since wet etching method didn't perform properly, HF vapor etch was used in hope of gas vapor can enter deep into the high aspect ratio opening, however, even in its vapor form, HF still attacks other layers aggressively. Metal electrodes and ZnO layer were all etched away within minutes rendering the whole device inoperable. DRIE dry SiO_2 etch from the backside didn't work either. The opening's aspect ratio was too high for the ionized gas molecules to reach all the way through for any chemical reaction to occur.

This brings up the second factor. ZnO itself was the other bottleneck to this process. To etch the oxide, or to form the air gap of the capacitive resonator, using of chemicals such as BOE and HF is inevitable. ZnO just happens to be extremely vulnerable to both chemicals. Releasing the device meant destroying the ZnO layer. There was no other way around it unless other type of piezoelectric material was substituted for ZnO. Aluminum Nitride (AlN) is highly recommended for this case. It is impervious to HF, which will make the device release a much simpler experience. Moreover, if the AlN is used instead of ZnO, it is possible to eliminate two mask layers from the fabrication process simplifying the fabrication process, which hopefully will increases the yield rate.

5.4 Parasitic Feedthrough

From the experimental result in section 4.4, it is clearly shown the parasitic elements deteriorate the performance of micromechanical resonators. There is no doubt all micron-scale

resonators suffer from this parasitic effect, and it is usually believed that electrostatically-transduced resonators are less susceptible to leakage signal. However, prior research works have not done justice to this general belief. No efforts have been made for a direct-comparison between the two types of resonators. In order to conduct an un-biased comparison, both types of resonators need to be fabricated using the same equipment and materials. This section shows the result of such comparison. Not only the resonators are fabricated on the same substrate, but they are also fabricated within the same run of process subjecting the devices through identical chemicals and temperature annealing treatments.

The fabrication is done using the process described in section 5.3.1. Each type of resonators could be produced by only using certain steps from the nine layers process. The following sections will show the comparison between both types of resonators, and the effect of the substrate resistivity is also documented.

5.4.1 Comparison between Capacitive and Piezoelectric Resonators

The fabricated micromechanical resonators were tested by on-wafer RF probing, the same technique and setup used in measuring piezoelectric and capacitive resonators from the previous chapters. The measurements presented here are meant to capture the parasitic feedthrough signal's effect to resonators' wide-span frequency response. Parasitic elements become more noticeable at higher frequency. Even though the sweep frequency is much higher to the device's resonant frequency, the measured response is still a valid reference for devices designed to operate at higher frequencies. It is worth mentioning that the high Q resonance peaks aren't shown in the measurement plot due to the wide-span measurement settings and low data point resolution.

Figure 5.9 below shows the measured frequency response for a 60 µm by 150 µm plate resonator of three different kinds. Some interesting conclusions can be drawn from this plot. First, the figure clearly shown the capacitive resonator with air gap does indeed have better overall noise floor response. The capacitive type's noise floor is 20 dB lower than the piezoelectric resonator's across the whole frequency range.

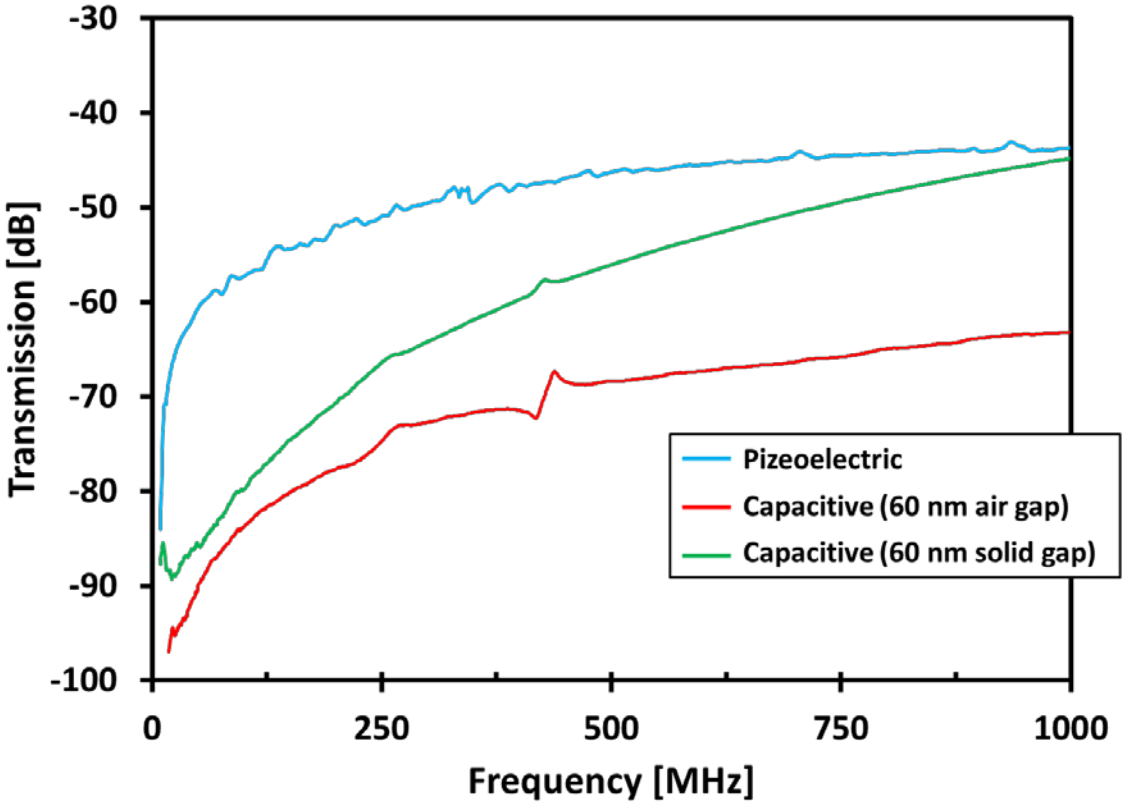

Figure 5.9 – Frequency response from three different types of resonators up to 1 GHz.

This can be explained by the two resonators' distinctive electro-mechanical transduction mechanisms. As illustrated in Figure 5.10 below, piezoelectric resonators rely on the two closely placed electrodes on top of the ZnO layer for actuating and sensing operation. Physically, the leakage signal (yellow arrow in the figure) can travel through the substrate and the piezoelectric material itself. At high frequency, the RF signal can travel through insulator without much

difficulty. On the other hand, for an air gap capacitive resonator, the feedthrough signal is limited to only the substrate traveling path, since air provides superior signal isolation than any solid dielectric. Therefore, the overall parasitic feedthrough signal is considerably less for air gap capacitive resonators. This explanation is further confirmed by replacing the air gap with solid dielectric material. Without the air gap isolation, the RF signal can now travel freely through the actuation and sensing parallel plate electrodes. Because of the nano-meter gap size, the solid gap's feedthrough signal escalated quickly as frequency goes higher, and caught up with piezoelectric resonator's noise eventually.

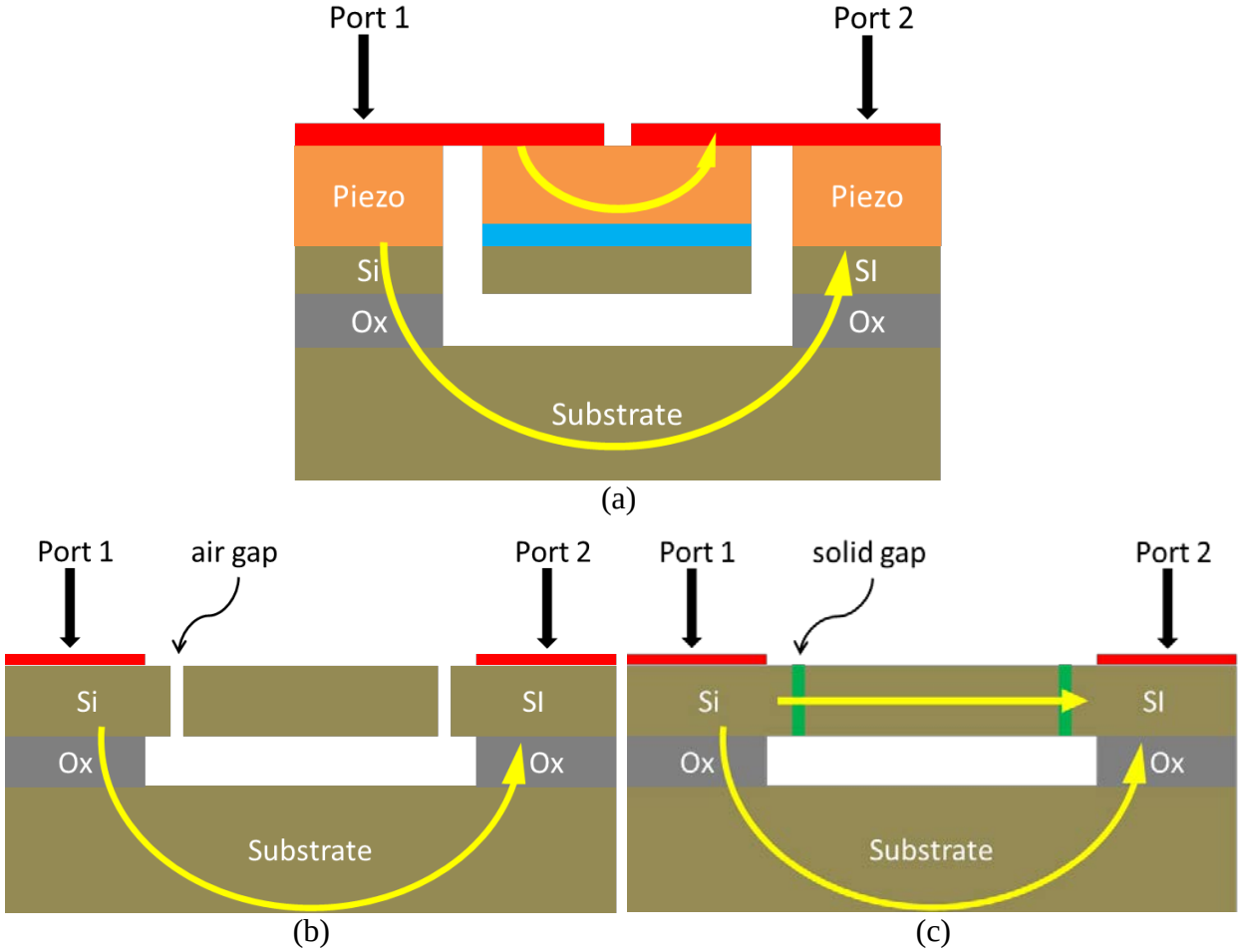

Figure 5.10 – Illustration of leakage feedthrough signal travel paths for different resonators. The yellow arrow represents the leakage signals.

5.4.2 Comparison between High and Low Resistivity Substrates

A number of approaches (triple well, guarding ring, through wafer connect, etc) [71, 72] have been carried out on minimizing the crosstalk performance within the MEMS device. Wu *et al*. [73] were able to engineer a faraday cage structure into the substrate by combining the use of plating and DRIE techniques.

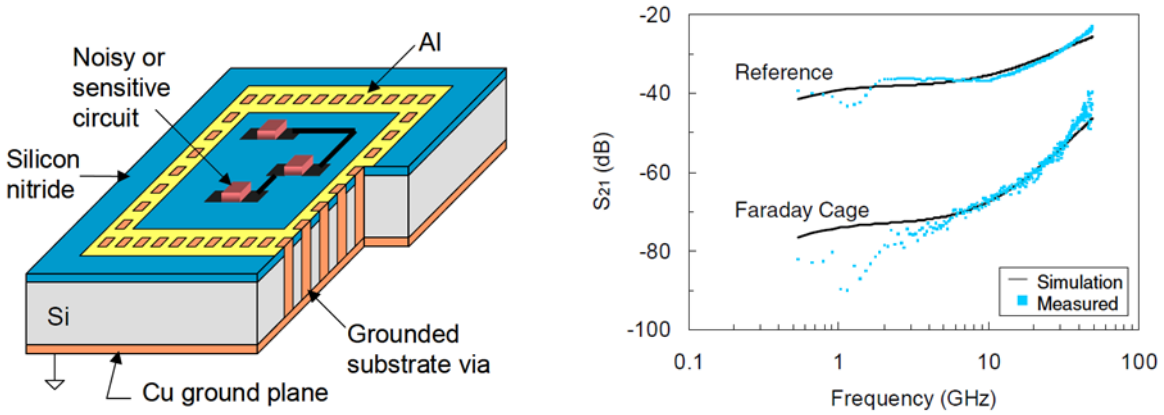

(a) (b)

Figure 5.11 – (a) A faraday cage structure engineered into the substrate. (b) Minimum 20dB improvement in transmission across the whole frequency range [73].

With the input and output electrodes completely isolated, more than 20 dB of improvement in cross talking can be obtained even at frequency up to 10s of GHz. However, it is extremely challenging to engineer such feature into an already complicated resonator structure. A more suitable solution that can be implemented with MEMS devices is the high resistive isolation technique. These studies demonstrated potential of minimizing the cross talk between input and output by increasing the resistance in the path of the signal feedthrough.

To demonstrate, piezoelectric MEMS resonators are fabricated on SOI wafers with high (> 1500 Ω•cm) and low (10-20 Ω•cm) handle layer resistivity, and the frequency wide-span response is measured. Figure 5.12 below clearly shows the resonator sitting on high resistive substrate has lower noise floor in overall frequency response. To further clarify the effect of the

substrate's impact on parasitic feedthrough, measurements were taken from special designed test structure. The test structure is designed to have all the necessary device layers (Si, metal electrodes, piezoelectric, etc) except for the resonating body structure. By taking out the resonator, feedthrough capacitiance, C_f (Figure 4.7), can be eliminated entirely, revealing the purest response from the substrate alone.

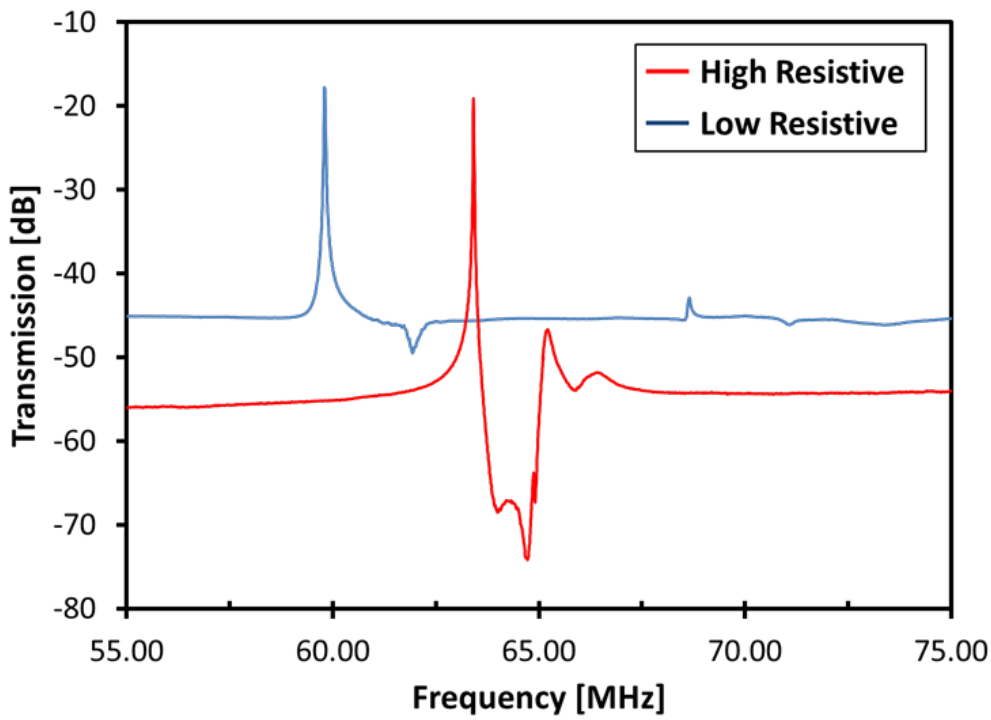

Figure 5.12 – Frequency response from 60 µm × 150 µm resonators residing on SOI substrates with different resistivity.

Figure 5.13 below is a schematic representation of the substrate's parasitic elements [74, 75]. Lateral elements, R_{lat} and C_{lat}, are mainly contributed by the cross talking between input and output ports through the layers of piezoelectric ZnO and SOI wafer's device and handle layers. Elements such as R_{sub} and C_{sub} represent the signal traveling path to the grounded bottom side of the wafer. Electrode pad capacitance, C_{pad}, is the capacitors formed between the pad, piezoelectric layer, buried oxide, and Si layers.

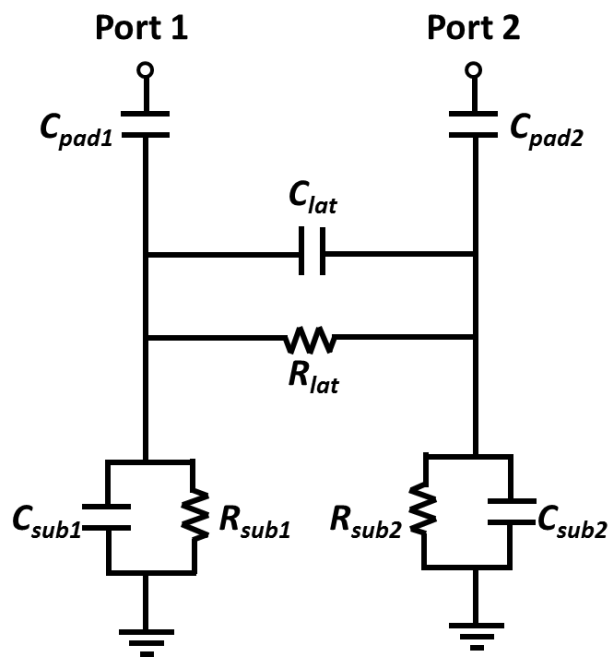

Figure 5.13 – Equivalent circuit model representation of SOI wafer.

The measurement results are shown in Figure 5.14 below. Unsurprisingly, frequency response from high resistive wafer exhibits nearly 20 dB lower noise floor which corresponds to the results shown in Figure 5.12 very well. The ADS simulated results using the equivalent circuit model are shown here as well, and Table 5.3 below summarizes the values of the substrate's parasitic elements.

Table 5.3 – SOI wafer's electrical equivalent parasitic elements

	High Resistive Wafer	**Low Resistive Wafer**
C_{pad} **[fF]**	264.8	641
C_{lat} **[fF]**	227	262
R_{lat} **[kΩ]**	8.4	5.1
C_{sub} **[pF]**	16.8	0.8
R_{sub} **[Ω]**	3110	118

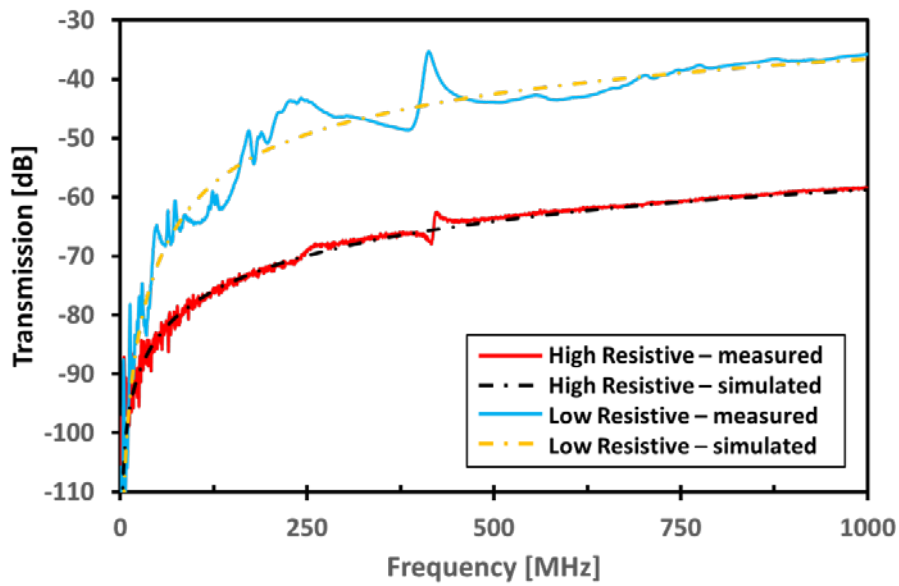

Figure 5.14 – Frequency response from test pad structures residing on SOI substrates with different resistivity.

One thing worth mentioning here is that the device layer thickness is not the same for both high and low resistivity wafers. It is rather challenging to obtain SOI wafers with identical parameters. Therefore, the device layer thickness is 6 and 15 µm for low and high resistivity wafer, respectively. The difference in device layer thickness is reflected in the value of C_{pad}, which by definition should be the identical if not roughly the same value. The difference in C_{pad} value reflects the change in thickness rather accurately. R_{lat} and C_{lat} are mainly defined by the test structure's probe pad distance and device layer's conductivity. Though the device layer resistivity is rather low for both wafers (1-5 Ω•cm), the difference in layer thickness yields minor shifts in element values. The major difference between the two wafers resistivity is better presented by the value of R_{sub} and C_{sub}. Clearly, there is an order of magnitude difference between R_{sub} due to the difference in substrate resistivity. These reference parameters are useful and will help in determining the most appropriate type of wafer to use for the development and design of future MEMS resonating devices.

Chapter 6

Conclusion and Future Work

6.1 Summary and Contributions to the RF-MEMS Field

This dissertation research has investigated the design and fabrication of both piezoelectrically- and electrostatically- transduced MEMS resonators. High yield CMOS compatible process have been successfully developed for both types of resonators, which will facilitate future monolithic integration between MEMS and CMOS circuitry on the same chip in order to fulfill single chip transceiver integration. The contour-mode devices' resonance frequencies are determined by its in-plane dimensions of the micromechanical structures, which allow multiple resonators to operate at different frequencies on the same substrate from a single fabrication run. The incorporation of low acoustic loss single crystalline silicon as the structural material, improves both the linearity and the quality factor of the resonators. Piezoelectric and capacitive resonator with Q higher than 3,000 and 10,000, respectively, are presented in this dissertation.

Filter implementation of piezoelectric MEMS filter has been attempted. Filters operating at above 100 MHz with 1.26% bandwidth and 6 dB insertion loss have been demonstrated. It is proven that MEMS filters can perform just as well as their purely electrical counterparts while also being IC compatible which is suitable for single-chip multi-frequency applications In addition, two different greatly simplified fabrication process have been developed for capacitive resonators. A two-steps fabrication process for producing capacitive resonator with sub 100 nm

actuation gap have been demonstrated. This process has greatly reduced the complexity of capacitive resonator which usually requires processing steps of five or six. In addition, some preliminary result for a brand new concept of single-mask capacitive resonator fabrication has been documented. With this technique, a silicon capacitive resonator with 100 nm transduction gap can be produced within a single photolithography step. This technique does not rely on using exotic materials or direct-write method, therefore, it is applicable in mass production environment. Since the said resonator only consists of Si, the prospect of the single-step capacitive resonator integrating with CMOS foundry process is without a doubt.

Other experimental applications have also been pursued. For a long time, no matter in MEMS or in electrical domain, reversible-frequency tuning has always been much desired. With the use SOI wafer, such tuning configuration is achievable within the mechanical domain. By supplying an electrostatic force to the micromechanical structure, stress is induced onto the body which alters the mechanical properties of the structure. Due to uncontrollable factors, alternative electrothermal frequency tuning method is presented in this dissertation. By intentionally shorting the device and handle layers, a current is drawn when voltage is applied, which in turns heat up the micromechanical structure. Using the current heating mechanism, up to 4000 ppm frequency shift has been made possible. Furthermore, such tuning mechanism does not introduce more complication to the fabrication process.

A brand new concept of mechanical resonator is introduced in this dissertation. A hybrid combination of piezoelectric and electrostatic has been attempted and fabricated. The idea of such structure is expected to provide excellent signal to noise ratio while improving the electrical mechanical coupling coefficient.

6.2 Future Work

High yield, CMOS compatible MEMS resonator production methods have been presented in this work. MEMS resonators have proven to be a worthy candidate for implementation of single-chip multi-frequency applications, however, there are still much left to be desired.

Section 3.5 has shown the possibility of MEMS filter performance based on the developed resonators. However, there is still room for improvements. Many other aspects such as giga-hertz operation frequency, wider bandwidth (> 5%), and lower insertion loss all required further research and refinement. A detailed study of different resonator coupling techniques is needed for implementing RF MEMS filter within real world wireless communication applications.

Many new concepts have been introduced in this dissertation work. The idea of single-mask capacitive resonator with 100 nm gap has huge potential to be readily deployed within current CMOS compatible foundry. Unlike, piezoelectric or conventional capacitive resonators, it can be made within one single-step and out of silicon only. The fabrication process has been proven to work, one simply needs to follow up with the idea and continue the work. Further gap reduction (< 100 nm) is entirely possible provided the DRIE Si etching recipe is further fine-tuned and thinner ALD gap spacer is used.

Frequency tuning of MEMS resonator has been demonstrated. However, the preliminary result is achieved through electrothermal current heating and not the proposed electrostatic force induced electrical stiffness. It is suspected that the unexpected outcome was due to the actuation gap (buried oxide layer) being too wide. Due to the fact that USF does not have a properly functioned critical CO_2 dry release equipment, it is challenging to release devices with actuation

gap less than 1 μm without the device being damaged by stiction [76, 77]. It is recommended that future fabrication of such devices on SOI wafer with less than 1 μm buried oxide layer, or preferably 0.5 μm thick. Smaller actuation gap will induce more stiffness onto the structure, hence, alters the frequency response more significantly.

This work also introduced the idea of a dual-actuated MEMS resonator by combining piezoelectric and electrostatic actuation mechanisms together. The attempted prototype concept involves nine layers of photolithography processing steps, which is a truly insufferable fabrication process at the academia research level. Due to the amount and complexity of the fabrication, the yield rate is almost non-existence. After several prototype tests, it comes to the conclusion that the formation of the sub 100 nm gap is critical to the success of the device. If solid gap is chosen for the capacitive actuation, the gap material needs to be able to survive the rigorous follow-up processing steps without being etched away. Especially during the device releasing step, which often involves the use of hydro fluoric (HF) acid. On the other hand, if air gap is to be desired, the gap sacrificial material needs to be able to be etched away without attacking other pre-existed layers. From the experience of this work, it is highly recommended to use Aluminum Nitride (AlN) as the piezoelectric actuation layer. AlN has the advantage of being impervious to high concentration HF, which makes it ideal for device releasing and air gap formation. Moreover, AlN would introduce loading effect to the silicon resonator body due to their comparable acoustic velocity. The added benefit of AlN is the reduction of parasitic feedthrough between the input and output ports since AlN has higher electrical resistivity than ZnO.

Instead of the nine steps process presented in previous section, the original proposed hybrid resonator fabrication was merely four photolithography steps.

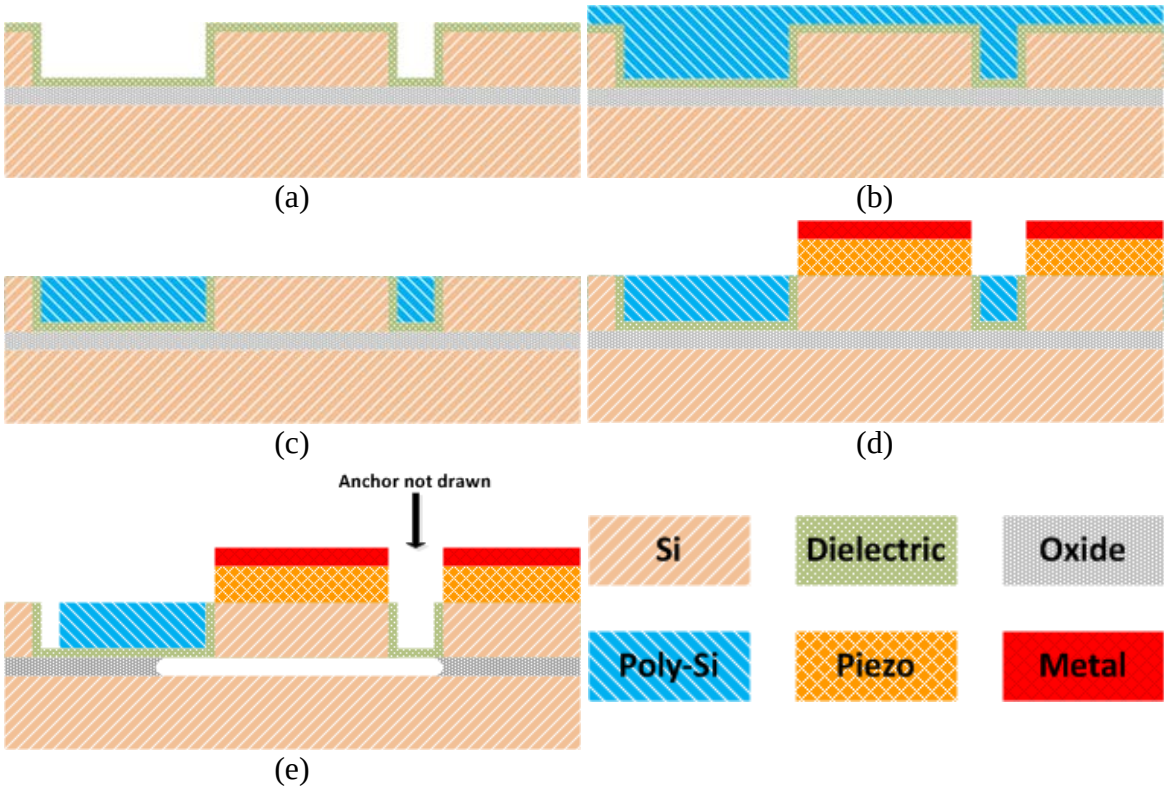

Figure 6.1 – Original proposed fabrication process for the hybrid resonator.

Figure 6.1 above depicts the original proposed process. The SOI wafer's Si layer is first patterned by DRIE to form the resonator structure, and then followed by a thin layer of ALD dielectric film as the gap spacer. PECVD poly-Si is then deposited as the capacitive electrode. CMP Planarization is applied to the top of the wafer down to the Si interface, and then followed by deposition and patterning of the piezoelectric and top electrode layers. Finally, the release hole and poly-Si electrode are etched and defined, and the structure is released by etching away the buried oxide layer underneath. PECVD poly-Si can be substituted by plated metal provided the metal can survive long duration in HF (*e.g.* nickel or gold).

This process can cut the hybrid resonator fabrication process in half, however, due to the lack of some critical elements here at USF, this process is put aside for the time being. For example, to pattern the top metal electrode and AlN piezoelectric layer, chlorine based dry

etching system is essential. In addition, identifying the correct gap spacer material is critical for the release of the device. Some other research works have shown by annealing ALD HfO_2, the dielectric material becomes resistant to HF solution [78], which, in this case, is just what the fabrication process needed.

References

[1] W. Hayward and D. Bingham, "Direct Conversion-A Neglected Technique," *ARRL, QST, Nov,* 1968.

[2] M. Brandolini, P. Rossi, D. Manstretta, and F. Svelto, "Toward multistandard mobile terminals-fully integrated receivers requirements and architectures," *Microwave Theory and Techniques, IEEE Transactions on,* vol. 53, pp. 1026-1038, 2005.

[3] D. Jakonis, K. Folkesson, J. Dbrowski, P. Eriksson, and C. Svensson, "A 2.4-GHz RF sampling receiver front-end in 0.18-µm CMOS," *Solid-State Circuits, IEEE Journal of,* vol. 40, pp. 1265-1277, 2005.

[4] R. Magoon, A. Molnar, J. Zachan, G. Hatcher, and W. Rhee, "A single-chip quad-band (850/900/1800/1900 MHz) direct conversion GSM/GPRS RF transceiver with integrated VCOs and fractional-N synthesizer," *Solid-State Circuits, IEEE Journal of,* vol. 37, pp. 1710-1720, 2002.

[5] M. A. Abdelmoneum, M. U. Demirci, and C.-C. Nguyen, "Stemless wine-glass-mode disk micromechanical resonators," in *Micro Electro Mechanical Systems, 2003. MEMS-03 Kyoto. IEEE The Sixteenth Annual International Conference on,* 2003, pp. 698-701.

[6] J. Maciel, "RF MEMS switches are reliable: a comprehensive technology overview," *MEMS Investor Journal,* Jul 8 2010.

[7] "Discera Releases World's Highest Performance Multiple Output MEMS Oscillators," Feb 22 2011.

[8] "SiTime Ships 20 Million Units of MEMS First™ CMOS Oscillators and Clock Generators " May 3 2010.

[9] H. C. Nathanson, W. E. Newell, R. A. Wickstrom, and J. R. Davis, Jr., "The resonant gate transistor," *Electron Devices, IEEE Transactions on,* vol. 14, pp. 117-133, 1967.

[10] T.-C. N. Clark and R. T. Howe, "POLYSILICON MICRORESONATORS FOR SIGNAL PROCESSING."

[11] W. C. Tang, T.-C. H. Nguyen, and R. T. Howe, "Laterally driven polysilicon resonant microstructures," *Sensors and actuators,* vol. 20, pp. 25-32, 1989.

[12] K. Wang and C.-C. Nguyen, "High-order medium frequency micromechanical electronic filters," *Microelectromechanical Systems, Journal of,* vol. 8, pp. 534-556, 1999.

[13] K. Wang, A.-C. Wong, and C.-C. Nguyen, "VHF free-free beam high-Q micromechanical resonators," *Microelectromechanical Systems, Journal of,* vol. 9, pp. 347-360, 2000.

[14] A.-C. Wong and C.-C. Nguyen, "Micromechanical mixer-filters (" mixlers")," *Microelectromechanical Systems, Journal of,* vol. 13, pp. 100-112, 2004.

[15] J. R. Clark, W.-T. Hsu, and C.-C. Nguyen, "High-Q VHF micromechanical contour-mode disk resonators," in *Electron Devices Meeting, 2000. IEDM'00. Technical Digest. International,* 2000, pp. 493-496.

[16] J. Wang, Z. Ren, and C.-C. Nguyen, "1.156-GHz self-aligned vibrating micromechanical disk resonator," *Ultrasonics, Ferroelectrics and Frequency Control, IEEE Transactions on,* vol. 51, pp. 1607-1628, 2004.

[17] S.-S. Li, Y.-W. Lin, Y. Xie, Z. Ren, and C.-C. Nguyen, "Micromechanical" hollow-disk" ring resonators," in *Micro Electro Mechanical Systems, 2004. 17th IEEE International Conference on.(MEMS),* 2004, pp. 821-824.

[18] Z. Hao, S. Pourkamali, and F. Ayazi, "VHF single-crystal silicon elliptic bulk-mode capacitive disk resonators-part I: design and modeling," *Microelectromechanical Systems, Journal of,* vol. 13, pp. 1043-1053, 2004.

[19] S. Pourkamali, Z. Hao, and F. Ayazi, "VHF single crystal silicon capacitive elliptic bulk-mode disk resonators-part II: implementation and characterization," *Microelectromechanical Systems, Journal of,* vol. 13, pp. 1054-1062, 2004.

[20] Y.-W. Lin, S.-S. Li, Y. Xie, Z. Ren, and C.-C. Nguyen, "Vibrating micromechanical resonators with solid dielectric capacitive transducer gaps," in *Frequency Control Symposium and Exposition, 2005. Proceedings of the 2005 IEEE International,* 2005, pp. 128-134.

[21] D. Weinstein and S. A. Bhave, "Internal dielectric transduction in bulk-mode resonators," *Microelectromechanical Systems, Journal of,* vol. 18, pp. 1401-1408, 2009.

[22] S. Pourkamali, A. Hashimura, R. Abdolvand, G. K. Ho, A. Erbil, and F. Ayazi, "High-Q single crystal silicon HARPSS capacitive beam resonators with self-aligned sub-100-nm transduction gaps," *Microelectromechanical Systems, Journal of,* vol. 12, pp. 487-496, 2003.

[23] R. Abdolvand and F. Ayazi, "A Gap Reduction and Manufacturing Technique for Thick Oxide Mask Layers With Multiple-Size Sub- <img src="/images/tex/241.gif" alt="\mu"> m Openings," *Microelectromechanical Systems, Journal of,* vol. 15, pp. 1139-1144, 2006.

[24] Y. Satoh, T. Nishihara, T. Yokoyama, M. Ueda, and T. Miyashita, "Development of piezoelectric thin film resonator and its impact on future wireless communication systems," *Japanese journal of applied physics,* vol. 44, p. 2883, 2005.

[25] K. Lakin and J. Wang, "UHF composite bulk wave resonators," in *1980 Ultrasonics Symposium,* 1980, pp. 834-837.

[26] R. Ruby, P. Bradley, J. Larson, and Y. Oshmyansky, "PCS 1900 MHz duplexer using thin film bulk acoustic resonators (FBARs)," *Electronics Letters,* vol. 35, pp. 794-795, 1999.

[27] K. Lakin, G. Kline, R. Ketcham, J. Martin, and K. McCarron, "Stacked crystal filters implemented with thin films," in *Frequency Control, 1989., Proceedings of the 43rd Annual Symposium on,* 1989, pp. 536-543.

[28] G. Piazza, P. J. Stephanou, and A. P. Pisano, "One and two port piezoelectric higher order contour-mode MEMS resonators for mechanical signal processing," *Solid-State Electronics,* vol. 51, pp. 1596-1608, 2007.

[29] P. J. Stephanou, G. Piazza, C. D. White, M. B. Wijesundara, and A. P. Pisano, "Piezoelectric aluminum nitride MEMS annular dual contour mode filter," *Sensors and Actuators A: Physical,* vol. 134, pp. 152-160, 2007.

[30] G. Piazza, P. J. Stephanou, and A. P. Pisano, "Single-chip multiple-frequency ALN MEMS filters based on contour-mode piezoelectric resonators," *Microelectromechanical Systems, Journal of,* vol. 16, pp. 319-328, 2007.

[31] R. Abdolvand, "Thin-film piezoelectric-on-substrate resonators and narrowband filters," 3364173 Ph.D., Georgia Institute of Technology, Atlanta, 2008.

[32] R. Abdolvand and F. Ayazi, "High-frequency monolithic thin-film piezoelectric-on-substrate filters," *International Journal of Microwave and Wireless Technologies,* vol. 1, pp. 29-35, 2009.

[33] R. Abdolvand, H. M. Lavasani, G. K. Ho, and F. Ayazi, "Thin-film piezoelectric-on-silicon resonators for high-frequency reference oscillator applications," *Ultrasonics, Ferroelectrics and Frequency Control, IEEE Transactions on,* vol. 55, pp. 2596-2606, 2008.

[34] G. Gautschi, *Piezoelectric sensorics: force, strain, pressure, acceleration and acoustic emission sensors, materials and amplifiers*: Springer, 2002.

[35] V. K. Varadan, K. J. Vinoy, and K. A. Jose, *RF MEMS and their applications*: John Wiley & Sons, 2003.

[36] W. Heywang, K. Lubitz, and W. Wersing, *Piezoelectricity: evolution and future of a technology* vol. 114: Springer, 2008.

[37] H. Campanella, *Acoustic Wave and Electromechanical Resonators: Concept to Key Applications*: Artech House, 2010.

[38] R. A. Johnson, *Mechanical filters in electronics*: Wiley New York, 1983.

[39] R. Adler, "Compact electromechanical filters," *Electronics,* vol. 20, pp. 100-105, 1947.

[40] J. M. Dewdney Montero, "Low Loss VHF and UHF Filters for Wireless Communications Based on Piezoelectrically-Transduced Micromechanical Resonators," 3543993 Ph.D., University of South Florida, 2012.

[41] S.-H. Park, B.-C. Seo, G. Yoon, and H.-D. Park, "Two-step deposition process of piezoelectric ZnO film and its application for film bulk acoustic resonators," *Journal of Vacuum Science & Technology A,* vol. 18, pp. 2432-2436, 2000.

[42] J. Molarius, J. Kaitila, T. Pensala, and M. Ylilammi, "Piezoelectric ZnO films by rf sputtering," *Journal of Materials Science: Materials in Electronics,* vol. 14, pp. 431-435, 2003.

[43] A. I. Zverev, *Handbook of filter synthesis* vol. 47: Wiley New York, 1967.

[44] A. S. Sedra and P. O. Brackett, *Filter theory and design: active and passive*: Matrix publishers Portland, 1978.

[45] W. Beaver, "Analysis of elastically coupled piezoelectric resonators," *The Journal of the Acoustical Society of America,* vol. 43, pp. 972-981, 2005.

[46] M. U. Demirci and C.-C. Nguyen, "Mechanically corner-coupled square microresonator array for reduced series motional resistance," *Microelectromechanical Systems, Journal of,* vol. 15, pp. 1419-1436, 2006.

[47] A. T. Alastalo and V. Kaajakari, "Intermodulation in capacitively coupled microelectromechanical filters," *IEEE electron device letters,* vol. 26, pp. 289-291, 2005.

[48] V. Kulkarni, "Novel RF filter structures: Acoustically coupled piezoelectric thin films," 3221068 D.Eng., University of Massachusetts, Lowell, 2006.

[49] W.-L. Huang, "Fully monolithic CMOS nickel micromechanical resonator oscillator for wireless communications," 3304990 Ph.D., University of Michigan, Ann Arbor, 2008.

[50] M. Xiong, I. T. Wu, M. Wei, and J. Wang, "Science and technology of MEMS/NEMS resonators: Si versus diamond platform materials," *Proceedings of SPIE - The International Society for Optical Engineering,* vol. 7679, May 2010.

[51] N. Sepulveda-Alancastro, "Polycrystalline diamond RF MEMS resonator technology and characterization," 3204793 Ph.D., Michigan State University, 2005.

[52] S. Pourkamali, "High frequency capacitive single crystal silicon resonators and coupled resonator systems," 3346050 Ph.D., Georgia Institute of Technology, Atlanta, 2006.

[53] G. L. Doll, B. A. Mensah, H. Mohseni, and T. W. Scharf, "Chemical Vapor Deposition and Atomic Layer Deposition of Coatings for Mechanical Applications," *Journal of Thermal Spray Technology,* vol. 19, pp. 510-516, Jan 2010.

[54] H. Im, N. J. Wittenberg, N. C. Lindquist, and S.-H. Oh, "Atomic layer deposition: A versatile technique for plasmonics and nanobiotechnology," *Journal of Materials Research,* vol. 27, pp. 663-671, Feb 2012.

[55] M. Xiong, "Development of UHF micromechanical resonators and arrays based on silicon-on-insulator (SOI) technology," University of South Florida, 2010.

[56] W. Shin, S. Park, H. Kim, K. Park, S. Joo, and H. Jeong, "Reduction of Dishing in Polysilicon CMP for MEMS Application by Using protective Layer and High Selectivity," in *Planarization / CMP Technology (ICPT), 2007 International Conference on*, 2007, pp. 1-5.

[57] K. Torki and B. Courtois, "CMP: the access to advanced low cost manufacturing," in *Microelectronic Systems Education, 2001. Proceedings. 2001 International Conference on*, 2001, p. 6.

[58] K. S. Gokhale and B. M. Moudgil, "Particle technology in chemical mechanical planarization," *KONA,* vol. 25, p. 88, 2007.

[59] J. Wang, "Self-aligned radial contour mode micromechanical disk resonators for wireless communications," 3238107 Ph.D., University of Michigan, Ann Arbor, 2006.

[60] M. A. Ionescu, N.-D. Ciressan, and M. Mazza, "Nanogap MEM resonators on SOI," 2009.

[61] J. H. Han, "Nanogap device: Fabrication and applications," 3592663 Ph.D., Marquette University, Wisconson, 2014.

[62] Y. Oh, L. Byeungleul, B. Seogsoon, K. Hosuk, K. Jeonggon, K. Seokjin, *et al.*, "A surface-micromachined tunable vibratory gyroscope," in *Micro Electro Mechanical Systems, 1997. MEMS '97, Proceedings, IEEE., Tenth Annual International Workshop on*, 1997, pp. 272-277.

[63] K. B. Lee and Y.-H. Cho, "A triangular electrostatic comb array for micromechanical resonant frequency tuning," *Sensors and Actuators A: Physical,* vol. 70, pp. 112-117, 1998.

[64] Z. Guiming, Z. Libo, X. Longqi, J. Zhuangde, Z. Yulong, W. Xiaopo, *et al.*, "Active Frequency Tuning for Magnetically Actuated and Piezoresistively Sensed MEMS Resonators," *Electron Device Letters, IEEE,* vol. 34, pp. 921-923, 2013.

[65] R. R. A. Syms, "Electrothermal frequency tuning of folded and coupled vibrating micromechanical resonators," *Microelectromechanical Systems, Journal of,* vol. 7, pp. 164-171, 1998.

[66] S. Sayed and J. V. Clark, "Active control of effective mass, damping and stiffness of MEMS," in *Design, Test, Integration and Packaging of MEMS/MOEMS (DTIP), 2013 Symposium on*, 2013, pp. 1-7.

[67] S. Hosseinzadeh, A. R. Zehtabchi, and M. H. Korayem, "Determination the Effects of Structural Parameters on Pull Down Voltage of RF MEMS Switches," in *Microwave Conference, 2007. APMC 2007. Asia-Pacific*, 2007, pp. 1-4.

[68] L. L. Chu, Q. Long, and Y. B. Gianchandani, "Temperature coefficients of material properties for electrodeposited MEMS," in *Micro Electro Mechanical Systems, 2001. MEMS 2001. The 14th IEEE International Conference on*, 2001, pp. 68-71.

[69] M. Rinaldi, A. Tazzoli, J. Segovia-Fernandez, V. Felmetsger, and G. Piazza, "High power and low temperature coefficient of frequency oscillator based on a fully anchored and oxide compensated ALN contour-mode MEMS resonator," in *Micro Electro Mechanical Systems (MEMS), 2012 IEEE 25th International Conference on*, 2012, pp. 696-699.

[70] E. Quevy, D. Galayko, B. Legrand, C. Renaux, C. Combi, D. Flandre, *et al.*, "IF MEMS filters for mobile communication," in *Emerging Technologies and Factory Automation, 2001. Proceedings. 2001 8th IEEE International Conference on*, 2001, pp. 733-736 vol.2.

[71] J. H. Wu, J. Scholvin, and J. A. del Alamo, "A through-wafer interconnect in silicon for RFICs," *Electron Devices, IEEE Transactions on,* vol. 51, pp. 1765-1771, 2004.

[72] K. A. Jenkins, "Substrate coupling noise issues in silicon technology," in *Silicon Monolithic Integrated Circuits in RF Systems, 2004. Digest of Papers. 2004 Topical Meeting on*, 2004, pp. 91-94.

[73] J. H. Wu and J. A. del Alamo, "An equivalent circuit model for a Faraday cage substrate crosstalk isolation structure," in *Radio Frequency Integrated Circuits (RFIC) Symposium, 2004. Digest of Papers. 2004 IEEE*, 2004, pp. 635-638.

[74] J. Ankarcrona, L. Vestling, K. H. Eklund, and J. Olsson, "Low resistivity SOI for substrate crosstalk reduction," *Electron Devices, IEEE Transactions on,* vol. 52, pp. 1920-1922, 2005.

[75] K. Ben Ali, C. Roda Neve, A. Gharsallah, and J. P. Raskin, "Efficient polysilicon passivation layer for crosstalk reduction in high-resistivity SOI substrates," in *Silicon Monolithic Integrated Circuits in RF Systems (SiRF), 2010 Topical Meeting on*, 2010, pp. 212-215.

[76] N. M. A. Ansari, "Understanding the effect of surface topography on stiction and friction in MEMS," 3497507 Ph.D., Auburn University, Alabama, 2011.

[77] A. Hariri, "Modeling and prediction of stiction in micro electro mechanical systems (MEMS)," NR15858 Ph.D., University of Toronto (Canada), 2006.

[78] J. Chambers, A. Rotondaro, M. Bevan, M. Visokay, and L. Colombo, "Effect of composition and post-deposition annealing on the etch rate of hafnium and zirconium silicates in dilute HF," *Proceedings of the Electrochemical Society, Cleaning Technology in Semiconductor Device Technology VII,* pp. 359-363, 2002.

About the Author

I-Tsang Wu received his B.S. and M.S. degree in electrical engineering from University of South Florida, Tampa, in 2007 and 2010, respectively. He is currently a member of the RF-MEMS Transducers Group (a division of the WAMI Center) within the Electrical Engineering Department at University of South Florida and is currently working towards his Ph.D. degree. His fields of study are RF/MW measurement and MEMS device design. His current research involves the design, fabrication, and measurement of integrated piezoelectrically- and electrostatically-transduced MEMS resonators for wireless communication applications.